Mechanisms of short-term plasticity at hippocampal mossy fiber synapses using direct patch clamp and variance-mean analysis.

Doctoral Dissertation

By:

Mamoru Tanaka

Graduate School of Brain Science, Doshisha University

Supervisor:

Dr. Takeshi Sakaba

Co-Supervisor:

Dr. Takafumi Miki

A thesis submitted for the degree of

Doctor of Philosophy in Science

March 2022

Abstract

Synapses exhibit various forms of short- and long-term synaptic plasticity, contributing to the versatile network function of the brain. Various forms of synaptic plasticity at hippocampal mossy fiber (hMF) synapses may be associated with learning and memory. However, the cellular mechanisms of the hMF synaptic plasticity remain to be resolved. In the first part, I analyzed the functional role of group III metabotropic glutamate receptors (mGluRs) at the hMF boutons using the direct patch-clamp technique. Specifically, activation of group III mGluRs is known to decrease transmitter release, but the underlying mechanisms have been lacking. I found that activation of group III mGluRs suppressed synaptic vesicle release mainly by decreasing presynaptic Ca^{2+} influx. In the second part, I have applied new variance-mean analysis to the synapses of hMF-stratum lucidum inhibitory interneurons (SLIN) in order to understand the mechanism of short-term synaptic depression during repetitive activity. I evaluated all synaptic parameters including release/docking site number (N), release probability (P), quantal size (Q), the probability of vesicle occupancy at a docking site (δ) and the probability of release of a docked synaptic vesicle (p). At hMF-SLIN synapses, it was found that short-term depression is mainly controlled by the decrease in δ. Therefore, δ is thought to be an important regulator of short-term plasticity. mGluRs are relevant to presynaptic modulation in long-term plasticity not only at hMF-pyramidal cell synapses, but also at hMF-SLIN synapses. However, the precise mechanism has not been identified at hMF-SLIN synapses. The

method used here is applicable to the analysis of not only short-term plasticity studied here, but also presynaptic modulation and long-term plasticity at hMF-SLIN synapses in the future.

Acknowledgment

I would like to thank my supervisors, Dr. Takeshi Sakaba and Dr. Takafumi Miki, for their continuous guidance, scientific advice, and encouragement. I would also like to thank Dr. Shin-ya Kawaguchi, Dr. Mitsuharu Midorikawa, Dr. Yuki Hashimotodani, and Dr. Ryota Fukaya.

I also expand my gratitude to Dr. Shigeo Takamori, Dr. Hiroaki Misonou and Dr. Nobuyuki Nukina for being my thesis committee members despite of their busy schedule.

I am grateful to the Doshisha University scholarship for doctoral students for financial support.

I am also profoundly grateful to the past and the present members of the Sakaba lab, colleagues in Doshisha and my friends for all the good times. A special thanks to my family for everything.

Part of this study has been published in Tanaka *et al*. 2021, The Journal of Physiology.

Table of contents

List of figures

Abbreviations

AMPA	α-amino-3-hydroxy-5-methyl-4-isoxazolepropionic acid
AP	action potential
AZ	active zone
Ca^{2+}	calcium ion
cAMP	cyclic adenosine monophosphate
ATP	adenosine triphosphate
C_m	membrane capacitance
CTZ	cyclothiazide
CV	coefficient variation
$_D$-APV	D-2-amino-5-phosphonovalerate
DCG-IV	(2S,2'R,3'R)-2-(2',3'-Dicarboxycyclopropyl)glycine
EGTA	ethylene glycol tetraacetic acid
EPSC	excitatory postsynaptic current
GABA	γ-aminobutyric acid
GC	granule cell
GTP	guanosine 5'-triphosphate
hMF	hippocampal mossy fiber

I_{Ca}	calcium current
L-AP4	L-(+)-2-amino-4-phosphonobutyric acid
L-Mi	lacunosum-moleculare interneuron
mEPSC	miniature excitatory postsynaptic current
Mg^{2+}	magnesium ion
mGluR	metabotropic glutamate receptor
MLCK	myosin light chain kinase
MLI	molecular layer interneuron
N	the number of docking/release site
NMDA	N-methyl-D-aspartic acid
P	release probability
p	the probability of release of a docked synaptic vesicle
PF	parallel fiber
PSC	postsynaptic current
Q	quantal size
RRP	readily releasable pool
SD	standard deviation
SLIN	stratum lucidum inhibitory interneuron

SV	synaptic vesicle
TTX	Tetrodotoxin
δ	the probability of vesicle occupancy at a docking site
ΔC_m	capacitance jump
$[Ca^{2+}]$	calcium concentration
$[Ca^{2+}]_o$	external calcium concentration

Chapter 1. General Introduction

Neurons are connected via the structures called synapses. Synapses have been initially discovered anatomically using staining methods (Ramon y Cajal, 1894). Later, the function of neurotransmission between neurons has been revealed using electrophysiological techniques (Katz, 1969). These anatomical and electrophysiological studies have led to the basic understanding of functions of individual synaptic connections and small neural networks. However, it remains to be seen how synapses and neural networks are specifically involved in higher brain functions such as learning and memory.

1.1 The role of synapses in neurotransmission

Synapses are essential for transmission of nerve impulses from one neuron to another. Many of the synapses in the central nervous system are chemical synapses. Chemical synapses transmit signals from a presynaptic cell to a postsynaptic cell by releasing neurotransmitters. Synaptic vesicles (SVs) contain these neurotransmitters. Action potentials (APs) at the presynaptic terminals open voltage-gated Ca^{2+} channels (VGCCs). Ca^{2+} channels are concentrated at the active zones (AZs) together with the protein complexes involved in synaptic vesicle fusion within the presynaptic terminal. Ca^{2+} influx into the presynaptic terminal through VGCC triggers an increase in the internal Ca^{2+} concentration,

which in turn causes fusion of SVs with the presynaptic membrane and releases neurotransmitters. The released transmitters act on the postsynaptic receptors. These receptors are usually ligand-gated ion channels activated by the specific neurotransmitter. Opening of receptor channels causes postsynaptic responses by changing membrane potential (Kandel *et al.*, 2013). After exocytosis, SV membrane is retrieved via endocytosis, and SVs are filled with neurotransmitters. SVs are functionally not homogeneous in the terminals. Most SVs are remote from AZs, not used for release, and are accumulated as a reserve pool of vesicles. A group of SVs are docked at the AZ and are immediately available for exocytosis upon calcium influx, which is called a readily releasable pool (RRP) of SVs. SVs are retrieved from the cell membrane by endocytosis, and some retrieved SVs return directly to the RRP without going through some intermediate processes, and the group of these SVs is classified as the recycling pool of vesicles. The SVs in the RRP are replenished from the recycling and reserve pools (Kandel *et al.*, 2013; Zucker & Regehr, 2002; Südhof, 2004). The RRP is defined by morphologically docked vesicles, and functionally by the number of vesicles released during strong stimulation such as a high-frequency action potential train, high osmotic shock, or else long depolarizing stimulation. Recycling pool is usually defined by optical methods, whereas reserve pool is defined morphologically (Zucker & Regehr, 2002; Alabi & Tsien, 2012). Synapses are able to change the strength of neurotransmission through plasticity. Synaptic plasticity is the key to control neural function by altering the efficiency of transmission. Some synapses in the central nervous

system have large synaptic structures, such as the calyx of Held and the hippocampal mossy fiber-CA3 pyramidal cell synapse (Borst *et al.*, 1995; Geiger & Jonas, 2000). These synapses provide a good model for investigating presynaptic function because simultaneous electrical recordings can be performed at the presynaptic terminal and the postsynaptic cell. However, many synapses in the central nervous system are small synapses that are difficult to record directly from the presynaptic terminal, and knowledge on small synapses is still limited (but see Kawaguchi & Sakaba, 2017; Ritzau-Jost et al., 2021). The results obtained from large synapses may not be generally applicable to small synapses.

1.2 Synaptic plasticity

Synaptic plasticity is divided into two types based on the time courses. The first one is short-term plasticity, in which plastic changes are maintained for a few milliseconds to a few minutes (Zucker & Regehr, 2002), and the second one is long-term plasticity, in which plastic changes are maintained for several hours to a lifetime (Nicoll & Schmitz, 2005). Short-term plasticity is thought to modulate dynamics of neural information processing such as gain control, whereas long-term plasticity is thought to operate as memory trace and be involved in learning and memory (Abbott & Regehr, 2004; Citri & Malenka, 2008)). Plasticity occurs depending on the type of synapse and the protein expressed, in addition to stimulus patterns. During facilitation, the subsequent synaptic responses are

strengthened, and during depression they are weakened (Fig. 1). Short-term plastic changes may be caused by changes in the sensitivity of the postsynaptic receptors without changing the amount of transmitter released (Jones & Westbrook, 1996). They are also caused by changes in the amounts of neurotransmitter released from the presynaptic terminal (Fisher *et al.*, 1997).

Synaptic responses are determined by N (the number of docking sites), P (release probability of synaptic vesicles), and Q (quantal sizes). Short-term facilitation is thought to be caused by accumulation of residual Ca^{2+} concentration within the presynaptic terminal during repetitive stimulation, which is sufficient to potentiate release because of the 3^{rd}-4^{th} power between Ca^{2+} concentration and release or else is caused by triggering specific facilitation sensors (Charlton *et al.*, 1982). The mechanisms of short-term depression can be multiple, and are thought to be due to desensitization of postsynaptic receptors (Jones & Westbrook, 1996) and depletion of the RRP (Foster & Regehr, 2004). However, it is unclear if the RRP depletion involves a decrease in the number of docking sites (reduction of N) or a decrease in the number of docked vesicles at the docking sites (reduction of δ). Exact estimation of the latter has been difficult in particular, because P is the product of the probability of vesicle occupancy at the docking sites (δ) and the release probability of the docked vesicles (p), and the separation of δ and p has been particularly difficult.

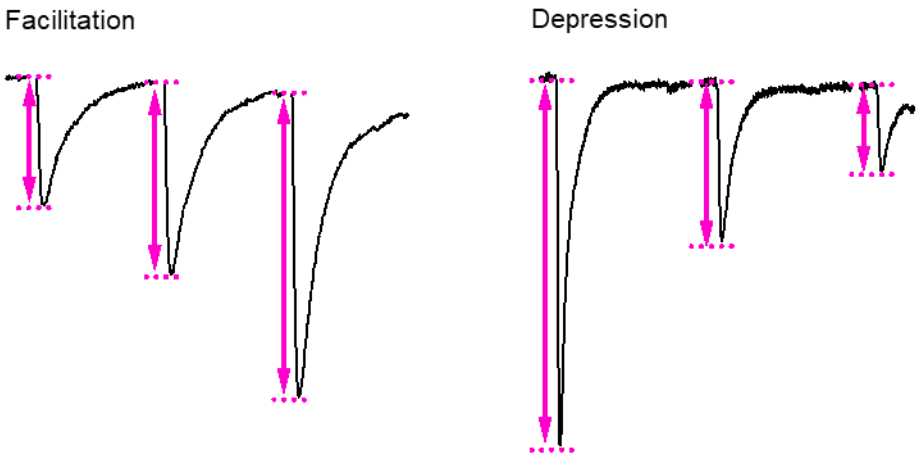

Figure 1 Synaptic facilitation and depression.

These traces are the postsynaptic currents (PSCs), which are postsynaptic responses to released neurotransmitter. Left panel shows an example of facilitation. The PSC amplitudes get larger during repetitive stimulation. Right panel shows an example of depression. The PSC amplitudes get smaller during repetitive stimulation.

1.3 Synaptic strength

The changes in synaptic strength are determined by the number of release/docking sites (N), release probability of synaptic vesicles (P), and quantal size (Q; Katz, 1969; Pan & Zucker, 2009; Fig. 2). Differences in these parameters cause functional diversity among different types of synapses and plastic changes within the same synapse. Presynaptic plasticity is mainly due to the changes in N and P, while the postsynaptic plasticity is mainly due to the changes in Q. The number of released vesicles follows binomial distribution, as synaptic vesicles at N release sites are independently released with release probability P_a (a is the number of docking sites. P_a is release probability of the a-th release site. P is average of P_1, P_2, … and P_N). It is also suggested that the parameter P can be divided into two parameters in a more detailed binomial distribution model. One of the parameters is the

probability of vesicle occupancy at the docking sites (δ), and the other is the release probability of a docked synaptic vesicle (p; Vere-Jones, 1966; Zucker, 1973; Quastel, 1997; Scheuss & Neher, 2001; Zucker & Regehr, 2002; Trigo et al., 2012; Pulido & Marty, 2017; Malagon et al., 2020; Fig. 2). The concept of docking sites has been proposed theoretically by Vere-Jones (1966) and Zucker (1973). Later, (traditional) variance-mean analysis of postsynaptic currents using parabola plots has been applied to various types of synapses. These studies have shown that synaptic depression involves reduction of P (Scheuss & Neher, 2001). Because Ca^{2+} currents are usually constant or even facilitate during repetitive stimulation, one has to propose either inhibition of transmitter release machinery (p) or else reduction of the site occupancy (δ; Neher & Sakaba, 2008). Yet, estimation of δ was not successful until recently because of lack of technique. The analysis of δ has been successfully applied to single synapses in the cerebellum by Marty's group (Malagon *et al.*, 2016) by utilizing variance of cumulative release events. Variance of the number of released vesicles should contain probability of the site occupancy (δ). However, limitation of the analysis is that one can count the number of vesicles only at single synapses, where one can ignore the fluctuation of quantal sizes within the release sites. At multiple-site synapses, the analysis is more complicated, because heterogeneity among release sites have to be considered. In-depth statistical analyses of postsynaptic currents as well as Ca^{2+}-uncaging experiments at cerebellar synapses has revealed that the docking site occupancy is incomplete at rest ($\delta < 1$), is dependent on the external calcium concentration, and that the partial site

occupancy limits the synaptic strength under high release probability (p ≒ 1) in GABAergic and glutamatergic connections (Trigo *et al.*, 2012; Malagon *et al.*, 2020). Model simulations indicate that the incomplete site occupancy has the potential of forming various types of short-term plasticity (Miki *et al.*, 2016, 2018; Pulido & Marty, 2018). Consistently, a recent study indicates that post-tetanic potentiation is associated with an increase in the docked vesicle pool at hippocampal mossy fiber (hMF) synapses (Vandael *et al.*, 2020), possibly implying that a change in the docking site occupancy may underlie post-tetanic potentiation. The correspondence between release parameters and their molecular identity needs to be addressed, in order to understand the molecular mechanism of synaptic transmission and plasticity.

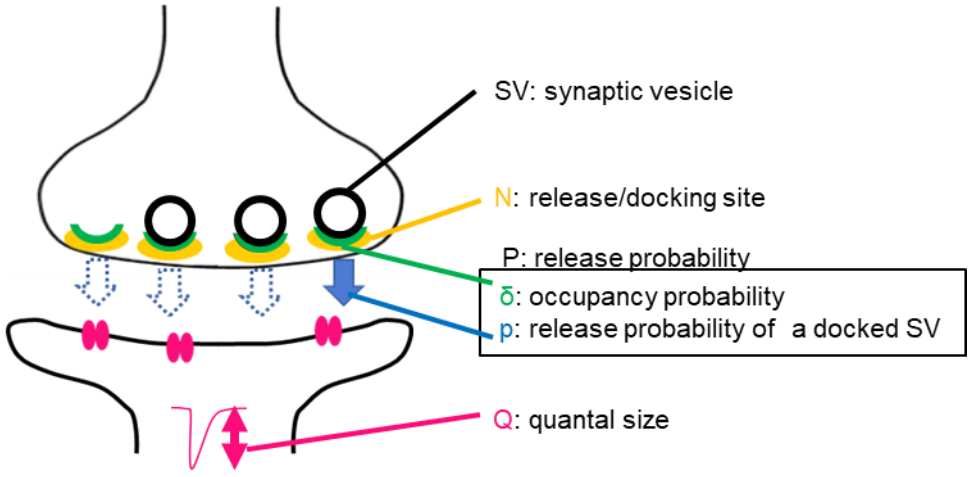

Figure 2 The parameters of synaptic strength

This figure represents the parameters of synaptic strength. Presynaptic parameters include release/docking sites (N) and release probability (P). P is can be divided into two parameters, which are probability of vesicle occupancy at the docking sites (δ) and release probability of a docked synaptic vesicle (p). The postsynaptic response per vesicle is quantal size (Q).

1.4 Hippocampal mossy fiber network

In hippocampus, hippocampal mossy fiber (hMF) axons from dentate gyrus granule cells innervate CA3 pyramidal cells and stratum lucidum inhibitory interneurons (SLINs) synapsing onto the pyramidal cells. Mossy fiber synapses are glutamatergic while interneurons form inhibitory synapses to the pyramidal cell, providing a strong feedforward inhibitory circuit in CA3 regions (Evstratova & Tóth, 2014; Mori et al., 2004; Fig. 3). Thus, hMFs constitute the network that simultaneously provides excitation via direct excitatory mossy fiber-pyramidal cell synapses outputs and inhibition with some delay via di-synaptic connection. Because excitatory synapses are facilitated and di-synaptic inhibitory pathway depressed during repetitive activity, the total output is very dynamic depending on the firing patterns of granule cells. Thus, hMFs constitute a part of so-called the tri-synaptic excitatory circuit (entorhinal cortex, dentate gyrus, CA3 and CA1), which is thought to operate as a high-pass filter and crucial for hippocampal function of learning and memory (Mori *et al.*, 2004; Bartos *et al.*, 2007; Hainmueller & Bartos, 2020). It has been observed that hMFs have different synaptic structures depending on the type of target cells (Acsády *et al.*, 1998), and each type of synapse shows different forms of plasticity. For example, hMF-pyramidal synapses have a large presynaptic terminal bouton, which contains dozens of AZs, but hMF-SLIN synapses have small boutons which include one or a few AZs. While hMF-pyramidal synapses show robust facilitation during repetitive stimulation, hMF-SLIN synapses show weak facilitation or depression (Tóth *et al.*,

2000). It has been suggested that the expression of different proteins or differential geometrical arrangement may result in such differences in plasticity.

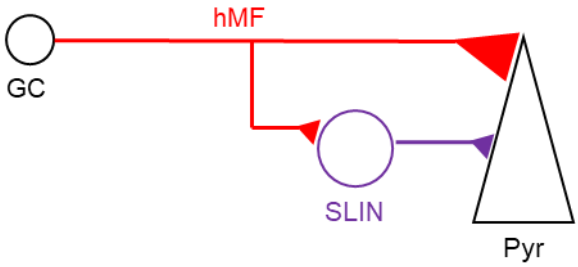

Figure 3 Model of the mossy fiber synapses innervating the cells in CA3 region

In the hippocampal CA3 region, the dentate gyrus granule cells (GC) innervate different types of target cells by hippocampal mossy fiber (hMF) axons. hMF axons innervate CA3 pyramidal cells and stratum lucidum inhibitory interneurons (SLINs). SLINs innervate pyramidal cells and form feed-forward inhibitory synapses. Pyr: Pyramidal cell.

1.5 Hippocampal mossy fiber synaptic plasticity

CA3 pyramidal cells are innervated by hMF large boutons which have complex presynaptic structures with multiple active zones (AZs) (Chicurel & Harris, 1992; Fig. 4). Interneurons of the CA3 are innervated by small *en passant* or filopodial mossy fiber synapses, which possess numerous anatomical properties distinct from the terminals on to the principal cells (Acsády *et al.*, 1998). Unlike the giant mossy fiber terminals that contain up to 35 active zones (Chicurel & Harris, 1992; Henze *et al.*, 2000), these synapses typically contain one or a few release sites on to interneurons (Acsády et al., 1998; Fig. 4). In addition to these differences in structure, there are also differences in plasticity. At hMF-pyramidal cell synapses, long-term potentiation is observed, which is stimulus-dependent and NMDA-independent, and robust short-term facilitation is observed during repetitive stimulation

even at low frequency (Harris & Cotman, 1986; Tóth *et al.*, 2000). At hMF-interneuron synapses, long-term potentiation is not usually observed and rather long-term depression is observed (Maccaferri *et al.*, 1998). In addition, robust short-term facilitation is not observed but weak short-term facilitation is observed. Either short-term facilitation or depression is observed by brief trains of high-frequency stimuli (Maccaferri *et al.*, 1998; Tóth *et al.*, 2000). When the agonists of group III metabotropic glutamate receptors (mGluRs) are administered, hMF-pyramidal cell synapses show reversible short-term depression, while hMF-interneuron synapses show long-term depression (Pelkey *et al.*, 2005). In contrast, when the agonists of group II mGluRs are administered, hMF-pyramidal cell synapses show long-term depression while hMF-interneuron synapses show reversible short-term depression (Tzounopoulos *et al.*, 1998; Pelkey *et al.*, 2005). Thus, the hippocampal network around the hMF is complex because the structure and function of the synapses are quite different even though they project from the same hMF. The mechanisms of distinct types of plasticity remain unclear. Investigating the plasticity of these synapses leads to the understanding of the function of the hippocampal network, which in turn leads to the understanding higher brain functions such as learning and memory.

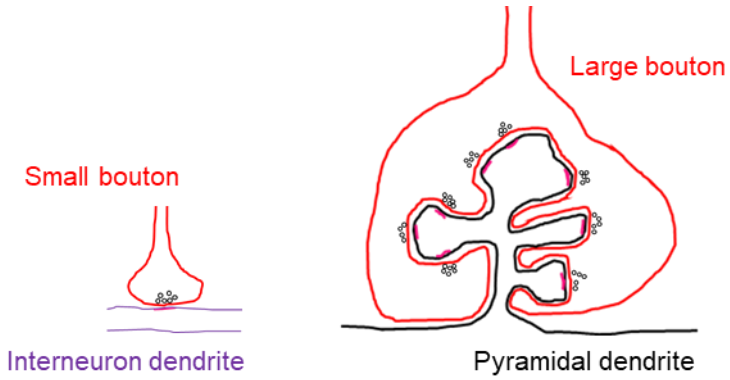

Figure 4 Model of a large bouton and a small bouton in hippocampal CA3 region.

Left panel illustrates a small bouton. It has a single active zone with a single or a few release sites. Right illustrates a large bouton. It has complex structure with multiple active zones. Red indicates mossy fibers. Purple indicates an interneuron. Black indicates pyramidal cell. Synaptic vesicles are indicated as small circles.

1.6 Role of mGluRs in synaptic plasticity at the hMF-pyramidal terminal

Presynaptic inhibition of hMFs is mediated by mGluR family (Schoepp & Conn, 1993; Nakanishi, 1994). mGluRs are divided into three groups. Group I mGluRs contain subtype mGluR1 and mGluR5. Group II mGluRs contain mGluR2 and mGluR3. Group III contain mGluR4, mGluR6, mGluR7 and mGluR8 (Conn & Pin, 1997). Group I mGluRs are mainly localized at the postsynaptic densities of asymmetrical synapses and are important for long-term synaptic depression(Ferraguti & Shigemoto, 2006). Group II and III mGluRs are localized in presynaptic region, and especially group III mGluRs are expressed in a target-specific manner(Shigemoto *et al.*, 1997; Corti *et al.*, 2002). For example, mGluR7 is located in hMF-interneuron synapse in CA3 region but not hMF-pyramidal synapse in CA3 region. Activation of group III mGluRs decreases transmitter release by several known and unknown processes, such as negative coupling to adenylyl cyclase, which decreases the production

of cyclic AMP (cAMP) (Anwyl, 1999; Cartmell & Schoepp, 2000). Analysis of the mEPSC/IPSCs has suggested direct modulation of release machinery by mGluRs (Kamiya & Ozawa, 1999). In the recording from presynaptic terminal at the calyx of Held, activation of group III mGluRs suppressed Ca^{2+} currents through G-protein-mediated modulation but did not change K^+ currents (Takahashi *et al.*, 1996). Kamiya and Ozawa (1999) have suggested that mGluRs may suppress both Ca^{2+} channels and the release machinery. However, at the hMF-pyramidal synapses, the effect of group III mGluRs has not been observed by direct presynaptic recording.

1.7 How to obtain the parameters of synaptic strength

The postsynaptic currents (PSCs), which are recorded under different release probability conditions, are used for variance-mean analysis to obtain the parameters of synaptic strength (Clements & Silver, 2000). When vesicle release follows binomial distribution, there are N vesicle sites, the average probability of vesicle release P, and the average quantal size Q. The average synaptic amplitude *m*, and variance of the synaptic amplitude *var* are

$$m = N\,P\,Q \qquad (Eq.\ 1)$$

$$var = N\,P\,(1 - P) = -(1/N)\,m^2 + Q\,m = -(1/N)\,(m - NQ)\,m \qquad (Eq.\ 2)$$

When *var* is plotted on the y-axis and *m* is plotted on the x-axis, *Eq. 2* becomes a parabolic curve. In practice, *m* and *var* are calculated from the PSCs measured under different conditions of release

probability, and the points for each release probability are plotted with the variance on the y-axis and the mean on the x-axis (Fig. 5A and B). The plots are fitted to the parabola (*Eq. 2*) to obtain the values of N, P, and Q (Fig. 5B). The parabola graph obtained by fitting to *Eq. 2* has the initial slope and intersection with x-axis. The slope, which originates from the origin and determines the initial lean of the parabola, is determined by Q. The intersections with the parabola and x-axis are origin (0) and another point. The latter point is determined by N and Q (Fig. 5B) in the simplest form. When Q is obtained from the initial slope, N is determined by the intersection. Therefore, when N and Q are obtained, P is obtained for each condition from *Eq. 1*. The obtained graph makes it easy to visually identify which parameters are changed. When Q is changed, the initial slope is changed (Fig. 5C). When P is changed, the plots of variance-mean move on the parabola curve (Fig. 5D). When N is changed, the size of parabola is changed (Fig. 5E). The combination of these changes in the parabola graph allows us to easily compare the parameter changes under different conditions. The analysis can be applied not only to evoked EPSCs in response to single stimulations. In order to obtain several data points, usually external Ca^{2+} concentrations are varied. In addition, the analysis can be applied to the EPSCs in response to repetitive stimulation, in order to estimate which parameters are changed during synaptic depression/facilitation (Scheuss & Neher, 2001). This type of non-stationary variance-mean analysis has contributed to the understanding of synaptic functions such as the mechanism of short-term plasticity. However, it is difficult to separate between docking occupancy

probability (δ) and release probability of a docked vesicle at a docking site (p) by using this analysis. Covariance can be potentially useful to separate these parameters (Scheuss & Neher, 2001), but the analysis is intrinsically noisy.

In recent years, The Marty's group extended the method of variance-mean analysis to estimate the accurate parameters and to examine the parameters in more detail, such as docking occupancy probability (δ) and release probability of a docked vesicle at a docking site (p; Malagon et al., 2016; Miki, 2019). The new method calculates the variance and mean of the cumulative number of released vesicles from the beginning to a given stimulus during a stimulus train, instead of calculating the variance and mean of release events (the PSC amplitudes) at each stimulation. Several points can be obtained in the variance-mean plot. The cumulative variance-mean plot also follows the parabola relationship. As the stimulus goes on, cumulative release increases, and variance increases until half of the sites are used. When more than half of the sites are used, variance decreases along the parabola. For example, if $\delta = 1$, cumulative release events are eventually equal to the number of release sites and variance becomes 0 when all the sites are used. If $\delta < 1$, cumulative release events are equal to $N \times \delta$ eventually, and variance due to incomplete occupancy remains at the end of stimulation. In reality, SV replenishment to the release sites has to be taken into account, which shows up as deviation from the parabola relationship. The SV replenishment can be handled by modeling (see Figure 13, for details). In summary, this method, by combining with the model of vesicle release and SV recruitment

to the docking site, allows one to estimate the values of δ and p, in addition to the three parameters obtained from the conventional analysis. At cerebellar synapses, the Marty's group has shown that increase/decrease of δ is responsible for the extent of synaptic facilitation/depression. In other words, the number of release sites is fixed and vesicles at the release sites are depleted during the train, leading to synaptic depression. During facilitation, occupancy probability of release sites with synaptic vesicles is increased. However, this new analysis method has been adequately applied to a few synapses so far because this analysis is only applicable to single connecting synapse.

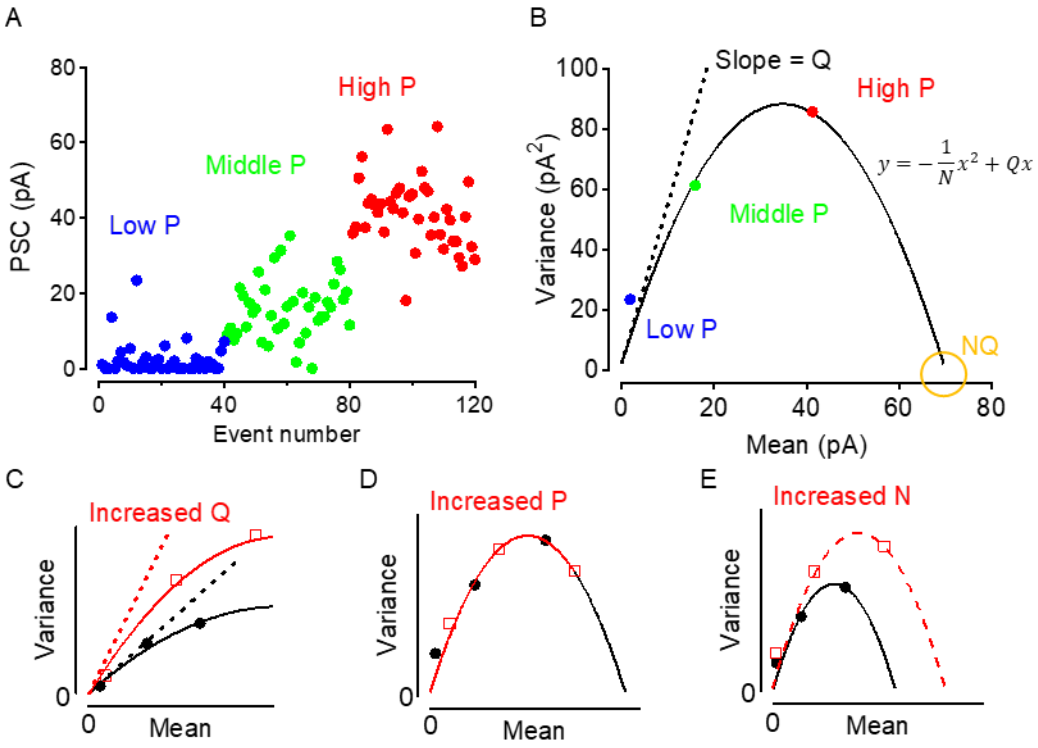

Figure 5 Description of the Variance-Mean analysis

These figures represent variance-mean analysis model. (A) This panel shows the PSC amplitudes under different conditions of release probability (P; Red is High P, green is middle P, and blue is low P). (B) Color plots are the variance- mean plots of the amplitude of each P. The parabolic curve is obtained by fitting the variance-mean plot to the equation. (C, D and E) These panels show that the changes in parabola due to changes in each parameter of synaptic strength. C indicates that the initial slope changes with Q. D indicates that the

plots move on the parabola with changing P. E indicates that the size of parabola is changed with changing N.

1.8 The aim of this study and result summary

This study has two parts, both of which are related to function of mossy fiber presynaptic terminals. In the first part (Chapter 2), I focused on hMF-pyramidal synapses and investigated the mechanisms of presynaptic inhibition by group III mGluRs. hMF-pyramidal synapse is part of the tri-synaptic circuit, an important circuit for learning and memory (Hainmueller & Bartos, 2020). Presynaptic inhibition of hMFs is mediated by mGluR family (Schoepp & Conn, 1993; Nakanishi, 1994). At hMF-pyramidal synapse, activation of group III mGluRs produces fully reversible depression (Pelkey *et al.*, 2005). However, the mechanism of presynaptic inhibition by group III mGluRs has been unclear. To investigate this, direct patch-clamp recording was performed from hMF-pyramidal presynaptic terminal with or without agonists of group III mGluRs. I revealed that activation of group III mGluRs suppressed Ca^{2+} influx but did not decrease the size of the RRP.

In the second part (Chapter 3), I attempted to clarify quantal parameters of single synapses between hMF and stratum lucidum inhibitory interneurons (SLINs). hMF axons innervate stratum lucidum inhibitory interneurons (SLINs) synapsing with the pyramidal cells, providing a strong feedforward inhibitory circuit in CA3 region (Mori *et al.*, 2004; Evstratova & Tóth, 2014). Because small en passant or filopodial extensions of the hMF boutons preferentially terminate on SLINs as a single synaptic connection (Acsády *et al.*, 1998), new quantal analysis can be applied to this synapse in

order to obtain more detailed parameters compared with traditional quantal analysis (Malagon *et al.*, 2016). One of the parameters obtained by this analysis is the probability of vesicle occupancy at a docking site (δ), which may contribute to synaptic plasticity (Pulido & Marty, 2017). However, so far this analysis method has not yet been applied to cortical synapse in the forebrain. Therefore, the effect of δ on plasticity has been unclear. To understand the relationship between synaptic plasticity and changes in the site occupancy during neuronal activity, I estimated the probability of the site occupancy (δ) separately from the release probability of a docked SV (p) based on statistical analysis of the number of vesicular events at hMF-SLIN synapses. To investigate individual vesicular events during train stimulations, I applied the recently-developed deconvolution analysis (also called matched-filtering method; Malagon et al., 2016) to single hMF-SLIN synapses. I found that the extent of synaptic depression of EPSCs (= N P Q) matched with that of the decrease in the numbers of release events (= N P) during trains under 3 mM external calcium condition. The variance-mean analysis of SV counts and model simulation indicated that the docking site number (N) was unchanged during trains. These results suggested that the release probability (P, also = δ p) exclusively determined the number of release events during a stimulus train. Using statistical analysis of the cumulative number of events, I estimated the resting occupancy probability ($\delta \approx 0.7$-0.85), and then calculated the release probability of a docked SV ($p \approx 0.6$-0.8) under 3 mM external calcium condition. Model simulations with the obtained values indicated that the reduction of the occupancy probability

(δ) accounted for the decrease in the release probability (P) during the stimulus train. External calcium concentration affected the initial occupancy probability, in turn shaping the extent of short-term synaptic plasticity. Based on these results, I suggest that the occupancy probability is a crucial determinant of short-term synaptic depression at single-AZ glutamatergic synapses in the hippocampus.

Chapter 2. Recording of Hippocampal mossy fiber terminals and the effects of group III metabotropic glutamate receptor agonist

2.1 Introduction

Hippocampal mossy fiber (hMF) synapses have different metabotropic glutamate receptors depending on the projecting target, and each synapse type has different forms of plasticity. Presynaptic inhibition of hMFs is mediated by the metabotropic glutamate receptor (mGluR) family (Schoepp & Conn, 1993; Nakanishi, 1994). Recent epilepsy research indicates that mGluRs may be a therapeutic target because they modulate both excitatory and inhibitory circuits in the hippocampus (Schoepp, 2001; Tang, 2005). The Group II mGluRs are also crucially involved in the induction of long-term depression at hMF-CA3 pyramidal cell synapses (Kobayashi *et al.*, 1996). At hMF-CA3 stratum lucidum interneuron synapses, L-AP4, the agonist of group III mGluR, causes long-term depression, but at hMF-CA3 pyramidal cell synapses, L-AP4 produces fully reversible depression instead of long-term depression (Pelkey *et al.*, 2005). In the previous study that recorded directly from the presynaptic terminal of the calyx of Held, the release probability was decreased when L-AP4 was applied, due to a decrease in Ca^{2+} influx (Takahashi *et al.*, 1996). However, at hMF-pyramidal synapses, the effect of L-AP4 has not yet been examined by direct presynaptic recording

and therefore it is unclear how L-AP4 reduces transmitter release. The reduction could be due to inhibition of Ca^{2+} currents, activation of K^{+} currents, and/or inhibition of transmitter release machinery. In order to examine if L-AP4 reduces presynaptic Ca^{2+} influx and/or the release machinery, I measured Ca^{2+} currents and capacitance jump at the hMF terminal by direct patch clamp.

2.2 Material and Methods

2.2.1 Experimental animals

Male and female Wistar rats (postnatal days 22-25) were used in accordance with the guideline of the Physiological Society of Japan. All procedures and animal cares were conducted in accordance with the guideline of the Physiological Society of Japan, and were approved by Doshisha University committee for Regulation on the Conduct of Animal Experiments and Related Activities. All efforts were taken to minimize animal numbers. Rats were given food and water freely and housed under 12:12 h light/dark cycles in temperature-controlled animal facility.

2.2.2 Experimental procedure

The rats were deeply anesthetized with evaporated isoflurane (1-3%), rapidly killed by decapitation and then their brains were removed. Transverse hippocampal slices (300 μm thick) were obtained

using a Leica VT1200S slicer (Leica Microsystems, Wetzlar, Germany) in ice-cold slice medium containing (in mM): 87 NaCl, 75 sucrose, 25 $NaHCO_3$, 1.25 NaH_2PO_4, 2.5 KCl, 10 glucose, 0.5 $CaCl_2$, and 7 $MgCl_2$. Slices were then incubated at 37°C for >1 hour in a slice medium equilibrated with 95% O_2 and 5% CO_2, and were left at room temperature (22-25°C) afterwards. For slice electrophysiological recordings, slices were visualized on an upright microscope (Axioskop, Zeiss, Oberkochen, Germany) in slice recording solution containing (in mM): 125 NaCl, 2.5 KCl, 25 glucose, 25 $NaHCO_3$, 1.25 NaH_2PO_4, 0.4 ascorbic acid, 3 myoinositol, 2 Na-pyruvate, 2 $CaCl_2$ and 1 $MgCl_2$ (pH 7.4, osmolality: 310 mosm/l). The solution was equilibrated with 95% O_2 and 5% CO_2.

2.2.3 Electrophysiological recording

For recording Ca^{2+} currents and capacitance jumps, 1 μM TTX was added to block Na^+ channels. Recordings were performed at room temperature (22-25°C) within 4 h after cutting the slices. The presynaptic terminals were whole-cell voltage clamped at -60 mV using EPC9/2 amplifier (HEKA, Bolanden, Germany), controlled by PatchMaster software (HEKA). The extracellular solution was not perfused during recording to avoid changes of the fluid level, which affects basal capacitance. The patch pipettes were filled with intracellular solution containing (in mM): 140 Cs-gluconate, 20 TEA-Cl, 10 Hepes, 5 Na_2-phosphocreatine, 4 MgATP, 0.5 NaGTP and 0.5 EGTA (pH 7.3, osmolality: 310 mosm/l). Liquid junction potential was not corrected. Membrane currents were low-pass filtered

at 2.9 kHz and sampled at 20 kHz. The data were analyzed with IgorPro software (WaveMetrics Inc., Portland, OR, USA). Patch pipettes (outer diameter: 1.5 mm, inner diameter: 0.86 mm, length: 10 cm; Harvard Apparatus, Holliston, Massachusetts) had a resistance of typically 13-20 MΩ. During recording, series resistance was maintained at 40-65 MΩ.

2.2.4 Capacitance measurements

Membrane capacitance measurements from the hMF-CA3 pyramidal presynaptic terminals were performed using an EPC9/2 amplifier in the sine+DC configuration (Lindau & Neher, 1988). A sine wave (30 mV in amplitude, 1000 Hz in frequency) was superimposed on a holding potential of -80 mV. A step depolarizing pulse (0 mV for 10, 30 and 50 ms) were used to evoke Ca^{2+} currents and exocytosis of synaptic vesicles in between sine wave.

2.2.5 Statistical analysis

Mean and standard deviations (SDs) were calculated for results of group data analysis in Igor Pro (Wavemetric, Lake Oswego, OR, USA) or Excel (Microsoft). When analyzing means, *P* values were determined with Student's *t*-test (either paired or unpaired).

2.3 Result

Comparison of Ca^{2+} current amplitudes and capacitance jumps before and after L-AP4 application

I applied whole-cell patch clamp recoding to the hippocampal mossy fiber terminal in the acute slice preparation (postnatal day 23-25) at room temperature. I measured Ca^{2+} current amplitudes and capacitance jumps with and without 100 μM L-AP4 in the external solution. L-AP4 is the group III metabotropic glutamate receptor agonist that suppress synaptic transmission between mossy fibers and CA3 pyramidal neurons of the hippocampus of guinea pig (Lanthorn *et al.*, 1984). The patch pipette contained Cs-based internal solution with 0.5 mM EGTA. External solution contained 1 μM TTX to isolate Ca^{2+} currents. The hMF-pyramidal presynaptic bouton was located in the stratum lucidum (Fig. 6A). When the terminal was depolarized from -80 mV to 0 mV, Ca^{2+} currents were activated with a time constant of 0.37 – 1.30 ms without L-AP4 (1.01 ± 0.50 ms, n = 5) and 0.96 – 10.25 ms with L-AP4 (3.31 ± 4.00 ms, n = 5; paired *t*-test, $P = 0.30$), and stayed constant afterwards (Fig. 6B and C). In 10, 30 and 50 ms depolarization, Ca^{2+} current amplitudes obtained with L-AP4 were significantly smaller than those obtained without L-AP4 (Fig. 6D; 10 ms: 110.4 ± 52.3 pA vs 64.94 ± 26.4 pA, $P = 0.030$; 30 ms: 101.2 ± 49.1 pA vs 79.2 ± 45.3 pA, $P = 0.010$; 50 ms: 91.9 ± 46.5 pA vs 78.3 ± 45.6 pA, $P = 0.001$; without L-AP4 vs with L-AP4, paired *t*- test, n = 5). Capacitance

jumps were elicited in response to presynaptic Ca^{2+} influx. The jumps obtained with L-AP4 were significantly smaller than those obtained without L-AP4 for 10 ms depolarization, but were not significantly different for 30 and 50 ms depolarization, possibly because depletion of the RRP limits the amplitude under these conditions (Fig. 6E; 10 ms: 21.2 ± 9.1 fF vs 5.2 ± 4.4 fF, $P = 0.027$; 30 ms: 27.8 ± 13.9 fF vs 31.8 ± 21.8 fF, $P = 0.555$; 50 ms : 27.6 ± 12.7 fF vs 38.7 ± 26.0 fF, $P = 0.357$; without L-AP4 vs with L-AP4, paired *t*- test, n = 5). These results indicate activating presynaptic group III metabotropic glutamate receptors suppressed Ca^{2+} influx, and decreased transmitter release in response to10 ms depolarization.

Activation of group III mGluRs suppressed Ca^{2+} influx but didn't inhibit Ca^{2+} influx completely. Therefore, vesicular release probability was lowered, and the time course of vesicle pool depletion was slowed after mGluR activation. 30 ms or 50 ms depolarization is sufficiently long to deplete the RRP under control condition (Midorikawa & Sakaba, 2017; Miyano *et al.*, 2019) and the reduced Ca^{2+} influx after mGluR activation is still sufficient to deplete the RRP. If the RRP is reduced, one would expect to see the reduced capacitance jump in response to 30 ms or 50 ms pulse. Because such a change has not been seen, it was concluded that L-AP4 did not change the RRP size.

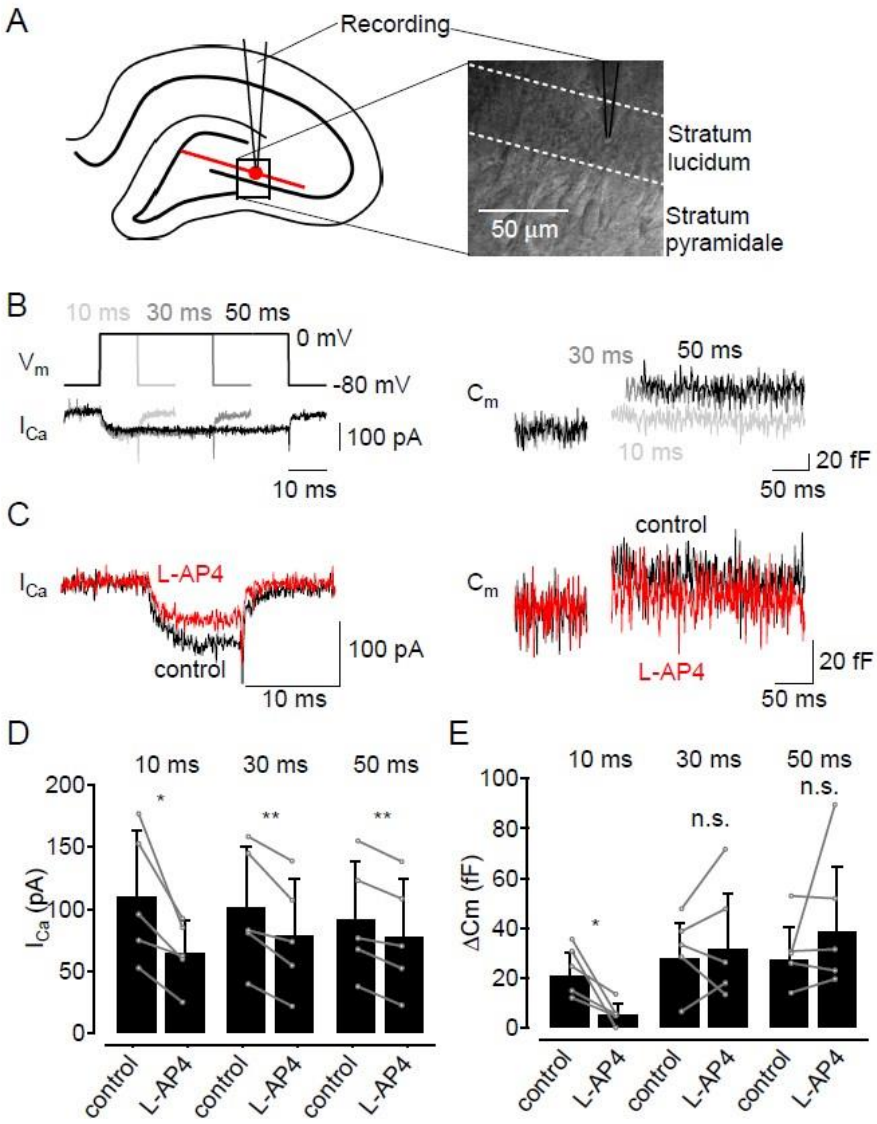

Figure 6 Comparison of Ca^{2+} current amplitudes and capacitance jumps before and after L-AP4 application

(A) The positions of the recording electrode and recorded hMF large bouton within stratum lucidum of the CA3 subfield of a hippocampal slice. Red line represents hMF and red circle represents hMF large bouton. (B) The terminal was depolarized from -80 mV to 0 mV for 10, 30 and 50 ms (V_m; light gray, dark gray and black, respectively). Ca^{2+} currents (I_{Ca}) and membrane capacitance (C_m) are shown. (C) The terminal was depolarized from -80 mV to 0 mV for 10 ms. Ca^{2+} currents (I_{Ca}) and membrane capacitance (C_m) before (black) and after L-AP4 application (red) are shown. (D) Comparison of the Ca^{2+} current amplitude (I_{Ca}) between before and after L-AP4 application. The Ca^{2+} current amplitude obtained with L-AP4 application are significantly smaller than those obtained without L-AP4 in 10, 30 and 50 ms depolarization ($P = 0.030$, $P = 0.010$ and $P = 0.001$ for control and L-AP4, respectively; paired *t*-test, n = 5) Error bars show SD. Results from the same cells are connected with lines. (E) Comparison of the capacitance jump (ΔC_m) before and after L-AP4 application. Capacitance jumps obtained with L-AP4 application were significantly smaller than those without L-AP4 for 10 ms depolarization ($P = 0.027$ for control and L-AP4; paired *t*-test, n = 5), but were not significantly different

for 30 and 50 ms depolarization ($P = 0.555$ and $P = 0.357$ for control and L-AP4, respectively; paired *t*-test, n = 5). Error bars show SD. Results from the same cells are connected with lines.

2.4 Discussion

This study showed that activation of group III metabotropic glutamate receptor suppressed Ca^{2+} influx, and decreased transmitter release for short depolarization but not for 30 and 50 ms depolarization at the mossy fiber terminal. It is likely that group III mGluRs on mossy fiber terminals primarily decreased Ca^{2+} currents, which in turn decreased the amounts of transmitter release.

2.4.1 The effect of group III mGluRs in mossy fiber-pyramidal synapses

In the present study, I recorded directly from hMF presynaptic terminals and found that activation of group III mGluRs suppressed synaptic vesicle release presumably by reducing Ca^{2+} influx and fast synaptic transmission. There has not been any report showing direct demonstration of mGluR-mediated inhibition of presynaptic Ca^{2+} currents and subsequent release process at the mossy fiber terminal. P/Q- and N-type Ca^{2+} channels are involved in fast synaptic transmission (Takahashi & Momiyama, 1993; Wheeler *et al.*, 1994; Sivaramakrishnan & Laurent, 1995). G-protein mediated inhibition of these channels have a strong effect on transmitter release at the calyx of Held synapse (Takahashi *et al.*, 1996, 1998). Group III mGluRs of hMF-pyramidal presynaptic terminal may

modulate P/Q-type Ca^{2+} channels through such a signaling pathway. mGluR family may also have a potential effect on K^+ channels, which change synaptic transmission (Cosgrove *et al.*, 2011*a*), but Takahashi et al. (1996) demonstrated that activation of group III mGluR did not suppress K^+ current at calyx of Held. Similarly, I suggest that the main action of group III mGluRs at hMF-pyramidal synapse is inhibition of Ca^{2+} currents through direct action of G-proteins, which in turn reduces transmitter release. However, because K^+ currents were inhibited by Cs-based internal solution in the present study, modulation on K^+ channels cannot be entirely excluded. Detailed signaling pathways need to be identified in the future.

2.4.2 The role of group III mGluRs in mossy fiber-pyramidal synapses

Subtype 4, 7 and 8 of Group III mGluR are expressed in hMFs, but mGluR7 is expressed only slightly in hMF-pyramidal presynaptic terminals (Shigemoto *et al.*, 1997). These indicated that reducing Ca^{2+} influx by activation of group III mGluRs was likely due to mGluR4 and 8. Activation of mGluR4/8 at the hMF boutons results in delayed action potential initiation at the postsynaptic lacunosum-moleculare interneurons (L-Mi) in hippocampal CA3 region, when the synapse was stimulated at 20 and 40 Hz (Cosgrove *et al.*, 2011*b*). If mGluRs 4/8 has the same effect on the hMF-pyramidal synapse, pyramidal cells may be regulated to avoid firing at the onset of high-frequency inputs. In contrast, at low frequencies, mGluRs4/8 are not activated and the synaptic strength is determined exclusively by

dynamics of the short-term plasticity at the hMF—L-Mi (Cosgrove *et al.*, 2011*b*). In analogy to hMF-interneuron synapses, I suggest that hMF-pyramidal synapses are regulated by the short-term plasticity dynamics at low-frequency stimulation, and activation of group III mGluRs may prevent epileptic-like firings at high-frequency stimulation.

Chapter 3. Quantal analysis estimates docking site occupancy determining short-term depression at hippocampal mossy fiber-interneuron glutamatergic synapses

3.1 Introduction

Short-term synaptic plasticity is crucial for information processing in nervous systems. The synaptic plasticity reflects rapid, bidirectional and reversible changes in synaptic strength, which is determined by the number of release/docking sites (N), release probability (P), and quantal size (Q; Katz 1969; Pan & Zucker, 2009). Recent studies using small central synapses containing a single presynaptic active zone (AZ), accumulate evidence indicating that the release probability (P) is a product of the probability of vesicle occupancy at a docking site (δ) and the probability of release of a docked synaptic vesicle (SV, p; P = δ p; Malagon et al., 2020; Pulido & Marty, 2017; Quastel, 1997; Scheuss & Neher, 2001; Trigo et al., 2012; Vere-Jones, 1966; Zucker, 1973; Zucker & Regehr, 2002). However, little has been known about the quantitative contribution of changes in the site occupancy during trains of action potentials (APs) to the extent of short-term synaptic plasticity in the forebrain.

In hippocampus, hMF axons from dentate gyrus granule cells innervate CA3 pyramidal cells and stratum lucidum inhibitory interneurons (SLINs) synapsing with the pyramidal cells, providing a strong feedforward inhibitory circuit in CA3 regions (Mori *et al.*, 2004; Evstratova & Tóth, 2014).

The tri-synaptic excitatory circuit is thought to be crucial for hippocampal function in learning and memory (Bartos *et al.*, 2007; Hainmueller & Bartos, 2020). Acsády et al. (1998) demonstrated a unique feature of the hMF: small *en passant* or filopodial extensions of the hMF boutons preferentially terminate on SLINs as a single synaptic connection. Given that single hMF axons can be stimulated reliably (Jonas *et al.*, 1993), the hMF-SLIN synapse is an ideal system to study a single synapse in the forebrain. Electrophysiological studies reveal that the majority of the small *en passant* synapses shows synaptic depression which contributes to frequency-dependent processing of information in associative hippocampal networks (Tóth *et al.*, 2000; Lawrence *et al.*, 2004; Mori *et al.*, 2004). However, the site occupancy has not been investigated at hMF-SLIN synapses because quantitative description of statistics of released vesicle numbers has been lacking. Therefore, the contribution of the site occupancy to the short-term plasticity remains unknown.

In this section, to understand the relationship between synaptic plasticity and changes in the site occupancy during neuronal activity, I established postsynaptic recording during single fiber stimulation at hMF-SLIN synapse and obtained the parameters of synaptic strength by variance-mean analysis using vesicular events.

3.2 Methods and Materials

3.2.1 Experimental animals

Male and female Wistar rats (postnatal days 16-18 and 22-30) were used in accordance with the guideline of the Physiological Society of Japan. All procedures and animal cares were conducted in accordance with the guideline of the Physiological Society of Japan, and were approved by Doshisha University committee for Regulation on the Conduct of Animal Experiments and Related Activities. All efforts were taken to minimize animal numbers. Rats were given food and water freely and housed under 12:12 h light/dark cycles in a temperature-controlled animal facility.

3.2.2 Experimental procedure

The rats were deeply anesthetized with evaporated isoflurane (1-3%), rapidly killed by decapitation and then their brains were removed. Transverse hippocampal slices (300-400 μm thick) were obtained using a Leica VT1200S slicer (Leica Microsystems, Wetzlar, Germany) in ice-cold slice medium containing (in mM): 87 NaCl, 75 sucrose, 25 $NaHCO_3$, 1.25 NaH_2PO_4, 2.5 KCl, 10 glucose, 0.5 $CaCl_2$, and 7 $MgCl_2$. Slices were then incubated at 37°C for >30 min in a slice medium equilibrated with 95% O_2 and 5% CO_2, and were left at room temperature (22-25°C) afterwards. For slice electrophysiological recordings, slices were visualized on an upright microscope (Axioskop, Zeiss,

Oberkochen, Germany) in slice recording solution containing (in mM): 110 NaCl, 2.5 KCl, 25 glucose, 25 $NaHCO_3$, 1.25 NaH_2PO_4, 0.4 ascorbic acid, 3 myoinositol, 2 Na-pyruvate, 1.2, 2 or 3 $CaCl_2$ and 3 $MgCl_2$ (pH 7.4, osmolality: 310 mosm/l). The solution was equilibrated with 95% O_2 and 5% CO_2. Three-four-week-old rats were mainly used in this study. I mentioned the age of rats in results when data was obtained from two-week-old rats.

3.2.3 Electrophysiological recording

For recording EPSCs, 50 μM $_D$-APV and 100 μM picrotoxin were added to block NMDA receptors and $GABA_A$ receptors, respectively. Recordings were performed at room temperature (22-25°C) within 4 h after cutting the slices. CA3 interneurons at striatum lucidum were whole-cell voltage clamped at -60 mV using EPC9/2 amplifier (HEKA, Bolanden, Germany), controlled by PatchMaster software (HEKA). The patch pipettes were filled with intracellular solution containing (in mM): 132.5 Cs-gluconate, 10 $CsCl_2$, 10 Hepes, 10 glucose, 8 NaCl, 2 MgATP, 0.3 NaGTP and 10 EGTA (pH 7.3, osmolality: 310 mosm/l). The stimulation pipettes for stimulation were filled with 1M NaCl. Liquid junction potential was not corrected. Membrane currents were low-pass filtered at 2.9 kHz and sampled at 20 kHz. The data were analyzed with IgorPro software (WaveMetrics Inc., Portland, OR, USA). Patch pipettes (BF-150-86-10, Sutter Instrument, Novato, CA, USA) had a resistance of typically 7-10 MΩ. During recording, series resistance was maintained at 5-28 MΩ with

compensation. For current-clamp recordings, I used the internal solution containing (in mM): 140 K-gluconate, 20 KCl, 10 Hepes, 5 Na_2-phosphocreatine, 5 MgATP, 0.5 NaGTP, and 10 EGTA (pH 7.3, osmolality: 320 mosm/l).

3.2.4 Staining

Patch pipettes were filled with the intracellular solution containing 2.5 mg/ml biocytin (Nakarai). At least 10 min after whole-cell recording, the pipettes were slowly removed. Slices were removed from recording chamber, and fixed with paraformaldehyde (4% in 0.1 PB, Wako) for 1 h at room temperature. The fixed slices were permeabilized and blocked in PBS with Triton X-100 (0.1%, Wako) and 10% FBS for 1h at room temperature, and then incubated with Alexa Fluor 568-labeled streptavidin (1:1000, Thermo Fisher Scientific) in a solution for blocking for 12-24 h at 4°C. They were washed 4 times for 10 min with PBS, and mounted with ProLong Gold (Thermo Fisher Scientific). Images were acquired using a fluorescence microscope, KEYENCE BZ-X800 (Keyence Corporation, Osaka, Japan) with a 10x dry objective lens and analyzed using ImageJ.

3.2.5 Decomposition of EPSCs

I determined occurrence times of individual EPSCs based on the deconvolution analysis to count the number of released vesicles for each stimulus, as has been described in detail (Malagon *et al.*, 2016).

I briefly describe the deconvolution analysis here. Firstly, I made an average of single EPSCs occurring later in a train to obtain a miniature EPSC (mEPSC) template in a given synapse, because at this time period multivesicular events are rare at hMF-CA3 interneuron synapses under our recording condition. Then the average mEPSC was fitted by a triple-exponential function with five free parameters including rise time, amplitude, fast decay time constant, slow decay time constant, and amplitude fraction of the slow decay. Next, I performed deconvolution using the triple exponential curve as kernel. Deconvolving the average mEPSC resulted in a narrow spike, and the deconvolved data traces resulted in sequences of spikes. Finally, I fit a given deconvolved trace by a sum of scaled narrow spikes in order to obtain the timing of each event. The amplitude parameter was free because the peak EPSC amplitudes varied during trains due to receptor saturation and desensitization. The above procedure had a detection limit that caused a failure of separation of two events occurring within 0.9 ms. To correct for missed events, I split into two or three the events having amplitudes at least 1.7 or 2.4 times larger than the average amplitude of the mEPSCs, respectively.

3.2.6 Model simulation

I implemented a stochastic synaptic model based on Monte Carlo simulation using Igor Pro (Wavemetric, Lake Oswego, OR, USA), as has been described previously (Miki *et al.*, 2016). In the two-step model, I assumed 2 independent docking and replacement sites, which were occupied by

synaptic vesicles with a probability of δ and of 1 before the first stimulus, respectively. When a vesicle is present at the docking site, release occurs with a probability of p. After releasing, replenishment of the docking site occurs stochastically with a probability of r (during one inter-AP interval) as long as the replacement site is occupied. After consumption of the vesicle in replacement sites, replenishment of the replacement site occurs stochastically with a probability of s (per one inter-AP interval). Simulations proceeded with a time increment of 0.05 ms. I repeated each simulation 5000 times to obtain values. When comparing the data and the simulation results, I normalized the data to N = 2. In the model simulation, I assumed that all vesicular events during an interspike interval (50 ms) occurred just after the stimulation.

3.2.7 Statistical analysis

Mean and standard deviations (SDs) were calculated for results of group data analysis in Igor Pro (Wavemetric, Lake Oswego, OR, USA) or Excel (Microsoft). When analyzing means, statistical *P* values were determined with Student's *t*-test (either paired or unpaired) or Wilcoxon signed rank test for paired data. All statistics were confirmed by non-parametric tests which were Wilcoxon signed rank test and Wilcoxon-Mann-Whitney two-sample rank test for paired and unpaired data, respectively. When analyzing correlations illustrated with regression lines, r represented Pearson's correlation coefficient, and *P* assessed the probability of correlation given the value of *r* and the

number of degrees of freedom of the data. Details, including sample sizes, can be found in figure legends and/or results.

3.3 Results

3.3.1 Recording of synaptic currents from mossy fiber associated CA3 interneurons

I first established recording of single hMF-evoked EPSCs onto interneurons in the CA3 stratum lucidum in hippocampal slices of rats of either sex at postnatal days 22-30 (Fig. 7; Jonas et al., 1993; Lawrence et al., 2004), because the following deconvolution analysis to detect vesicular events was only applicable to single synapse recordings (Malagon *et al.*, 2016; Pulido & Marty, 2017). Minimal stimulation method was established to record from a single synapse at this synapse.

Anatomical studies demonstrated that small *en passant* hMF synapses innervated interneurons of the CA3 stratum lucidum with a single AZ in rat hippocampus (Acsády *et al.*, 1998), indicating that the synapse was a potential single synapse containing a single AZ and a single postsynaptic density of receptors (Pulido & Marty, 2017). I used >3-week-old rats that are juvenile, because the structures of the hMF and the interneurons are matured around P20 (Amaral & Dent, 1981; Lang & Frotscher, 1990).

The interneurons in the CA3 stratum lucidum were identified based on their morphological and

electrophysiological properties. The soma of the biocytin-stained neuron was located in the stratum lucidum, while the dendrites were located mainly in the stratum lucidum and stratum radiatum (Fig. 7A; The fluorescence observed in the stratum pyramidale was thought to be the result of biocytin attaching to the outside of the pyramidal cells that could not be washed out due to insufficient perfusion). In response to depolarizing current pulses, these neurons fired at high frequency initially and showed strong firing frequency adaptation. The initial and steady-state firing frequencies were >80 Hz and around 40 Hz, respectively (Fig. 7B). These morphological and electrophysiological properties were similar to those of hMF-associated interneurons as described previously (Vida & Frotscher, 2000).

3.3.2 Identification of synapses with single hMF inputs

With the target cell identified, I next sought to identify synapse with single hMF inputs using minimal stimulation and quantal analysis. I recorded hMF-evoked EPSCs by stimulating hMFs in the granule cell layer under a high Ca^{2+} (3 mM) and high Mg^{2+} (3 mM) condition which reduced cellular excitability and allowed better isolation of the hMF-evoked EPSCs from recurrent associational/commissural EPSCs (Fig. 7C; Kwon & Castillo, 2008). Additionally, calcium was increased to achieve high release probability, which was necessary to estimate the synaptic parameter values using variance-mean analysis of the number of events in response to AP trains accurately

(Malagon *et al.*, 2016; Miki *et al.*, 2016; see below for details). The amplitudes of EPSCs were blocked by a mGluR2 agonist, DCG-IV, confirming that the recorded EPSCs were mediated by hMFs (31.8 ± 24.2 % of control, n = 7, Fig. 7D; Kamiya et al., 1996).

To stimulate a single hMF input, I finely adjusted the position of the stimulation pipette as well as the stimulation intensity so as to get a stepwise intensity-response curve (Fig.7E). Choosing a weakest stimulation intensity setting over the threshold where the success rate approached the maximum value, I collected recordings of hMF-evoked EPSCs. The mean amplitude, 20-80% rise time, decay time constant of EPSCs were 25.5 ± 8.8 pA, 0.93 ± 0.37 ms, and 4.72 ± 1.93 ms, respectively (n = 32). These EPSCs with the homogeneous amplitude indicate that they are single hMF-evoked EPSCs. Consistently, the mean amplitude was similar to the reported values of single hMF-evoked EPSCs (Lawrence *et al.*, 2004).

However, the rise and decay times of the EPSCs were slightly longer than reported values (Lawrence *et al.*, 2004). The slower time course of the recorded EPSCs at hMF-SLIN synapses was probably due to using older animals in this study (3-4 weeks vs 2 weeks in Lawrence *et al.* 2004). Because the dendrites of the interneuron were structurally matured around P20 (Lang & Frotscher, 1990), it is likely that the interneuron in 3-4-week-old animals has thinner and longer dendrites, leading to larger extent of the dendritic filtering effect. In line with the expectation, the EPSCs from 2-week-old rats showed faster kinetics that was comparable to that in Lawrence *et al.* (2004) (20-80%

rise time: 0.64 ± 0.10 ms, decay time constant: 2.89 ± 0.54 ms; n = 5). Nevertheless, the experiments where the hMF origin of recorded EPSCs was confirmed by their sensitivity to DCG-IV, also showed similar slow kinetics (20-80% rise time: 0.92 ± 0.24 ms, decay time constant: 4.69 ± 1.76 ms, n = 12), indicating that single hMF-SLIN synapses were recorded in all cases. In mature synapses (e.g., calyx of Held synapses and hair cells synapses), presynaptic AP-like Ca^{2+} current does not decrease during a train (Taschenberger *et al.*, 2002; Li *et al.*, 2014). Thus, the mature hMF-CA3 interneuron synapses probably do not exhibit presynaptic Ca^{2+} current inactivation during AP train stimulation. This could simplify analysis of mechanisms of EPSC depression (see later results and Discussion).

I further analyzed EPSCs to make sure that they were truly single hMF-evoked EPSCs. When superimposing the recorded traces at individual stimulation intensities, I found multiple amplitude levels in all cases (Fig. 7E). The amplitude histogram of all successes from the data in Figure 7E was better fitted with a double Gaussian than with a single Gaussian, suggesting the possibility that two classes of events existed (Fig. 7F; Akaike's Information Criterion value: 223.3 vs 217.3 for single vs double Gaussian fit; Spiess & Neumeyer, 2010)). If the two classes of events were derived from multiple hMF inputs rather than from a single one, one would expect that the number of events belonging to the second component may gradually increase with stimulus intensity as the success rate increased from 0 to 1. To test this, I roughly divided the events at the amplitude of 27 pA where the two Gaussian curves crossed in Figure 7F, and counted the number of events having amplitudes below

27 pA for the first component and having amplitudes above 27 pA for the second one (Fig. 7F) with varying stimulation intensities. In the stimulation range of 10-11V, where the success rate started increasing, the numbers of events which were below and above 27 pA were 24 and 13, respectively, while they were 87 and 47 when the success rate approached 1 (stimulation range: 11.6-16V). The values of the ratios of the second components to the first were 0.54 for both cases, suggesting that the ratio of event numbers between the first and second components did not vary with stimulus intensity. Thus, the simplest interpretation of the results is that the two classes of events originate from a single hMF input, and that smaller and larger amplitude events represent single vesicular and multivesicular release, respectively (Tong & Jahr, 1994).

To test the validity of this interpretation, I performed experiments for intensity-response curve under 1.2 mM external calcium concentration ($[Ca^{2+}]_o$) condition (Fig. 8A and B). If the larger events represent multivesicular release, under lower release probability condition the number of events having larger amplitude would be reduced, because multivesicular release is known to occur under high release probability condition (Silver *et al.*, 1998). As in 3 mM $[Ca^{2+}]_o$ condition, stepwise increase of average peak EPSC amplitude and gradual increase of success rate were observed. Compared with 3 mM $[Ca^{2+}]_o$ condition, the amplitude histogram for the successes in 1.2 mM $[Ca^{2+}]_o$ condition showed a reduction in the number of second class of events (Fig. 7F and Fig. 8B), suggesting the events as multivesicular release events. Therefore, these results augmented confidence

that our recordings were obtained from a single hMF-SLIN synapse.

It should be noted that there was still a possibility that I recorded from two synapses, which originated from a single hMF, had different release probabilities with similar quantal sizes, and contacted with a SLIN. However, previous morphological studies have reported that the filopodial extension from a single hMF typically innervated an interneuron with only a single contact, whereas multiple contacts were rarely observed (around 5%; Acsády et al., 1998). Therefore, such a case might be rarely included, producing at most about 5% error of group data. Also, these synapses would make the second larger component twice as large as the first component. In Figure 7F, the double Gaussian fit indicated that the small and large amplitude components were centered at 20.8 and 31.4 pA. The ratio between the values was 1.51, less than 2. Altogether, these results indicated that single synapse recordings were established at hMF-SLIN synapses.

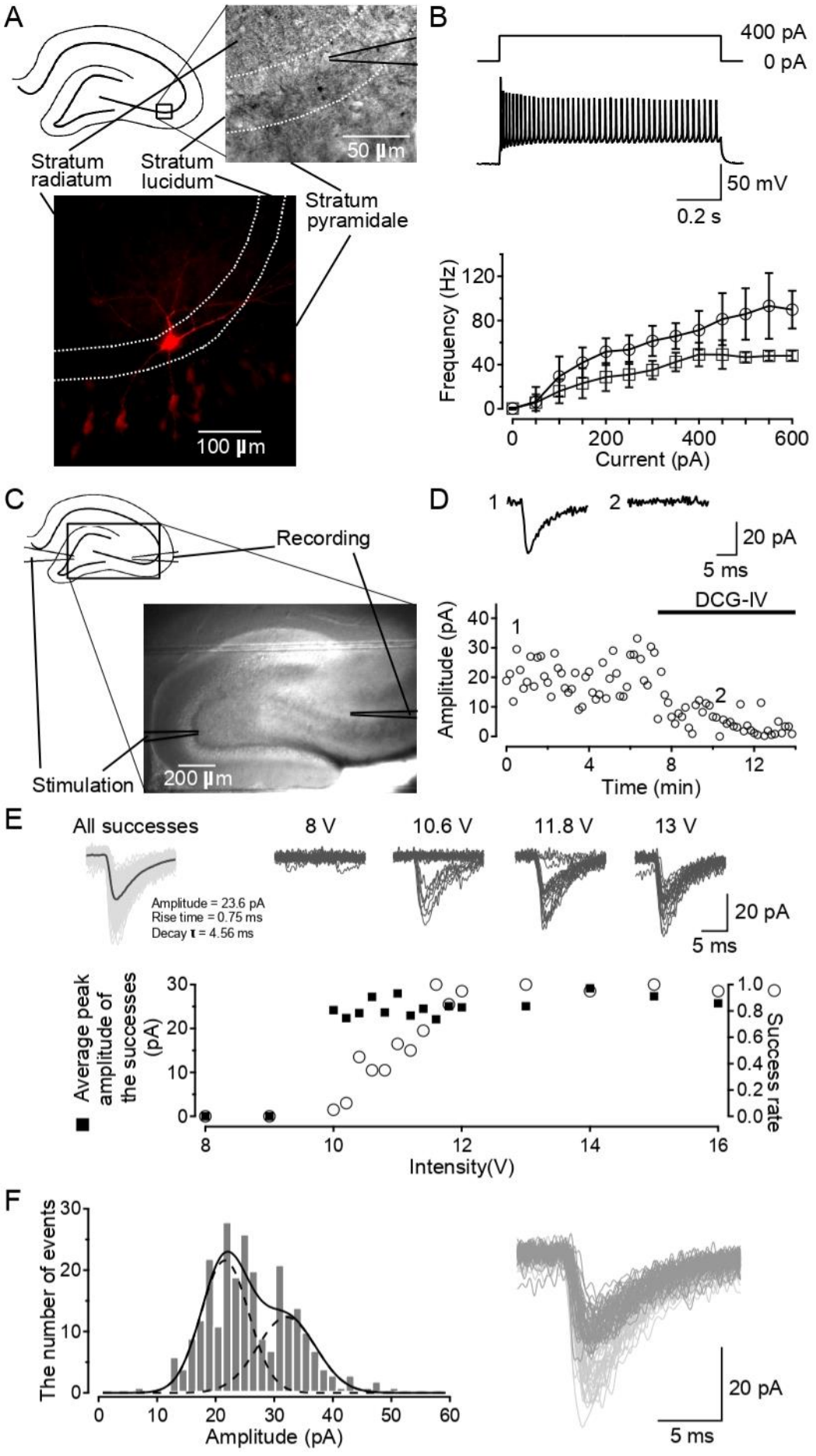
A
Stratum radiatum
Stratum lucidum
Stratum pyramidale
50 μm
100 μm
B
400 pA
0 pA
50 mV
0.2 s
Frequency (Hz)
Current (pA)
C
Recording
Stimulation
200 μm
D
1
2
20 pA
5 ms
DCG-IV
Amplitude (pA)
Time (min)
E
All successes
8 V
10.6 V
11.8 V
13 V
Amplitude = 23.6 pA
Rise time = 0.75 ms
Decay τ = 4.56 ms
20 pA
5 ms
Average peak amplitude of the successes (pA)
Success rate
Intensity(V)
F
The number of events
Amplitude (pA)
20 pA
5 ms

Figure 7 Identification of single hMF input in stratum lucidum interneurons in hippocampal CA3 region.

(A) The positions of the recording electrode and recorded neuron within stratum lucidum of the CA3 subfield of a hippocampal slice. The recorded neuron was labeled with biocytin injected through a recording patch pipette. (B) A train of action potentials elicited in the recorded neuron by a suprathreshold current pulse (400 pA). The initial (circles) and the steady-state firing frequencies (squares) are plotted against the current amplitude of the pulses (n = 9). Error bars show SD. (C) Placement of the recording and stimulating electrodes, within stratum lucidum of the CA3 subfield and dentate-gyrus subfields, respectively. (D) Evoked EPSCs were blocked by application of the mGluR2 agonist, DCG-IV (5 μM), confirming that the EPSCs were mediated by mossy fibers. The evoked EPSCs were obtained at 0.1 Hz. (E) Intensity-response curve of a potential single-fiber input. Top left, all successes (light gray) and the average trace (black) in the experiment were superimposed. Top right, 20 recorded traces for each stimulation intensity (8, 10.6, 11.8, and 13 V). Bottom, the success rate (open circles) and the average peak amplitude of the successes (filled squares) are plotted against stimulation intensities. A step-like intensity-response curve with a narrow transition region (here, at 10 – 12 V) is shown. (F) Left, an amplitude histogram of all successes in E with a double Gaussian fit (mean and variance: 20.8 pA and 16.4 pA^2 for the first Gaussian curve, and 31.4 pA and 24.7 pA^2 for the second one). The crossing point of the two Gaussian curves was 27 pA which was used to separate two groups of the successes. Right, all 75 successes for stimulus intensities ranging from 11.8 to 14V in E were superimposed. The successes having amplitudes above 27 pA and below 27 pA were shown in light gray and dark gray, respectively.

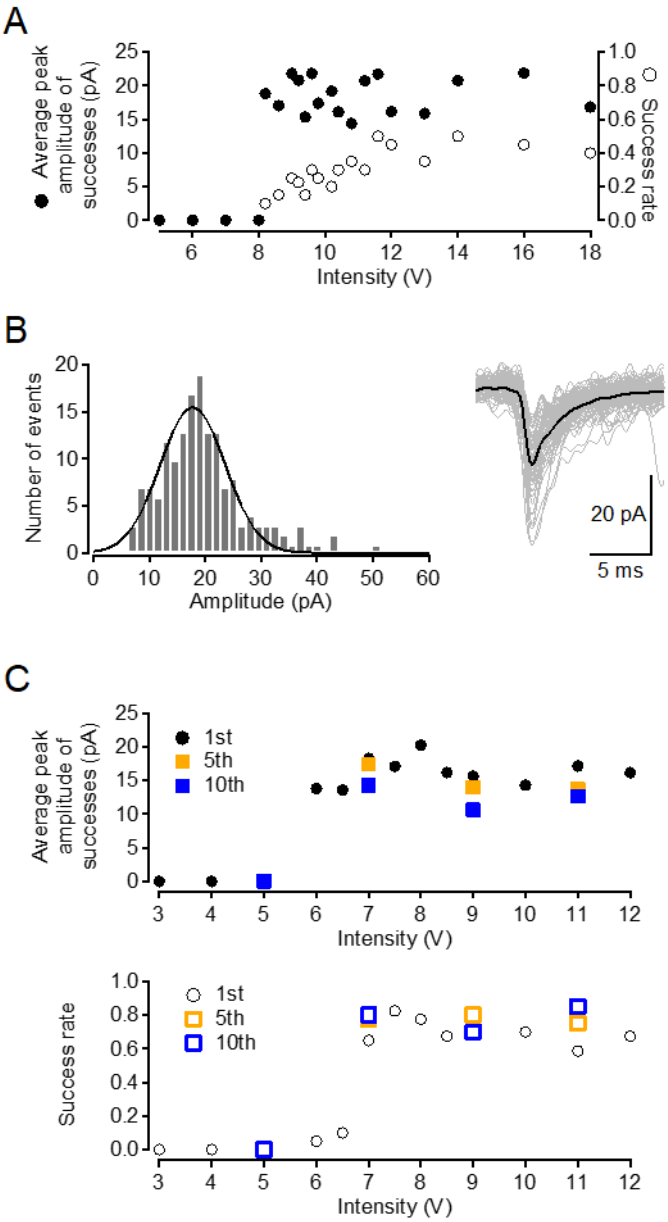

Figure 8 Isolation of single hMF input.

(A) Intensity-response curve of a potential single hMF input recorded in 1.2 mM $[Ca^{2+}]_o$ condition. The success rate (open circles) and the average peak amplitude of the successes (filled circles) are plotted against stimulation intensities. The success rate gradually increased with stimulus intensity ranging from 8 to 12 V, and then became stable after 12 V, while the average peak amplitude was stable from 8 to 18V. (B) Left, an amplitude histogram of the all successes in A with a single Gaussian fit (mean = 17.8 pA, variance = 33.9 pA^2). Right, 80 successes (light gray) and the average trace (black) in A were superimposed. (C) Intensity-response curve obtained from recordings with single and train stimulations (e.g., 10 stimuli at 20 Hz) in 1.2 mM $[Ca^{2+}]_o$ condition at a hMF-SLIN synapse. I recorded EPSC traces repeatedly 40 times for each stimulus intensity. Top, the average peak amplitudes of the successes obtained from 1^{st}, 5^{th}, and 10^{th} responses are plotted against

stimulation intensities. Bottom, the success rates obtained from 1st, 5th, and 10th responses are plotted against stimulation intensities.

3.3.3 Vesicle counting by decomposition of EPSCs

The aim of the study in this chapter is to apply the variance-mean analysis of release events, instead of EPSC amplitudes, to estimate hidden parameters of synapse transmission. In order to apply variance-mean analysis of cumulative release events, it is important to obtain vesicle number from EPSCs. In this section, I achieved this by deconvolution of EPSCs with miniature EPSCs (mEPSCs), which represent single quantal events.

The basic idea to isolate mEPSCs is to make a condition, in which EPSCs rarely occur (Malagon *et al.*, 2016). Tóth et al. (2000) demonstrated that the majority of hMF-interneuron synapses displayed depression in response to repetitive stimulation under 2.5 mM $[Ca^{2+}]_o$ condition (2.5 mM Ca^{2+}/ 1.5 mM Mg^{2+}). Therefore, by augmenting this depression in the high Ca^{2+} condition, rare and stochastic mEPSC events can be recorded. I recorded EPSCs with a train of stimulations at single hMF-SLIN synapses (e.g., 10 stimuli at 20 Hz repeated every 15 sec). The repetitive stimulations at single hMF could be reliably applied without changing stimulation threshold during trains (Fig. 8C).

At the single synapses, an EPSC with relatively large amplitude was observed in response to the first stimulus in a train, while failures were often observed in response to later stimuli (Fig. 9A, left). The data suggested that multiple vesicular events frequently occurred at the beginning of a train,

while one/zero vesicular events mainly occurred in response to later stimuli. Thus, for the decomposition of EPSCs I used the EPSCs which occurred later in a train as representative mEPSCs at a given synapse. According to Malagon *et al*. (2016), I performed the deconvolution analysis as follows. I aligned several mEPSCs from a given synapse with respect to their peaks, and calculated their average (Fig. 9B). I then deconvolved the averaged mEPSC using a model curve obtained by a fit of the averaged mEPSC with a combination of three exponentials (Fig. 9B, see Methods; Malagon *et al*. 2016). The deconvolution resulted in a narrow spike-shaped curve which was used as a template of one vesicle event for further analysis (Fig. 9B). The same deconvolution method was applied to the entire recorded traces, providing the deconvolved traces (Fig. 9A, middle). The deconvolved traces were fitted with a sum of amplitude-scaled spike templates, in order to obtain the occurrence times and the amplitudes of the quantal events (Fig. 9A, right).

Figure 9C shows examples of EPSCs analyzed by this method. A single vesicular event (left) and two successive events (middle) were detected by the fits using the templates. The third example illustrates a large spike (right) which could be fitted with a single amplitude-scaled template, but which nevertheless presumably represented multiple events. As discussed by Malagon *et al*. (2016), two successive events with a short time interval (<0.2 ms) could not be resolved by the deconvolution method. In our analysis, the time interval of the detection limit was <0.9 ms (Fig. 10). Therefore, these unresolved large events could increase the number of missed events and thus interfere the

analysis, particularly the event counts. To correct this, I determined the amplitude threshold to split large events based on the degree of amplitude occlusion. Amplitude occlusion takes place in a pair of consecutive EPSCs, when postsynaptic receptors participating in the first EPSC at a single synapse become unavailable, reducing the amplitude of the subsequent EPSC (Auger & Marty, 2000; Crowley *et al.*, 2007; Malagon *et al.*, 2016). To calculate the degree of amplitude occlusion, I plotted the normalized amplitudes of the events as a function of the time interval since the preceding events during a train of stimuli. There was a clear trend of mEPSC amplitude reduction as the interval decreased, indicating the amplitude occlusion. I then approximated the occlusion at a time interval of 0 (for overlapping mEPSCs) by extrapolation of an exponential curve fitting the plot (Fig. 9D; amplitude occlusion = 0.18 for the average plot). The average value of amplitude occlusion across experiments was 0.13 ± 0.18, indicating that amplitudes of subsequent events with a short time interval became ~80% of the amplitudes without amplitude occlusion. Amplitude occlusion mostly ranged from ~0.3 to 0 in the experiments. Therefore, I decided to split events into two or three events, when the amplitude were1.7-2 and 2.4-3 times larger than definitive mEPSC amplitude, respectively. In other words, the events whose amplitudes are larger than the threshold (1.7-2) were classified as simultaneously occurring two events (Fig. 9C, right). If they were larger than the second threshold (2.4-3), I classified them as containing three events. Note that the thresholds depended on the respective percentages of amplitude occlusion in the individual synapses. Altogether, these results

showed that I could adequately apply the deconvolution method to single hMF-SLIN synapses with appropriate corrections to detect individual vesicular events.

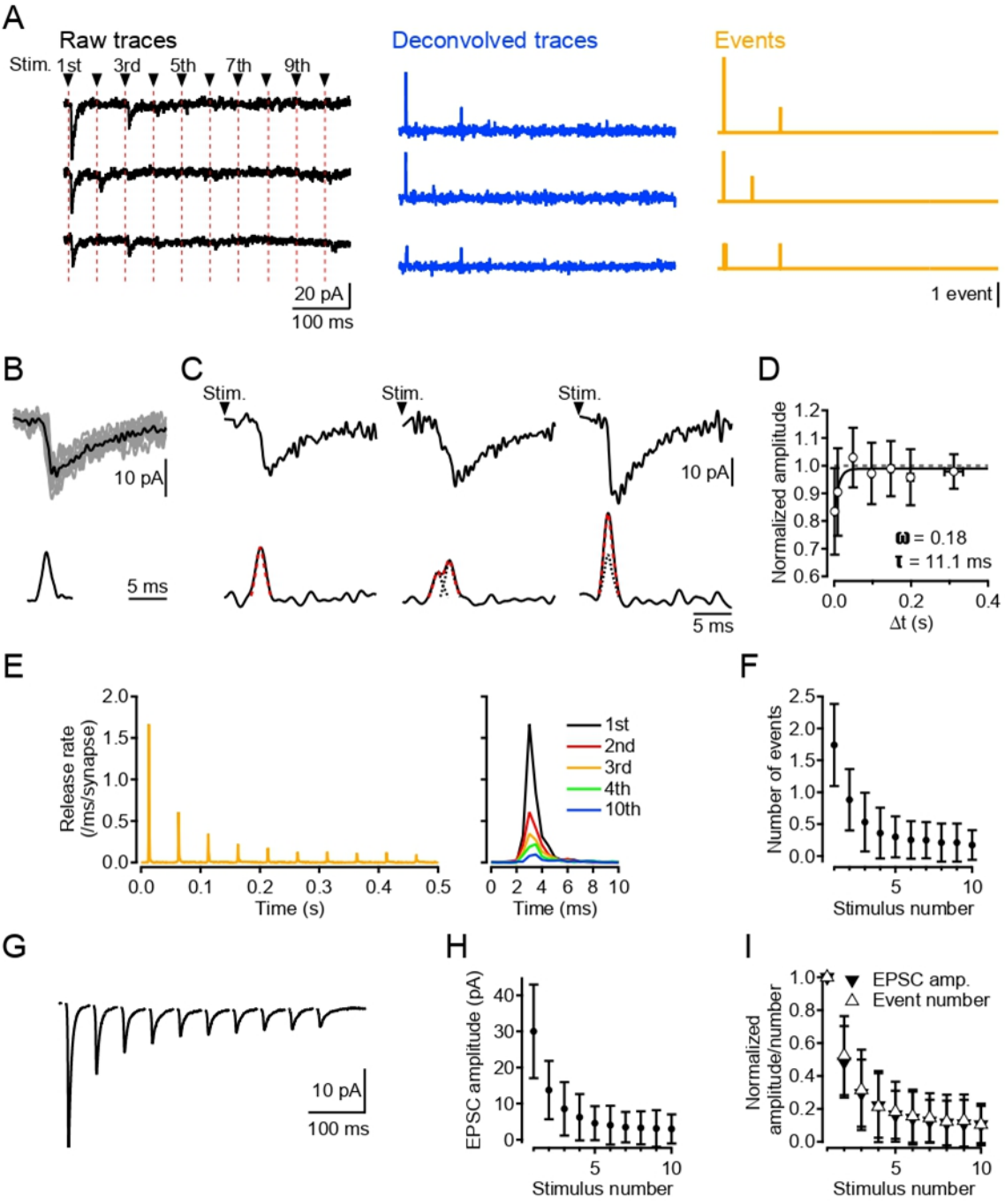

Figure 9 Detecting synaptic vesicular events from synaptic responses at single hMF-SLIN synapses.

(A) Representative recordings from a single hMF-SLIN synapse. Individual EPSC responses (black) to presynaptic action potential stimuli (stim.), deconvolved traces using quantal EPSC as kernel (blue), and detected events by analyzing the deconvolved traces (yellow) are shown. (B) Quantal EPSCs from the same

experiment were aligned and averaged. The average mEPSC was fitted with a sum of three exponentials. The filtered version of the mEPSC (single spike) was obtained by applying a matched filter calculated from the three-exponential fit. (C) Examples of individual EPSCs applying the same matched filter to detect vesicular events. A filtered signal is fitted with spike-shaped curve having appropriate time positioning and vertical scaling (dotted red curve, left). A broader signal can be decomposed into two components (dotted black curves; dotted red curve is the sum of the two components; middle). A large signal which has >1.7 times larger amplitude than the single spike is treated as a double event (dotted black curve is a single spike from the average mEPSC; dotted red curve is the fitted spike; right). (D) A plot of the normalized amplitude of EPSCs that are detected as single vesicular events as a function of the time since the previous event (Δt, n = 17). Extrapolation of the model exponential curve to $\Delta t = 0$ suggests a maximum amplitude occlusion $\omega = 0.18$. (E) Left, an average release rate per synapse was calculated from the latency of the detected events (n = 17). Right, release rates for the 1^{st}, 2^{nd}, 3^{rd}, 4^{th} and 10^{th} responses are superimposed. Time of 0 ms shows the time of individual stimulations. (F) The number of events occurring within 10 ms after individual stimulations were plotted as a function of stimulus number (n = 17). (G) An average response to 20 Hz trains at single hMF-SLIN synapses. (H) Plots of the EPSC amplitude as a function of stimulus number. (I) Plots of the normalized EPSC amplitude (filled inverted triangles) and the normalized event number (open triangles) as a function of stimulus number (n = 17). Error bars show SD.

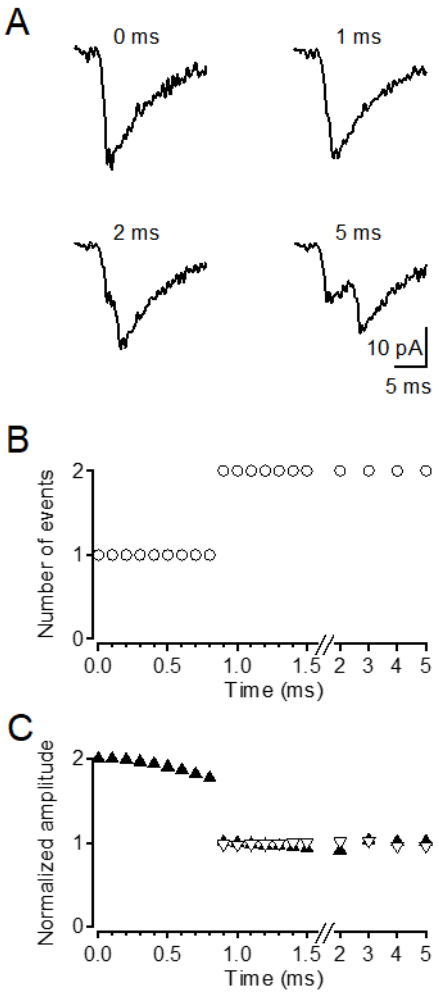

Figure 10 Time resolution of the event detection.

(A) Two average mEPSCs in an example experiment were artificially added together with time intervals of 0-5 ms. The event detection procedure was run on these traces to determine the minimum interval required for event disambiguation. (B) The traces composed of two mEPSCs with time intervals of < 0.9 ms were detected as a single event. The procedure correctly discerned 2 events with a separation of ≥ 0.9 ms. (C) The amplitudes of the detected events were normalized by the amplitude of the average mEPSC (filled triangles: amplitudes of the first detected EPSCs; open triangles: amplitudes of the second detected EPSCs, when applicable).

3.3.4 Analysis of synaptic depression using vesicle numbers

Here, I compared the extent of synaptic depression between the number of released vesicles and EPSC amplitudes. I counted the released SVs detected by the deconvolution analysis in response to the

individual stimuli. Figure 9E shows the time course of the detected events. Most of vesicular events occurred within 10 ms after each stimulation. Hence, I counted the number of the events occurring during the 0-10 ms period as the event number for each stimulus. The event numbers and the peak EPSC amplitudes were plotted against the stimulus number, both showing strong depression (Fig. 9F-H). To evaluate the extent of depression, I obtained ratios of the 2nd and the 5th response to the 1st response from the event numbers (s_2/s_1 or paired pulse ratio (PPR): 0.52 ± 0.24, s_5/s_1: 0.18 ± 0.18; s_i: the number of released events for the i-th stimulus) and from the peak EPSC amplitudes (PPR: 0.49 ± 0.22, EPSC5/EPSC1: 0.16 ± 0.15). I found no significant differences of these ratios between the two methods (Fig. 9F, H). When comparing the normalized EPSC amplitudes and the normalized event numbers, the time courses of depression were almost identical (Fig. 9I). The similar degree of depression between the two plots suggests that the peak EPSC amplitudes in response to individual stimuli are proportionally related to the corresponding numbers of release events. These results indicated the extent of depression estimated from EPSC amplitudes (=NPQ) and that from the number of vesicular events (=NP) during a stimulation train is virtually identical under 3 mM external calcium condition. Therefore, it was suggested that Q has little effect on synaptic depression in these synapses.

3.3.5 Changes in Q have little effect on synaptic depression

The proportional relationship between the peak EPSC amplitudes and the numbers of vesicular events

during the stimulus train raises the question as to why amplitude occlusion, which would occur at the first stimuli, does not distort the relationship. The amplitudes of EPSCs in response to the first stimulus should be reduced by perhaps 20% (as indicated by the amount of amplitude occlusion for 2 consecutive events), because multiple vesicular events were often observed in the first responses (Fig. 9). Then, the comparable results from EPSC amplitude and vesicle count indicate that the quantal size after the second stimulation should also be reduced equally, perhaps due to postsynaptic receptor desensitization. Indeed, in other synapses, in addition to the amplitude reduction by amplitude occlusion, another reduction due to cumulative desensitization of postsynaptic receptors was observed during a train (Trussell *et al.*, 1993; Otis *et al.*, 1996; Taschenberger *et al.*, 2005; Malagon *et al.*, 2016). Therefore, I next examined whether quantal size reduction during a train was observed at hMF-SLIN synapses. Figure 11A shows amplitude distributions of the first vesicular events in a train, and of later events during a train after collecting the amplitude occlusion. In the example, the amplitude histogram of the first events displayed higher mean and lower coefficient variation (CV), compared with the amplitude histogram of successive events (Fig. 11A). Note that double and triple events have excluded from the first event results. Group results demonstrated that there was a significant difference in the mean amplitudes (23.2 ± 8.7 pA and 18.5 ± 6.3 pA for first and train events, respectively; $P = 0.00001$, paired *t*-test), and in the mean CVs (0.25 ± 0.11 and 0.33 ± 0.04 for first and train events, respectively; $P = 0.027$, paired *t*-test, Fig. 11B), indicating that

quantal size decreased to 80% during a train. Because the percentage of the quantal size reduction was similar to that of amplitude occlusion that mainly influenced the amplitude of the first response, these results suggest that amplitude occlusion and quantal size reduction after the first response reduced the amplitudes of all responses in a train by ~20%, so that the reductions of the quantal amplitudes were roughly counterbalanced among responses. This also suggests that the reduction of the quantal amplitudes, presumably from postsynaptic changes, apparently had little effect on the extent of synaptic depression at hMF-SLIN synapses under this condition, indicating that synaptic depression should be mediated by presynaptic mechanisms.

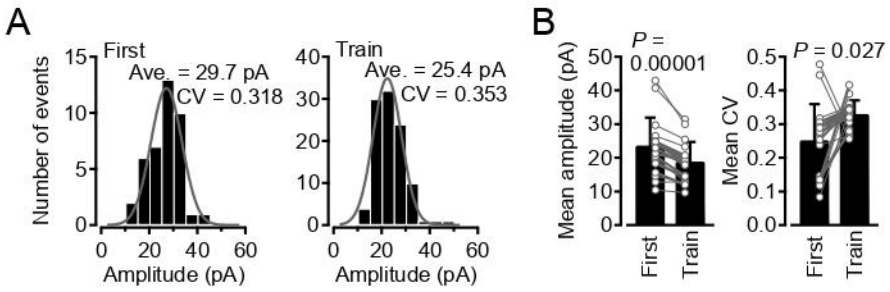

Figure 11 Quantal size reduction during trains at single hMF-SLIN synapses.

(A) Examples of amplitude histograms with Gaussian fits, for the first single events in trains (left) and the other single events during trains (right). (B) Group data from 17 single synapse experiments showing mean and CV of peak amplitudes for the first single events, and train events (after correction for amplitude occlusion from previous events; circles: individual experiments). First events have larger mean amplitude and smaller CV than train events (P = 0.00001 and P = 0.027 for mean amplitude and CV, respectively; paired t-test, n = 17). Error bars show SD. Results from same cells are linked together with lines.

3.3.6 Contribution of presynaptic parameters to the synaptic depression

Because it was suggested that Q has little effect, synaptic depression should be determined by other

presynaptic factors (N and P). To investigate determining factors of released vesicle numbers potentially related to synaptic depression, I next examined the docking site number (N) and the release probability (P) at single hMF-interneuron synapses using variance-mean analysis of vesicle counts (Clements & Silver, 2000; Malagon *et al.*, 2016). In the variance-mean analysis using SV counts, the mean amplitude m is replaced by $\langle s_i \rangle$, where s_i is the variable for the number of released vesicles after the $_i$th stimulation, and the expected value (or mean) and variance of s_i follow the relations:

$$\langle s_i \rangle = NP_i$$

$$\text{var}\,(s_i) = NP_i\,(1 - P_i)$$

where N is the number of docking sites with one vesicle at most, and P_i is the probability of one docking site releasing one vesicle at the i-th stimulus. Therefore:

$$\text{var}\,(s_i) = \langle s_i \rangle\,(1 - \langle s_i \rangle / N) = -1 / N\langle s_i^2 \rangle + s_i$$

Hence, the model parabola intersects the x axis at the origin and at the docking site number (N), and has an initial slope of 1, whereas its slope equals the quantal size in classical variance-mean analysis using EPSC peak amplitudes (Malagon *et al.*, 2016; Miki, 2019). Figure 12A shows an example matrix of the number of released vesicles as a function of stimulus number (rows) and sweep number (columns). The variance and mean of the number of vesicles for each stimulus were calculated across sweeps, and plotted in Figure 12B. The parabolas having an initial slope of 1 fitted the variance-mean plots, providing N values of 1.68 and 2.62 for the example and average data, respectively (Mean ±

SD: 2.68 ± 1.13, n = 17, $N_{parabola}$). By dividing the mean values of s_1 by N, I obtained the release probabilities per docking site for the first stimulus, P_1 = 0.74 and 0.66 for the example and average data, respectively (Mean ± SD: 0.66 ± 0.17, n = 17, $P_{1,parabola}$). The N and P_1 values can also be calculated by another analysis in which vesicular release number distribution is fitted with a binomial model, when P_i is sufficiently high (Korn *et al.*, 1981; Redman, 1990; Malagon *et al.*, 2016). In Figure 12C, the probability distributions of vesicle counts for the first stimulus in a train, where P was expected to be high, were compared with predictions from the binomial model, providing N values of 2 and 3, and P_1 values of 0.58 and 0.5 for the example and average data, respectively ($N_{binomial,1st}$: 2.65 ± 1.17, $P_{1,binomial}$: 0.63 ± 0.17, n = 17). Both mean values of N and P_1 were similar to those calculated from the variance-mean plots. Comparing N and P_1 values obtained with parabolic fits and binomial fits, I found that the two sets of values were significantly correlated and that both plots were fitted with lines having slopes of ~1, indicating that the values obtained by the two methods were consistent (Fig. 12D, E). Altogether, N values ranged from 1 to 5, while P_1 values ranged from 0.37 to 0.9 at hMF-SLIN synapses.

To examine whether N values change during synaptic depression, the binomial method is useful, as N can be measured at the first and second stimuli. So, I compared $N_{binomial}$ from the vesicle counts for the first and second stimuli (Fig. 12C). The binomial fits of example and average data provided the same N values from the second as those from the first. Group analysis indicated no significant

difference ($N_{binomial,2nd}$: 2.35 ± 1.22, vs $N_{binomial,1st}$ $P = 0.31$, paired *t*-test, Fig. 12F). Moreover, Figure 12B shows that all points were close to the fitted parabolas. These observations were consistent with unchanged N values during trains.

Next, I examined whether P_i changes. For each stimulus number i, the release probability was calculated assuming a constant N value from:

$$P_i = \langle s_i \rangle / N,$$

and was plotted in Figure 12G. The release probability gradually decreased to 0.10-0.15 with stimulus number until the 5th stimulation, and then reached the steady state ($P \approx 0.08$). These results suggest that the gradual decrease of the release probability during trains without a change in the docking site number causes the decrease of the number of events, leading to synaptic depression at hMF-SLIN synapses.

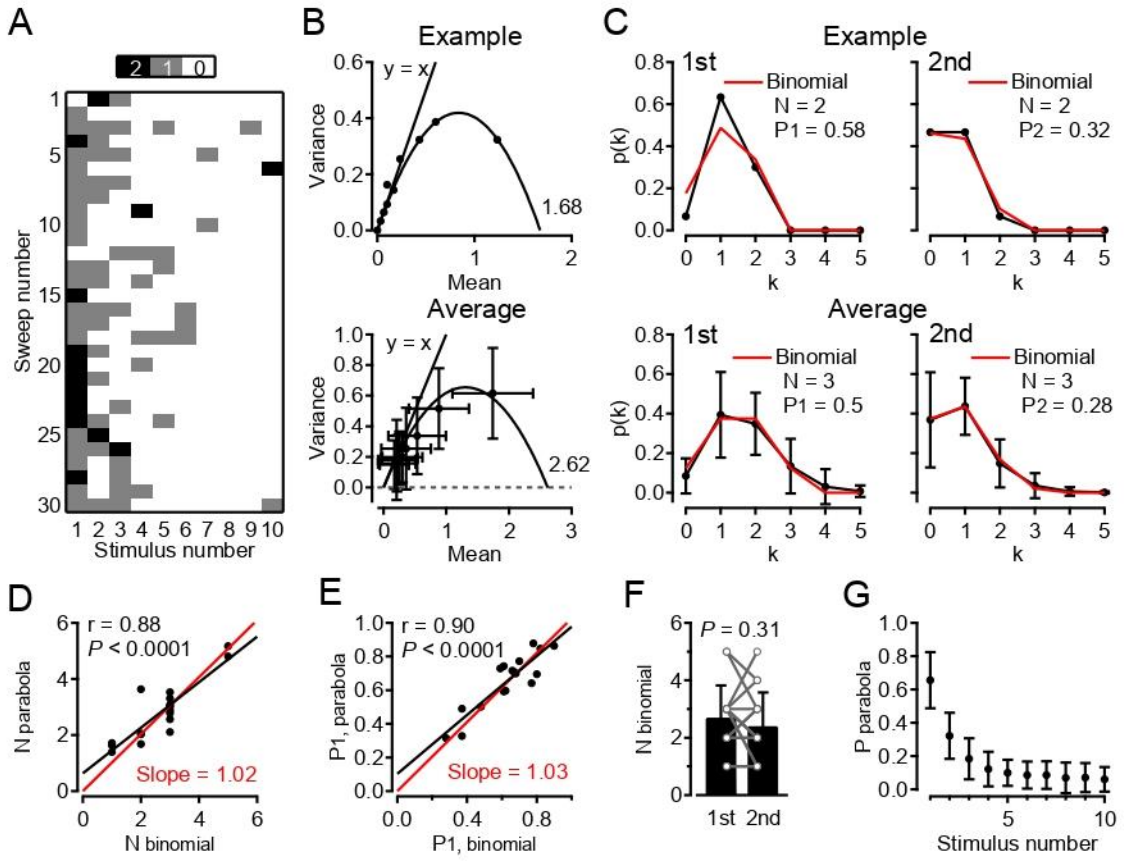

Figure 12 Estimating the number of docking sites and the release probability at hMF-SLIN synapses.

(A) An example of matrix of vesicular release counts as a function of stimulus number (columns; 20 Hz stimulation) and trial number (rows) in a single synapse experiment. Black, gray, and white colors show 2, 1, and 0 events, respectively. (B) The variance-mean plots of the number of released vesicles for each stimulus number and parabolic fits with y = x reference lines, provided numbers N = 1.68 and 2.62 of releasing units and the release probability for the first stimulus P_1 = 0.74 and 0.64 for the example (top) and the average data (bottom, n = 17), respectively. Error bars show SD. (C) The probability distributions $p(k)$ to observe k vesicular release events are shown for the first and second stimuli in B. Binomial fits (red) provided numbers N = 2 and 3 of releasing units, the release probability P_1 = 0.58 and 0.5 and P_2 = 0.32 and 0.28 for the example (top) and the average data (bottom, n = 17), respectively. Error bars show SD. (D) A plot of the N values obtained by the variance-mean analysis, as a function of binomial N values obtained from the vesicle counts for the first stimulus by the method shown in C. The N estimates are significantly correlated (black regression line; P = 0.000003), and the regression line through the origin has a slope of 1.02, close to 1 (red). (E) Corresponding plot of the first release probability (P_1) with the two methods. The two estimates are also significantly correlated (black regression line; P = 0.000001), and the regression line through the origin has a slope of 1.03, close to 1 (red). (F) Comparison of binomial N values obtained from the probability distributions of SV counts for the first and second stimuli (P = 0.31, paired t-test; n = 17). Results from same cells are linked together with lines. (G) Plots of the release probabilities obtained by the variance-mean analysis as a function of

stimulus number for the average data (n = 17). Error bars show SD.

3.3.7 Estimations of δ and p values using stochastic properties of the cumulative numbers of released vesicles

The experimental results so far suggested that the release probability, P, was the responsible factor for synaptic depression. As described before, the release probability is the product of the probability of the docking site occupancy (δ) and the release probability of a docked SV (p). Thus, I next attempted to estimate δ and p separately to clarify which accounts for the P reduction and contributes to synaptic depression at hMF-SLIN synapses.

To obtain information about the above parameter values, I first examined the cumulative number of vesicles counts because the stochastic properties of the cumulative number of events provide clues for an appropriate release model and parameter values (Miki *et al.*, 2016; Miki, 2019). In cerebellar and cortical excitatory synapses, this analysis allowed the establishment of a novel model of vesicle dynamics (Miki *et al.*, 2016, 2018; Doussau *et al.*, 2017; Pulido & Marty, 2018; Blanchard *et al.*, 2020; Bornschein *et al.*, 2020). In the model, named the two-step model, the docking sites were replenished by associated sites called replacement sites with a probability of r during an inter-AP time interval. The replacement sites were also replenished by an infinite pool called a recycling pool with a probability of s (Miki et al., 2016; Fig. 14A). If the hMF-SLIN synapses are similar, I should observe substantial deviation of the data points from parabola. In Figure 13, an example showed that the

variance-mean plot for the cumulative number (open squares) deviated from the previously described parabola starting at the 2nd point, then gradually departed from the parabola, and eventually approached a linear relation with a slope of 0.47 (filled circles: the standard variance-mean plot, as in Figure 12B). Similarly, the average cumulative plot also departed from the parabola at the 2^{nd} point, approaching a linear relation with a slope of 0.53 (Mean ± SD: 0.57 ± 0.26, n = 17). Note that the values for the average plots were normalized to a N value of 2 (see Methods). These results are consistent with the two-step model.

Next, I compared the cumulative plots in the experimental data and in simulation using the two-step model (Fig. 14). In the model without SV replenishment of the docking sites, the cumulative plot (filled squares) stayed along the parabola fitting the standard variance-mean plot (open circles; Fig. 14A). In such a case, only vesicles that were initially docked were released during trains, so that the maximum mean value of the cumulative numbers of events was limited by the probability of the initial site occupancy. Therefore, I next chose the model with replenishment. Figure 14B shows that a least-squares fit of the cumulative plot of the data with the model provided the best combination of the parameter values (δ: 0.85, p: 0.8, r: 0.15, s: 0.2, and N: 2). In the simulation result, the cumulative plot deviated from the parabola at the 2^{nd} point and became linear at the 7^{th}-8^{th} points. The slope of the final linear fit was 0.43, indicating that the model reproduced the data well.

To further examine the validity of the simulation, I estimated the number of released events for

each stimulus (s_i), the covariance between s_i and s_{i+1} and the covariance between S_i and s_{i+1}, each time comparing experimental data and simulation results using the same combination of parameter values as in Figure 14B (Fig. 14C, D). Here s_i is the number of released vesicles for the i-th stimulus, while S_i is a sum of successively released vesicles, defined as $S_i = s_1 + s_2 + \ldots + s_i$. The definitions of covar(s_i, s_{i+1}) and covar(S_i, s_{i+1}) are $\langle s_i - \langle s_i \rangle \rangle \langle s_{i+1} - \langle s_{i+1} \rangle \rangle$, and $\langle S_i - \langle S_i \rangle \rangle \langle s_{i+1} - \langle s_{i+1} \rangle \rangle$, respectively. The two types of covariance provide detailed information about the synaptic parameters and constrain release models (Vere-Jones, 1966; Quastel, 1997; Scheuss & Neher, 2001; Miki *et al.*, 2016). Comparison of the plots of the event numbers demonstrated that the number of events for the first stimulus (s_1), the PPR (s_2/s_1), and the ratio of s_5 to s_1 (s_5/s_1) in simulation results were comparable to those in the experimental data (s_1: 1.36 vs 1.31 ± 0.34, PPR: 0.35 vs 0.52 ± 0.24, s_5/s_1: 0.17 vs 0.18 ± 0.18 for simulation results vs experimental data; Fig. 14C). The plots for covariance between s_i and s_{i+1} and between S_i and s_{i+1} were also similar to those in experimental data as shown in Figure 14D. The values of the first, second and steady-state points for covariance between s_i and s_{i+1} were -0.157 vs -0.122 ± 0.092, -0.033 vs -0.023 ± 0.055 and -0.014 vs -0.007 ± 0.018 for simulation results vs experimental data, respectively. The second and steady-state values for covariance between S_i and s_{i+1} were -0.063 vs -0.061 ± 0.056, and -0.048 vs -0.014 ± 0.026, respectively. The steady-state values for covariance were slightly smaller in data. Nevertheless, these results suggested that satisfactory fits of the plots were provided by the two-step model with the δ value of 0.85 and p value of 0.8 at

hMF-SLIN synapses.

I further looked into the simulated cumulative plots to extract information about δ values using various analytical approaches. The simulation indicates that (i) the mean value of the cumulative number was limited by δ in the case of no vesicle replenishment (Fig. 14A) and that (ii) the cumulative plot departed from the parabola linearly with a slow replenishment rate (Fig. 14B). Together these results suggested that the consumption of the initially docked SVs and the release of the slowly recruited SVs during trains corresponded to the parabolic part and to the linear part in the cumulative plot, respectively. The interpretation of the cumulative plot as composed of these two components led us to the proposal that the point where the regression line for the cumulative plot intersected the parabola represents the initial occupancy probability. In fact, the intersection point between the fitted line and the parabola in the simulation indicated a probability of 0.77, close to the constrain occupancy probability of 0.85 (Fig. 14B). To test the validity of this proposal, I performed simulations with various recruitment rates and then calculated the percentage errors between the estimates obtained from the intersection points to 0.85 (Fig. 14E). With a combination of $\delta = 0.85$ and $p = 0.8$, I could obtain correct estimates of the occupancy probability with <10% errors provided that $r \leq 0.3$ and $s \geq 0.2$, that is, the rate constant of SV replenishment to a docking site was less than 7.13 s^{-1}. These simulation results suggested that by the "line-parabola intersection" approach, I could directly estimate the probability of the site occupancy from the cumulative plots in the experimental

conditions where the docking sites have high occupancy probability and high release probability with low recruitment rate. The model simulation for data indicated that a maximum rate constant of SV replenishment was 3.25 s^{-1} at hMF-SLIN synapses (Fig. 14B). The rate constant obtained from a line fit of cumulative number in data for Figure 9F was 1.57 s^{-1} later in a train, indicating a sufficiently low recruitment rate at the synapses to apply the "line-parabola intersection" approach. In Figure 14, using the approach I obtained occupancy probabilities of 0.89 and 0.85 by dividing the mean values of the intersection points (1.50 and 1.70) by the docking site numbers (1.68 and 2.0) for the example and average data, respectively (δ: 0.84 ± 0.11, n = 17). In addition, I obtained the release probability of a docked SV (p: 0.78 ± 0.15, n = 17) by dividing the release probability (P) for the first stimulus by the δ estimate. The δ estimates ranged from 0.64 to 1.00, while the p estimates ranged from 0.46 to 1. The average values of the estimates were close to those values in the simulation result (δ: 0.85, p: 0.8). These results indicated that the initial occupancy probability (≈ 0.85) and the release probability of a docked SV (≈ 0.8) can be directly estimated from the cumulative plot by the "line-parabola intersection" approach. These parameters could not be estimated by previous approaches.

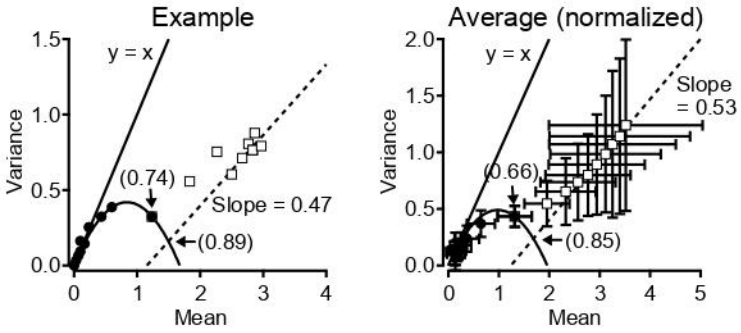

Figure 13 Stochastic properties of the cumulative number of vesicular events.

The variance-mean plots of the direct number (filled circles) and cumulative number (open squares) of released vesicles for an example experiment (left, same experiment as in Figure 12) and a group of 17 experiments (right). The plots for the number of released vesicles were fitted with parabolic curves. The variance points for the cumulative number depart from the parabolas to approach lines with slopes of 0.47 and 0.53 in the example and average plots, respectively. The lines crossed the parabolas at points where the mean values are 1.50 and 1.70, indicating that the estimated initial occupancies at the docking sites are 0.89 (N = 1.68) and 0.85 (N = 2) in the example and average data, respectively. When averaging, I scaled individual data to N = 2, because the mean and variance values were proportional to N values. Error bars show SD.

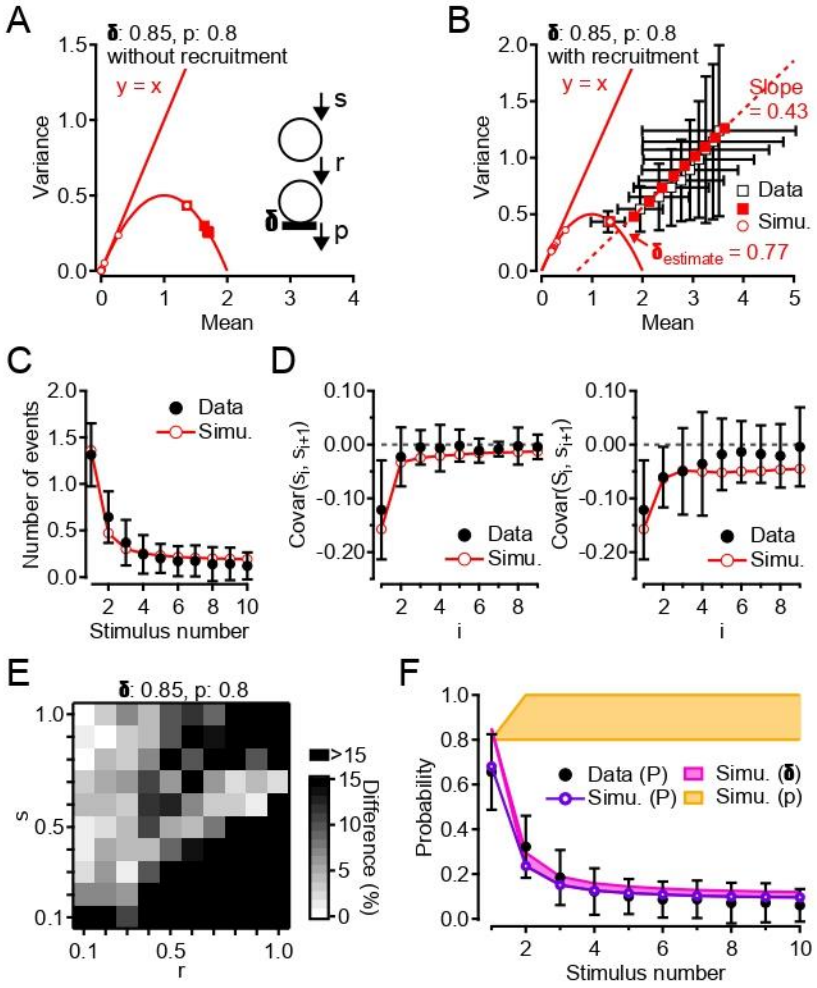

Figure 14 Estimating the initial occupancy using cumulative number of vesicular events.

(A) Stochastic properties of the direct number (open circles) and cumulative number (filled squares) of events in two-step model without replenishment to docking sites. I assumed two independent docking sites in the model (N = 2). (B) A least-squares fit of the cumulative plot with the two-step model provided the parameter values (δ: 0.85, p: 0.8, r: 0.15, s: 0.2 and N: 2; circles: the standard variance-mean plots, squares: the cumulative number plots). The last 4 points for the cumulative number were fitted with a line having a slope of 0.43. The

fitted line and the parabola crossed at a point with a mean value of 1.54, providing an initial occupancy value of 0.77, close to 0.85 which is the parameter value from the model. The cumulative plot of data is the same plot as in Figure 13 (open squares). (C and D) The two-step model with same values of parameters as those in B, well reproduced the number of events, covariance calculated between consecutive counts (s_i, s_{i+1}), and covariance between the cumulative count S_i and the count s_{i+1} (i: stimulus number). All experimental data were normalized to N = 2 to compare the absolute values with those from the model simulations. (E) A matrix displays the percentage errors between the estimated value and the parameter value of the probabilities of the site occupancy in the model (column: a transition probability of r; row: that of s). The parameter values of the occupancy (δ) and release probability (p) were fixed to 0.85 and 0.8, while the transition probabilities (r and s) were changed from 0.1 to 1 with an interval of 0.1. Better estimations were predicted in the condition where the r value was low. (F) Simulated parameter values (P, δ, and p) and P values obtained from data (same plot as in Figure 12G) are plotted as a function of stimulus number. Possible range of δ and p values are filled with colors. The reduction of P value reflects that of δ value, irrespective of constant or increased p.

3.3.8 δ determines the extent of synaptic depression

Although we could estimate δ and p at the first stimulus, it was uncertain how these parameters change during repetitive stimulation. I then asked which parameters (δ or p) determined the reduction of the release probability (P) that was responsible for synaptic depression. In the simulations presented so far, the release probability per docked SV (p) was assumed to be constant during trains. However, since p should directly be affected by local [Ca^{2+}], changes in [Ca^{2+}] during a stimulation train would change p. Presynaptic Ca^{2+} imaging showed that during train stimulations Ca^{2+} transients at hMF boutons were either constant or increased with stimulus number due to the accumulation of residual Ca^{2+} and the increase of Ca^{2+} influx by AP broadening (Regehr *et al.*, 1994; Geiger & Jonas, 2000; Pelkey *et al.*, 2006). Therefore, the peak local [Ca^{2+}] at hMF synapses were expected to be stable or to slightly increase with stimulus number. And thus, the p value was expected to be constant or if

anything increasing, but not decreasing. Consistent with this expectation, when assuming constant δ with reducing p during trains in the model, the simulated cumulative plot and covariance failed to fit the data (Fig. 15). Especially, the first negative covariance observed experimentally was consistent with a reduction of δ rather than p (Figs. 14 and 15; Miki et al., 2016; Scheuss & Neher, 2001). Therefore, it is likely that δ rather than p decreases during synaptic depression.

Short-term depression is thought to be mediated, at least in part by depletion of the RRP. The mechanism underlying the RRP depletion has been unclear, because separation between a decrease of the number of docking site (N) and that of the number of docked vesicles (δ) has been difficult experimentally. Foster and Regehr (2004) have suggested N decreases during the stimulus train. In addition, in this study, I estimated these parameters separately by using novel fluctuation analysis and model simulation. In the analysis of SV counts shown in Figure 12, I revealed that N did not change between 1st and 2nd stimuli. However, there is still a possibility that N changes after first two stimuli, because I cannot estimate N accurately under low release probability condition. To test this, I assumed in the model simulations that N decreased to 1 while p increased to 1 toward the 3rd stimuli (Fig 16) to counter the N reduction. The simulation with decreasing N during trains provided worse fits of the cumulative plot and of the covariance plots compared with that with unchanged N (Figs. 14 and 16). Additionally, in the case of increasing N during trains, instead of decreasing N, model simulations have shown that the slope of the linear fit for cumulative plot can be expected to become larger, at

most 1, because release events tend to follow a Poisson process as N increases (Miki, 2019). This is not consistent with my data. Thus, the stochastic properties of cumulative event number were also consistent with unchanged N during trains at the synapses.

Figure 14F shows the simulation results of the P, δ and constant/increased p values, and the experimental result of the P value. In the case of unchanged N, the simulated P values showed depression similar to those from the experimental data. Because of the constant/increased p value, the reduction of the release probability (P) with stimulus number mainly reflected the reduction of the occupancy probability (δ; Fig 14F). Overall, the results suggest the following: (i) The initial occupancy was high, (ii) δ mainly decreases during the stimulus train, resulting in the decrease of the total release probability (P), and synaptic depression at hMF-SLIN synapses. (iii) p is most likely not decreased.

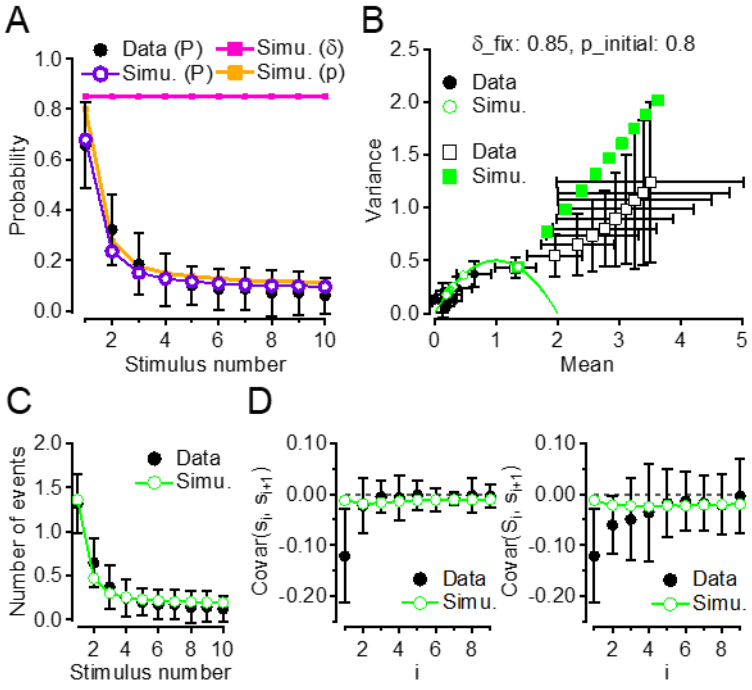

Figure 15 Model simulations with constant δ and variable p.

(A) Simulated parameter values (P, δ, and p; simulated P plot same as in Figure 14F) and experimental P values (same plot as in Figure 12G) are plotted as a function of stimulus number. Instead of p, δ was assumed to be constant. The p values were calculated by dividing P by δ. (B) Simulated variance-mean plots using constant δ and variable p. The simulated variance-mean plot of the number of events (open circles) showed the same pattern as the simulated one in Figure 14B, and was fitted with a parabola (N = 2). The simulated cumulative plot (filled squares) departed more markedly from the parabola, compared with the simulated plot in Figure 14B, because the docked vesicles were never consumed in this model. (C) The plot of the number of events as a function of stimulus number in the simulation showed the same pattern as that in Figure 14C. (D) Simulation results of covariance calculated between consecutive counts (s_i, s_{i+1}), and covariance between the cumulative count S_i and the count s_{i+1} (i: stimulus number). Negative covariance predicts a compensatory mechanism such that if the number of released events for a given stimulus is larger than the average, the number for the subsequent one becomes smaller, and vice versa. Basically, docking site occupancy creates a negative correlation (Scheuss & Neher, 2001; Miki et al. 2016). Relatively large negative covariance between s_1 and s_2 (or between S_1 and s_2) in the experimental results suggested a large decrease in δ upon the first stimulus and a slow recovery of δ after the stimulus. By contrast, the first negative covariance almost disappeared in the model because of the constant δ during a train. All experimental data are as in Figure 14. Error bars show SD.

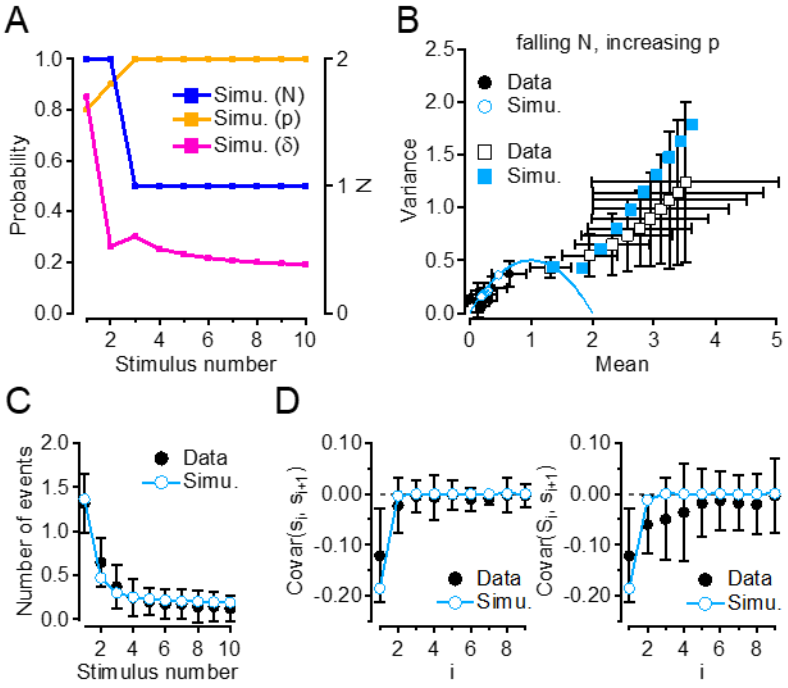

Figure 16 Model simulations with reducing N and increasing p during trains.

(A) Simulated parameter values (N, δ, and p) are plotted as a function of stimulus number. I assumed that

the N value decreased to 1 at the 3rd stimuli, while the p value lineally increased to 1 at the 1st - 3rd stimuli. The δ values were calculated by dividing the simulated numbers of events by the product of N and p values. (B) Simulated variance-mean plots using the parameter values shown in A. The simulated variance-mean plot of the number of events (open circles) showed the same pattern as the simulated one in Figure 14B, and was fitted with a parabola (N = 2). The simulated cumulative plot (filled squares) showed a worse fit, compared with the simulated plot in Figure 14B. (C) The plot of the number of events as a function of stimulus number in the simulation showed the same pattern as that in Figure 14C. (D) Simulation results of covariance calculated between consecutive counts (s_i, s_{i+1}), and covariance between the cumulative count S_i and the count s_{i+1} (i: stimulus number). Compared with the experimental results, larger negative covariance between s_1 and s_2 (or between S_1 and s_2) in the simulated results was obtained because the 2nd response more largely depends on the remaining δ after the first stimulus due to higher p at 2nd stimuli. The negative covariance almost disappeared at i = 2, because history of usage of SVs at a docking site was cleared when decreasing N at 3rd stimuli. All experimental data are as in Figure 14. Error bars show SD.

3.3.9 Changes of δ with $[Ca^{2+}]_o$ affect synaptic plasticity

I so far clarified the contribution of synaptic parameters, especially δ, to synaptic depression in 3 mM Ca^{2+} condition at hMF-SLIN synapses. However, I have not yet considered the contribution in lower Ca^{2+} conditions (Borst, 2010). The release probability (P) is regulated by $[Ca^{2+}]_o$, shaping short term synaptic plasticity (Zucker & Regehr, 2002). It was usually assumed that p is the one mainly determined by $[Ca^{2+}]_o$. However, a recent study indicated that initial δ may change $[Ca^{2+}]_o$ at different at cerebellar synapses (Malagon *et al.*, 2020). Therefore, there is a possibility that δ changed with lower $[Ca^{2+}]_o$ affects the extent of synaptic plasticity at hMH-SLIN synapses. However, it remained unknown whether δ changes with $[Ca^{2+}]_o$ at synapses in the forebrain.

To examine which parameters are influenced by changing extracellular calcium concentration and affect the synaptic plasticity at hMF-SLIN synapses, I compared the estimated synaptic parameters

between 3 mM and 2 mM $[Ca^{2+}]_o$ conditions. In the same way as in Figure 9, I recorded EPSCs using train stimulation with 2 mM $[Ca^{2+}]_o$ at single hMF-SLIN synapses, and then counted SV numbers by deconvolution for quantitative analysis (Fig. 17 and Fig. 18). In the 2 mM Ca^{2+} condition, the ratio s of the 2nd and 5th responses to the 1st responses estimated from both the peak EPSC amplitudes (PPR: 1.50 ± 2.13, s_5/s_1: 1.29 ± 2.19, n = 9) and the event numbers (PPR: 1.12 ± 0.74, s_5/s_1: 0.98 ± 1.17, n = 9) were larger than those in 3 mM Ca^{2+} condition (vs 3 mM $[Ca^{2+}]_o$; PPR: $P = 0.004$ and $P = 0.004$, s_5/s_1: $P = 0.008$ and $P = 0.004$ for EPSC amplitude and event number, respectively; Wilcoxon singed rank test), showing less depression (Fig. 17B). That was mainly caused by the reduction of the EPSC amplitude and event number for the 1st response in 2 mM $[Ca^{2+}]_o$ EPSC amplitude for the 1st response: 30.0 ± 12.9 pA vs 13.7 ± 7.5 pA for 3 mM vs 2 mM $[Ca^{2+}]_o$; $P = 0.002$, unpaired *t*-test; event number for the 1st response: 1.74 ± 0. 64 vs 0.90 ± 0. 46 for 3 mM vs 2 mM $[Ca^{2+}]_o$ $P = 0.002$, unpaired *t*-test). Variance mean analysis using SV counts and binomial fits of the probability distribution of SV counts revealed that N values did not change as a function of $[Ca^{2+}]_o$ ($N_{parabola}$: 2.92 ± 1.04 vs 2.41 ± 1.40 , $N_{binomial}$ 3 .00 ± 1.32 vs 2.63 ± 1.06 for 3 mM vs 2 mM $[Ca^{2+}]_o$; $P = 0.07$ and $P = 0.35$ for $N_{parabola}$ and $N_{binomial}$, respectively; paired *t*-test n = 7 and 8 for $N_{parabola}$ and $N_{binomial}$, respectively), while P_1 values became smaller in 2 mM $[Ca^{2+}]_o$ ($P_{1,parabola}$: 0.69 ± 0.17 vs 0.50 ± 0.31, $P_{1,binomial}$: 0.62 ± 0.18 vs 0.37 ± 0. 24 for 3 mM vs 2 mM $[Ca^{2+}]_o$; $P = 0.044$ and $P = 0.004$ for $P_{1,parabola}$ and $P_{1,binomial}$, respectively; paired *t*-test n = 7 and 8 for $P_{1,parabola}$ and $P_{1,binomial}$, respectively; Fig. 17C, D). Quantal

sizes for both the first and train events did not change (first: 21.9 ± 3.3 pA vs 21.2 ± 3.9 pA, train: 17.3 ± 2.9 pA vs 17.1 ± 3.1 pA for 3 mM vs 2 mM $[Ca^{2+}]_o$; $P = 0.17$ and $P = 0.61$ for first and train events, respectively; paired *t*-test n = 9). These results indicated that the release probability (P) changed with $[Ca^{2+}]_o$ at hMF-SLIN synapses, while N and Q did not. The reduction of P_1 was prominent in 2 mM $[Ca^{2+}]_o$ condition, leading to the decrease in the degree of depression.

To investigate impacts of δ and p on the change of P_1 with 2 mM $[Ca^{2+}]_o$, I separately estimated initial δ and p that composed P_1 using the "line parabola intersection" approach (Fig. 17E). Figure 17F demonstrated that both initial δ and p significantly decreased by around 20% in 2 mM $[Ca^{2+}]_o$ condition (δ: 0.86 ± 0.11 vs 0.72 ± 0.20, p: 0.74 ± 0.17 vs 0.56 ± 0.31 for 3 mM vs 2 mM $[Ca^{2+}]_o$; $P = 0.022$ and $P = 0.017$ for δ and p, respectively; paired *t*-test; n = 9). The best fit of the cumulative plot of the data with the two step model provided δ = 0.7 and p = 0.65 for 2 mM $[Ca^{2+}]_o$ that were smaller than those for 3 mM $[Ca^{2+}]_o$ (Fig. 19). In addition, the simulation results indicated that the δ value was able to be estimated by the "line parabola intersection" approach with around 95 % accuracy, confirming the applicability of the approach to the data obtained at 2 mM $[Ca^{2+}]_o$. In 1.2 mM $[Ca^{2+}]_o$ and 30-32°C condition, initial δ and p were 0.5 and 1 obtained by simulation (Fig. 20), indicating that p has potentials of near maximal value in more physiological conditions. These results suggested that not only p but also δ was decreased by reducing $[Ca^{2+}]_o$, resulting in the reduction of P_1. In more physiological conditions (1.2 mM $[Ca^{2+}]_o$ and 30-32°C), I obtained similar P_1 value to

that in 2 mM $[Ca^{2+}]_o$ and room temperature condition (Fig. 20).

Altogether, not only the change of p, but also that of the initial δ with $[Ca^{2+}]_o$ contributed to the extent of synaptic depression at room temperature. In addition, p may be near maximal value and only δ may contribute to depression at more physiological conditions (low $[Ca^{2+}]_o$) and high temperature. Therefore, changes in δ could contribute to synaptic depression under physiological condition.

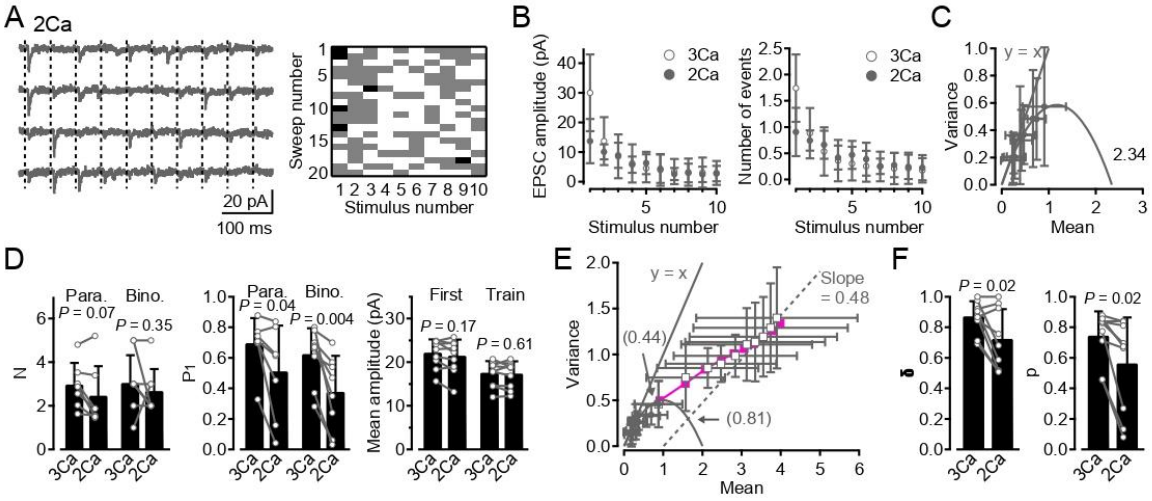

Figure 17 Estimating synaptic parameters in 2 mM $[Ca^{2+}]_o$ condition

(A) Representative recordings from a single hMF-SLIN synapse in 2 mM $[Ca^{2+}]_o$ condition. Individual EPSC responses (gray) to presynaptic action potential stimuli (20 Hz; dashed lines) are shown (left). An example of matrix of vesicular release counts as a function of stimulus (columns) and trial number (rows) in a single synapse experiment (right). Black, gray, and white colors show 2, 1, and 0 events, respectively. (B) Peak EPSC amplitude and the number of events which occur within 10 ms after individual stimulations are plotted as a function of stimulus number (n = 9 for 2Ca). The plots for 3 mM $[Ca^{2+}]_o$ are the same as those in Figure 9F and H. (C) The variance-mean plots of the number of released vesicles for each stimulus number and parabolic fits with y = x reference lines, provided numbers N = 2.34 of releasing units for the average data in 2 mM $[Ca^{2+}]_o$ condition (n =9). (D) Comparison of the values of N, P_1 and Q between 3 mM $[Ca^{2+}]_o$ and 2 mM $[Ca^{2+}]_o$. Both N parabola and N binomial obtained from 2 mM $[Ca^{2+}]_o$ are not significantly different from those from 3 mM $[Ca^{2+}]_o$ $P = 0.07$ and $P = 0.35$ for $N_{parabola}$ and $N_{binomial}$, respectively; paired *t*-test, n = 7 and 8 for

$N_{parabola}$ and $N_{binomial}$, respectively; left), while both $P_{1,parabola}$ and $P_{1,binomial}$ are significantly smaller in 2 mM $[Ca^{2+}]_o$ P = 0.04 and P = 0.004 for $P_{1,parabola}$ and $P_{1,binomial}$, respectively; paired t-test; middle). The peak amplitudes for the first single events and train events are not significantly different between 3 mM $[Ca^{2+}]_o$ and 2 mM $[Ca^{2+}]_o$ (after correction for amplitude occlusion from previous events; circles: individual experiments; P = 0.17 and P = 0.61 for the first and train events, respectively; paired t-test n = 9; right). Error bars show SD. Results from the same cells are linked together with lines. (E) The variance-mean plots of the number (filled circles) and cumulative number (open squares) of released vesicles for a group of 9 experiments. When averaging, I scaled individual data to N = 2, because the mean and variance values were proportional to N values. The variance points for the cumulative number depart from the parabola to approach a line with a slope of 0.48. The line fitting the last 4 points crossed the parabola at a point where the mean value is 1.62, indicating that the estimated initial occupancies at the docking sites are 0.81 (N = 2). A simulated variance-mean plot of cumulative number is shown in pink (δ: 0.7, p:0.65, r: 0.25, s:0.15; same plot as in Fig. 19). A simulation result of 3 mM $[Ca^{2+}]_o$ data from the same experiments is shown in Figure 19. (F) The "line-parabola intersection" approach provided δ and p values. Both δ and p are significantly smaller in 2 mM $[Ca^{2+}]_o$ condition P = 0.022 and 0.017 for δ and p, respectively; paired t-test, n = 9; circles: individual experiments). Error bars show SD. Results from same cells are linked together with lines.

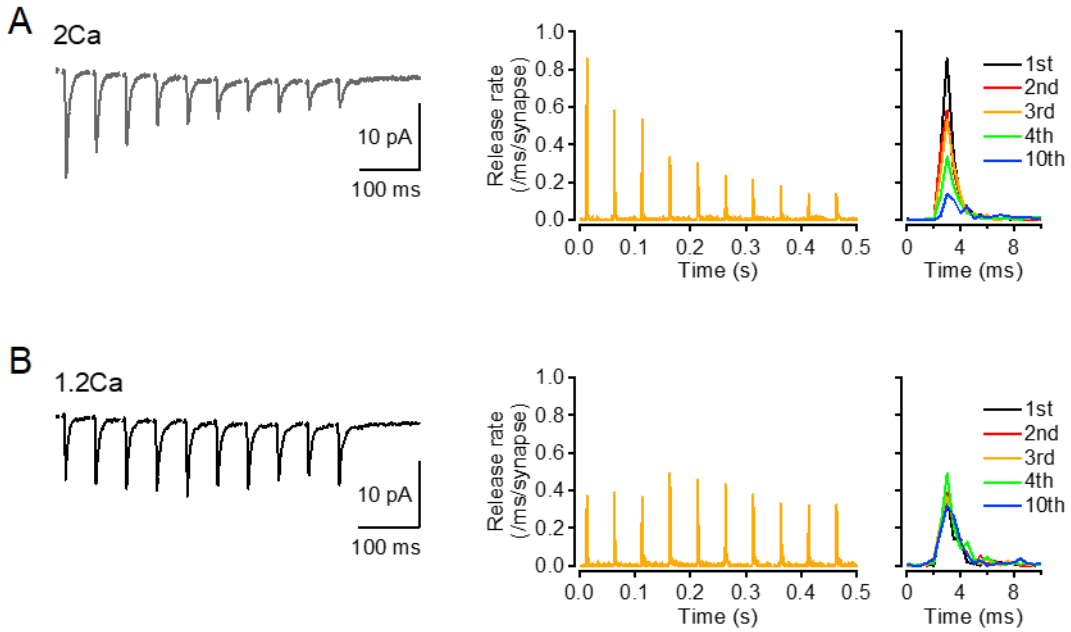

Figure 18 Average EPSCs and release rates of SVs recorded in 2 mM and 1.2 mM $[Ca^{2+}]_o$ conditions.

(A) Left, an average response to 20 Hz trains at single hMF-SLIN synapses recorded in 2 mM $[Ca^{2+}]_o$ condition (n = 9). Middle, an average release rate per synapse was calculated from the latency of the detected events (n = 9). Right, release rates for the 1st, 2nd, 3rd, 4th and 10th responses are superimposed. Time of 0 ms

shows the time of individual stimulations. (B) Left, an average response to 20 Hz trains at single hMF-SLIN synapses recorded in 1.2 mM $[Ca^{2+}]_o$ condition (n = 8). Middle, an average release rate per synapse was calculated from the latency of the detected events (n = 8). Right, release rates for the 1st, 2nd, 3rd, 4th and 10th responses are superimposed. Time of 0 ms shows the time of individual stimulations.

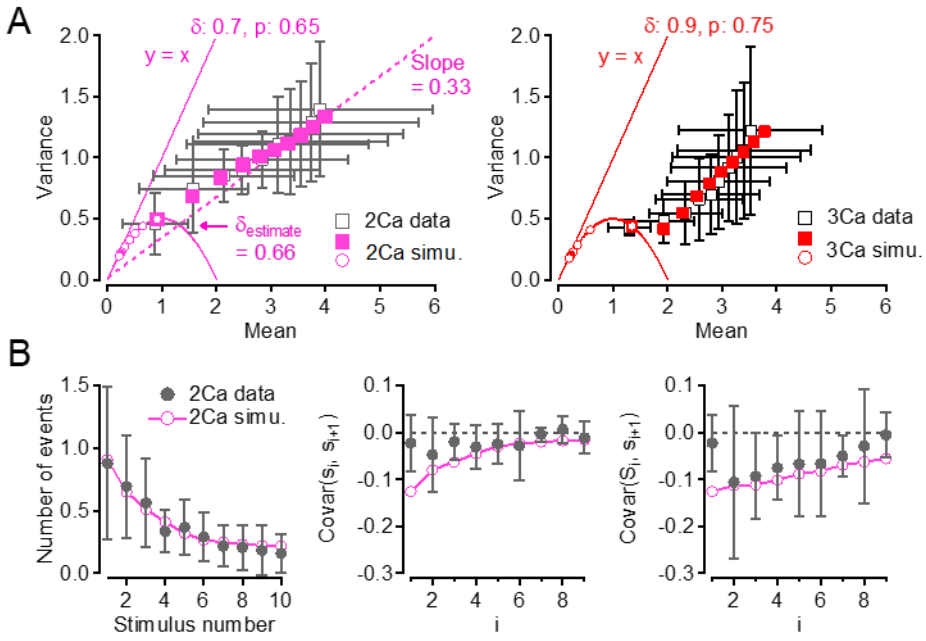

Figure 19 Stochastic properties of the cumulative number of vesicular events obtained in 2 mM $[Ca^{2+}]_o$ condition.

(A) Least-squares fits of the cumulative plots for 2 mM $[Ca^{2+}]_o$ (left; open squares; same plot as in Figure 17; n = 9) and 3 mM $[Ca^{2+}]_o$ data (right; open squares; n = 9) with two-step model provided the best combinations of parameter values (δ: 0.7, p: 0.65, r: 0.25, s: 0.15 and N: 2 for 2 mM; δ: 0.9, p: 0.75, r: 0.15, s: 0.2 and N: 2 for 3 mM). The simulated variance-mean plots of the number (open circles) and cumulative number (filled squares) of released vesicles are shown in pink and red for 2 mM and 3 mM, respectively. In the simulation for both $[Ca^{2+}]_o$, I assumed that p increased by 0.1 with stimulus number until reaching the maximum value, 1. Once reaching 1, p kept the value until the last stimuli. The variance points for the cumulative number approaches to a line with a slope of 0.33. The lines crossed the parabolas at points where the mean values are 1.32, indicating that the estimated the initial occupancy at the docking sites are 0.66. (B) The number of events, covariance calculated between consecutive counts (s_i, s_{i+1}), and covariance between the cumulative count S_i and the count s_{i+1} (i: stimulus number) from 2 mM $[Ca^{2+}]_o$ data and the model simulation with same values of parameters as those in A are plotted. All experimental data were normalized to N = 2 to compare the absolute values with those from the model simulations. Error bars show SD.

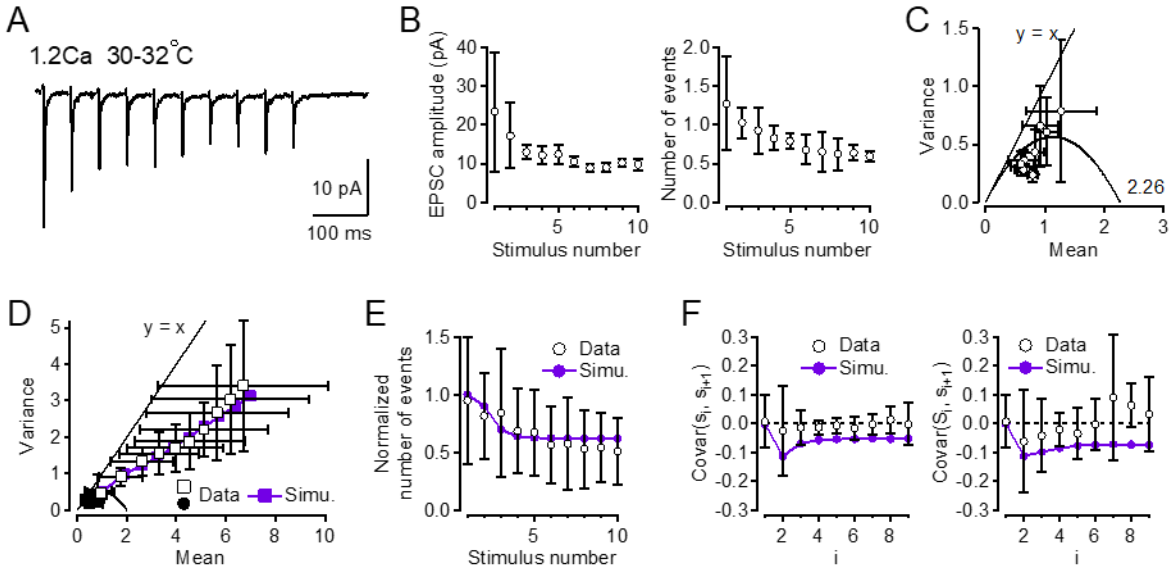

Figure 20 Estimating synaptic parameters under near physiological condition.

(A) An average response to 20 Hz trains at single hMF-SLIN synapses recorded in 1.2 mM $[Ca^{2+}]_o$ and 30-32°C condition (n = 3). (B) Plots of the peak EPSC amplitude (left) and the number of events which occur within 10 ms after individual stimulations as a function of stimulus number (n = 3). (C) The variance-mean plot of the number of released vesicles for each stimulus number and parabolic fits with y = x reference lines, provided numbers N = 2.26 of releasing units for the average data in 1.2 mM $[Ca^{2+}]_o$ and 30-32°C condition (n = 3). (D) The variance-mean plots of the number (filled circles) and cumulative number (open squares) of released vesicles for a group of 3 experiments. When averaging, I scaled individual data to N = 2, because the mean and variance values were proportional to N values. A simulated variance-mean plot of cumulative number is shown in purple (δ: 0.5, p: 1, r: 0.45, s: 0.5, N: 2). (E and F) The number of events, covariance calculated between consecutive counts (s_i, s_{i+1}), and covariance between the cumulative count S_i and the count s_{i+1} (i: stimulus number) from data and the model simulation with same values of parameters as those in D are plotted. The experimental data were normalized to N = 2 to compare the absolute values with those from the model simulations. Error bars show SD. In the condition, I obtained δ of 0.5 and p of 1 by the model simulation. Thus P_1 value, a product of δ and p, was 0.5, that is comparable to that (= 0.49) in 2 mM $[Ca^{2+}]_o$ and room temperature condition.

3.3.10 Small effect of desensitization on short-term synaptic plasticity under decreased $[Ca^{2+}]_o$ condition

The result that the synaptic parameters were different at physiological conditions from those obtained

at the higher $[Ca^{2+}]_o$ prompted me to re-evaluate the postsynaptic parameter Q and other presynaptic parameters. At the hMF-SLIN synapses, the contribution of the reduction in quantal size due to desensitization to synaptic depression was less than that at the other synapses (Otis *et al.*, 1996; Rozov *et al.*, 2001; Taschenberger *et al.*, 2005; Saviane & Silver, 2006), because the reduction somehow counterbalanced with the amplitude reduction by amplitude occlusion that often occurred at the first response due to multivesicular release under high release probability condition (Figs. 9 and 11). Therefore, one would expect that the contribution of desensitization may be observed in lower $[Ca^{2+}]_o$ condition due to a reduced effect of amplitude occlusion. Therefore, I next investigated the contributions of desensitization to the extent of synaptic plasticity by further reducing $[Ca^{2+}]_o$ to 1.2 mM.

In this $[Ca^{2+}]_o$ condition, I observed less multivesicular events (Fig. 21A). The plots of EPSC amplitude and the number of events as a function of stimulus number demonstrated almost constant responses rather than depression during trains (PPR: 1.14 ± 0.22 and 1.13 ± 0.16; s_5/s_1: 1.14 ± 0.20 and 1.22 ± 0.23 for EPSC amplitude and event number, respectively; n = 8; Fig. 21B and Fig. 18B). To see the effect of Q, I compared normalized EPSC amplitude and event number, because EPSC amplitude and event number represented N P Q and N P, respectively. In the plot, I found a slight but significant reduction of the normalized EPSC amplitudes later in a train compared with the normalized event number (Fig. 21B; *P*= 0.015, 0.031, 0.003, 0.021, and 0.002 for the 6^{th}, 7^{th}, 8^{th}, 9^{th}

and 10th responses, respectively; paired *t*-test, n = 8), indicating that an effect of Q emerged in the condition. Blockage of desensitization by cyclothiazide did not affect vesicle counts, indicating that vesicular events could be appropriately detected by the method even when quantal size was reduced due to desensitization (Fig. 22). An average of 20% difference between the normalized amplitude and event number later in a train (Fig. 21B) was consistent with a significant reduction in quantal size (22.3 ± 5.1and 19.6 ± 5.1 pA for quantal size in first and train responses, respectively; *P*= 0.0004, paired *t*-test, n = 8), suggesting that the contribution of a decrease in quantal size to the extent of plasticity could be observed in 1.2 mM $[Ca^{2+}]_o$ condition although it was small.

I next investigated other presynaptic parameters in the condition. When comparing the steady-state number of events between 1.2 mM and 3 mM $[Ca^{2+}]_o$ conditions in the same cells, I found no significant difference (event number at the 10th response; 0.42 ± 0.16 and 0.42 ± 0.15 for 1.2 mM and 3 mM $[Ca^{2+}]_o$, respectively; n = 4), suggesting no change of recruitment rate with $[Ca^{2+}]_o$. Group analysis of N values obtained from variance-mean plots of the event number showed no significant difference between 1.2 mM $[Ca^{2+}]_o$ and the other $[Ca^{2+}]_o$ conditions (Mean ± SD: 2.69 ± 1.15 for 1.2 mM $[Ca^{2+}]_o$ condition; *P* = 0.87, one-way ANOVA; Fig. 21C). In the condition, the 'line-parabola intersection' approach could not be applied because the parameter values did not meet the criteria where δ and p are relatively high and r is low (≤ 0.3). Nevertheless the other approach, that is a least-squares fit of cumulative plot with the two-step model, provided δ of 0.3 and p of 0.45 for 1.2 mM

$[Ca^{2+}]_o$ condition (Fig. 21D and Fig. 23). Both δ and p values were smaller than those in the higher $[Ca^{2+}]_o$ condition, suggesting that the constant response rather than depression was, in large part, caused by the further decrease in initial δ and p in the 1.2 mM $[Ca^{2+}]_o$ condition.

In conclusion, under lower $[Ca^{2+}]_o$ condition, Q may contributes to synaptic responses during a stimulus train, though contribution is relatively small. Rather changes in δ are more critical.

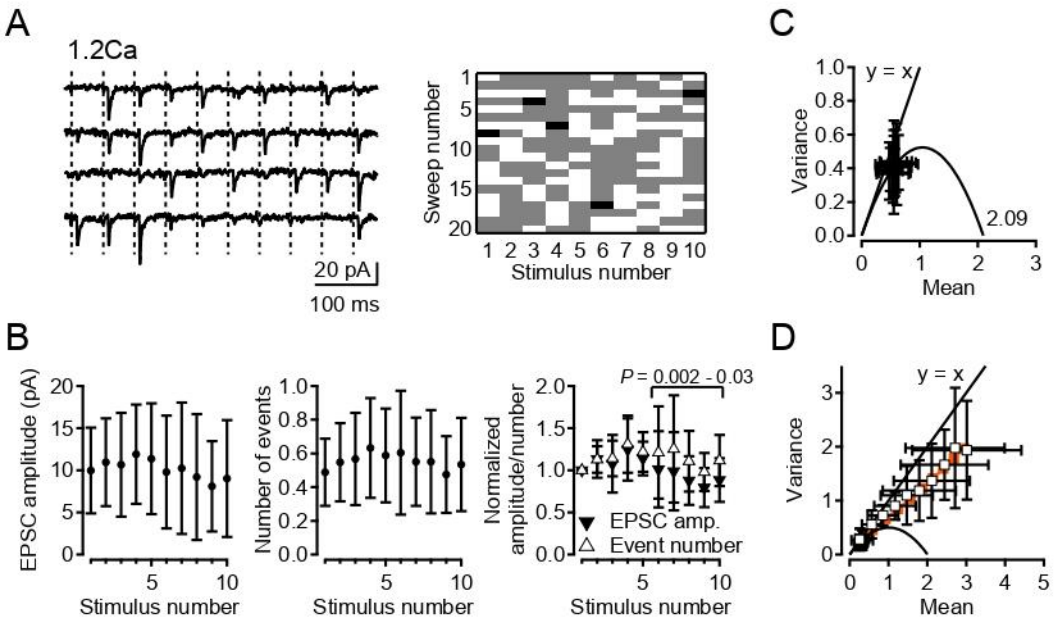

Figure 21 Estimating synaptic parameters in 1.2 mM $[Ca^{2+}]_o$ condition.

(A) Representative recording from a single hMF-SLIN synapse in 1.2 mM $[Ca^{2+}]_o$ condition. Individual EPSC responses to presynaptic action potential stimuli (20 Hz; dashed lines) are shown (left). An example of matrix of vesicular release counts as a function of stimulus number (columns) and trial number (rows) in a single synapse experiment (right). Black, gray, and white colors show 2, 1, and 0 events, respectively. (B) Peak EPSC amplitude (left) and the number of events (middle) which occur within 10 ms after individual stimulations are plotted as a function of stimulus number (n = 8). Plots of the normalized EPSC amplitude (filled inverted triangles) and the normalized event number (open triangles) as a function of stimulus number (right, n = 8). There were significant differences between the values at the 6^{th}-10^{th}responses (P = 0.015, 0.031, 0.003, 0.021, and 0.002 for the 6^{th}, 7^{th}, 8^{th},9^{th} and 10^{th} responses; paired t-test). (C) The variance-mean plots of the number of released vesicles for each stimulus number and parabolic fits with y = x reference lines, provided numbers N = 2.09 for the average data in 1.2 mM $[Ca^{2+}]_o$ condition (n = 8).(D) The variance-mean plots of the number (filled circles) and cumulative number (open squares) of released vesicles for a group of 4 experiments.

When averaging, I scaled individual data to N = 2. Simulated variance-mean plots of cumulative number of released vesicles for 1.2 mM $[Ca^{2+}]_o$ are shown in orange (δ: 0.3, p: 0.45, r: 0.15, s: 0.55; Same plots as in Fig. 23).A simulation result of 3 mM $[Ca^{2+}]_o$ data from the same experiments is shown in Figure 23. Error bars show SD.

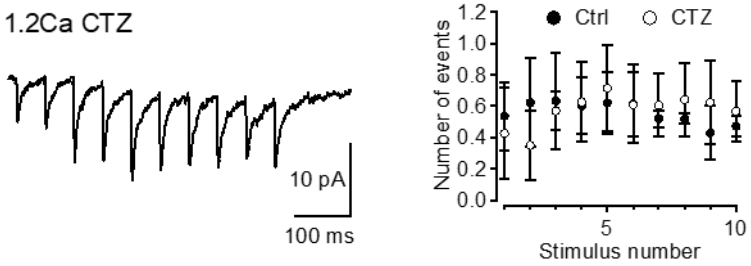

Figure 22 Vesicular event detection from EPSCs recorded in the presence of cyclothiazide.

Left, Blockade of AMPA receptor desensitization by cyclothiazide (CTZ, 50 μM) slowed the decay kinetics of EPSCs. Right, Plots for the number of detected events by matched-filtering method using EPSCs recorded in the presence and absence of CTZ as a function of stimulus number. There were no significant differences between control and CTZ (n = 3; paired *t*-test). Error bars show SD.

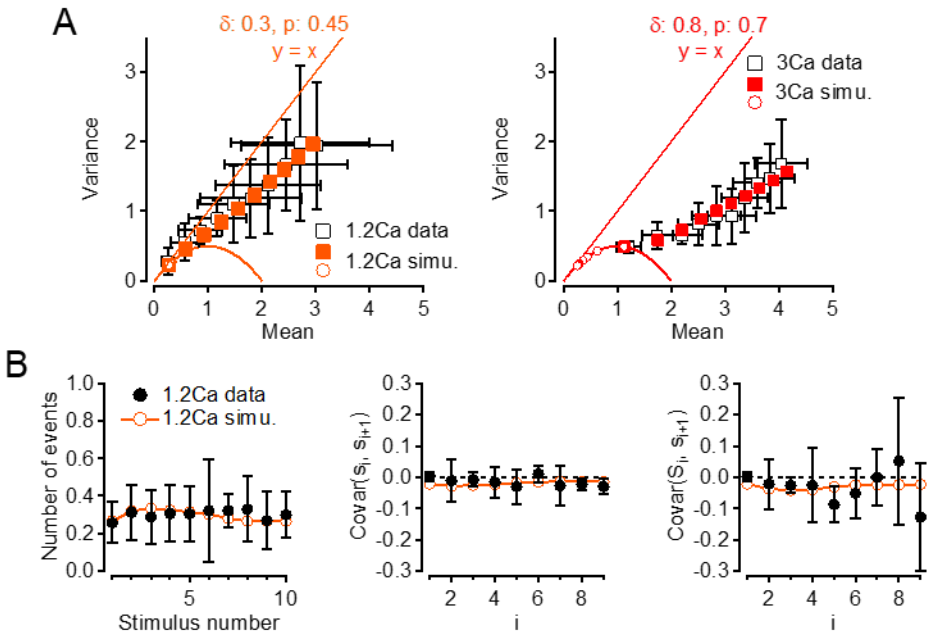

Figure 23 Stochastic properties of the cumulative number of vesicular events obtained in 1.2 mM $[Ca^{2+}]_o$ condition.

(A) Least-squares fits of the cumulative plots for 1.2 mM (left; open squares; same plot for 1.2 mM as in

Figure 21; n = 4) and 3 mM $[Ca^{2+}]_o$ data (right; open squares; n = 4) with two-step model provided the best combinations of parameter values (δ: 0.3, p: 0.45, r: 0.15, s: 0.55 and N: 2 for 1.2 mM; δ: 0.8, p: 0.7, r: 0.2, s: 0.25 and N: 2 for 3 mM). The simulated variance-mean plots of the number (open circles) and cumulative number (filled squares) of released vesicles are shown in orange and red for 1.2 and 3 mM $[Ca^{2+}]_o$, respectively. In the simulation for both $[Ca^{2+}]_o$, I assumed that p increased by 0.1 with stimulus number until reaching the maximum value, 1. Once reaching 1, p kept the value until the last stimuli. (B) The number of events, covariance calculated between consecutive counts (s_i, s_{i+1}), and covariance between the cumulative count S_i and the count s_{i+1} (i: stimulus number) from 1.2 mM $[Ca^{2+}]_o$ data (n = 4) and the model simulation with same values of parameters as those in A are plotted. All experimental data were normalized to N = 2 to compare the absolute values with those from the model simulations. Error bars show SD.

3.4 Discussion

To evaluate quantitative contributions of synaptic parameters to short-term depression, I applied the deconvolution analysis, previously established at cerebellar synapses, to hMF synapses in the forebrain for the first time. It was found that the docking site occupancy (δ; Fig.2) is the crucial determinant of the short-term depression during stimulus train.

More specifically, I detected individual vesicular release events from synaptic responses measured at single hMF-SLIN synapses (Figs. 7 and 9). Using the detected vesicular events, I then estimated the values of synaptic parameters, such as the docking site number (N), the release probability (P), and the quantal size (Q; Fig.2). The analysis indicated that the quantal amplitudes were reduced by two types of mechanisms during train stimulations (Figs. 9D and 11). A combination of amplitude occlusion and quantal size reduction during a train affected all responses to a similar extent, resulting in little contribution of the reduction of the quantal size (Q) to the extent of synaptic depression in 3 mM $[Ca^{2+}]_o$ condition. More specifically, the extent of the decrease in the SV event numbers (= N P) was similar to that of synaptic depression of the peak EPSC amplitudes (= N P Q; Fig. 9). The statistical analysis of SV counts furthermore demonstrated that the docking site number (N) was unchanged during trains (Fig. 12 and Fig. 16). These results suggested that the release probability (P), which was composed of the probability of the docking site occupancy (δ) and the release probability

of a docked SV (p), mainly contributed to synaptic depression. The simple stochastic properties of the cumulative number of events together with model simulations indicated that the probability of the initial site occupancy could be reliably estimated from the point of intersection between a linear fit of the cumulative plot and a parabolic fit of the standard variance-mean plot (Figs. 13 and 14). This "line-parabola intersection" method provided direct estimations of the occupancy probability ($\delta \approx 0.85$) and of the release probability of vesicles occupying docking sites ($p \approx 0.8$) under 3 mM $[Ca^{2+}]_o$ condition. Further model simulations suggested that the decrease of the release probability (P) reflected the reduction of the occupancy probability (δ) during trains (Fig. 14). Additionally, I found that δ varies with $[Ca^{2+}]_o$ ($\delta \approx 0.7$ and 0.4 for 2 mM and 1.2 mM $[Ca^{2+}]_o$, respectively) and that this variation contributes to determining the degree of depression (Figs. 17, 19, 21 and 23). Based on these results, I suggest that the extent of synaptic depression mainly depends on the change of the occupancy probability at hMF-SLIN synapses. The dynamic change of the vesicle occupancy at docking sites during neuronal activity may regulate synaptic strength and property, such as short-term synaptic plasticity at synapses in the forebrain.

3.4.1 Estimates of synaptic parameters at single hMF-SLIN synapses

In this study, I established single hMF-SLIN synapse recording by adjusting the position of the stimulation pipette and stimulation intensity in 3-4-week-old rats (Figs. 7 and 8). The evoked quantal

size (Q) in the recording was well characterized by a single Gaussian and had a CV of about 0.3 (Fig. 11), which had been also observed for single quanta fusion at the synapses which can be reliably stimulated and have little electrical attenuation (del Castillo & Katz, 1954; Li *et al.*, 2014; Malagon *et al.*, 2016). Thus, vesicular events were reliably detected by the matched-filtering method even when quantal size was reduced by postsynaptic saturation and desensitization (Figs. 9, 11 and 22). Using vesicle counts obtained at the single hMF-SLIN synapses, I estimated key basic synaptic parameters, including N (average: 2.67, range: 1-5), P (average: 0.65, 0.40 and 0.20; range: 0.37-0.90, 0.03-0.84, and 0.07-0.35 for 3 mM, 2 mM, and 1.2 mM $[Ca^{2+}]_o$, respectively), and Q (average: 23.2 pA, range: 10-43 pA) under room temperature conditions (Figs. 11, 12, 17, and 21). Under 1.2 mM $[Ca^{2+}]_o$ and 30-32°C condition, P value was comparable to that under 2 mM $[Ca^{2+}]_o$ and room temperature condition (Fig. 20). While low $[Ca^{2+}]_o$ reduces P, the simultaneous change to higher temperature can increase P, because presynaptic Ca^{2+} currents activate faster and have a larger amplitude at 30-32°C (Kushmerick *et al.*, 2006). The overall effect may thus be to keep P the same as under 2 mM $[Ca^{2+}]_o$ and room temperature condition. N values that were previously obtained by variance-mean analysis of the peak amplitudes of EPSCs, ranged from 1 to 2 in 2-week-old rats (Lawrence *et al*. 2004). The P values were reported to range from 0.34 to 0.51 under 2.5 mM $[Ca^{2+}]_o$ condition and from 0.44 to 0.78 under 3.8 mM $[Ca^{2+}]_o$ condition, while the Q values ranged from 12 to 70 pA (average: 28.8 pA; Lawrence *et al*. 2004). These results indicate that comparable values

were obtained by variance-mean analysis using either peak EPSC amplitudes or SV counts, and that the hMF-SLIN synapses have not necessarily a single docking site, and often have multiple docking sites in 2-4-week-old rats.

By fitting the probability distribution of SV counts for the first and second responses with a binomial model, I revealed that N did not change between the first and second at hMF-SLIN synapses under high $[Ca^{2+}]_o$ condition (Fig. 12). The simulation results were consistent with unchanged N during trains in the condition (Fig. 14 and 16). Additionally, I estimated similar N values among different $[Ca^{2+}]_o$ conditions, indicating that N value was not sensitive to $[Ca^{2+}]_o$ (Figs. 17 and 20). Under low release probability condition, accurate estimation of N values could not be achieved (Clements & Silver, 2000). Therefore, there is still a possibility that N changes during trains under low $[Ca^{2+}]_o$ condition. When estimating N with less accuracy by binomial fits under 1.2 mM $[Ca^{2+}]_o$ condition, I obtained similar N values from the first and fourth responses having maximal EPSC amplitude and event number in the condition (Mean ± SD: 2.88 ± 2.10 and 3.38 ± 3.16 for the first and fourth, respectively; $P = 0.75$, paired *t*-test). The result suggested that N is unchanged during trains under low $[Ca^{2+}]_o$ condition, although I could not perfectly exclude the possibility of a change in N during trains.

Only in a few preparations the probability of the site occupancy (δ) has been estimated by maximizing p under extreme recording condition or by presynaptic spot Ca^{2+} uncaging, because of

the difficulty of separating δ from the release probability of a docked SV, p (Trigo *et al.*, 2012; Malagon *et al.*, 2020). Here, I developed another approach, the "line-parabola intersection" approach, to directly estimate the values for δ and p separately (Figs. 13 and 14). Reliable estimates can be obtained with our new approach when δ and p are high and the rate of SV recruitment to docking sites is low. Therefore, this new approach is more applicable to depressing synapses. In this study, the approach could be applied to 2 mM and 3 mM $[Ca^{2+}]_o$ data. By combining the new approach with variance-mean analysis of SV counts, I could obtain all synaptic parameter values simultaneously from experimental data at depressing synapses (Figs. 14 and 17).

The probability of docking site occupancy is dependent on $[Ca^{2+}]_o$ (Malagon *et al.*, 2020). In cerebellar PF-MLI synapses (an example of mildly facilitating glutamatergic synapses), the values for the occupancy are 0.22 and 0.47 with 1.5 mM and 3 mM $[Ca^{2+}]_o$, respectively. In our experiments using hMF-SLIN synapses, I estimated δ of 0.4, 0.7, and 0.85 for 1.2 mM, 2 mM, and 3 mM $[Ca^{2+}]_o$, indicating that the δ value was higher than that in PF-MLI synapses (Figs. 14, 17 and 21). In MLI-MLI synapses, which are depressing GABAergic synapses, the δ value is 0.5-0.7 in 2 mM $[Ca^{2+}]_o$ condition (Trigo *et al.*, 2012; Pulido *et al.*, 2015). These results suggest that the site occupancy is similar between glutamatergic and GABAergic depressing synapses.

3.4.2 Synaptic plasticity at single hMF-SLIN synapses

So far, several mechanisms for synaptic depression via changes in synaptic parameters have been reported (Schneggenburger *et al.*, 2002; Zucker & Regehr, 2002). Depletion of release-competent vesicles, desensitization and/or saturation of postsynaptic receptors, decrease in the presynaptic calcium current, silencing and/or availability of the release sites are involved in the mechanism of depression (Trussell *et al.*, 1993; Otis *et al.*, 1996; Silver *et al.*, 1998; Forsythe *et al.*, 1998; Taschenberger & Gersdorff, 2000; Brenowitz & Trussell, 2001; Chen *et al.*, 2002; Foster & Regehr, 2004; Xu & Wu, 2005; Taschenberger *et al.*, 2005; Saviane & Silver, 2006; Doussau *et al.*, 2010; Hua *et al.*, 2013).

The present study suggests that the decrease of the occupancy probability (δ) during trains results in a reduction of the release probability (P)/the number of released vesicles, leading to short-term depression at hMF-SLIN synapses (Figs. 9, 12 and 14). In hMF-SLIN synapses, pre- and postsynaptic modulations of synaptic transmission have been reported (Evstratova & Tóth, 2014). Presynaptic mGluRs and kainate autoreceptors are activated during repetitive stimulation, leading to modulation of the synaptic strength (Tóth *et al.*, 2000; Scott *et al.*, 2008; Cosgrove *et al.*, 2011*b*). However, the effects at hMF-SLIN synapses are less pronounced than those at hMF-CA3 pyramidal cell synapses (Tóth *et al.*, 2000; Scott *et al.*, 2008). Voltage-dependent polyamine blockade of AMPA receptors, and NMDA receptor activation during repetitive stimulation also influences short-term plasticity at

hMF-SLIN synapses (Tóth *et al.*, 2000; Lei & McBain, 2002). However, because I suppressed the release of polyamine from channel pores by holding membrane potential at -60 mV, and blocked NMDA receptor currents by D-APV, those effects were likely negligible. Additionally, the decrease in the quantal size (Q) during a train due to desensitization and saturation of AMPA receptors was counterbalanced among responses under high release probability condition (Figs. 9 and 11). Furthermore, N was unchanged during trains of stimuli (Fig. 12 and Fig. 16), while a release probability of a docked SV (p) was likely constant or increased during trains at the mature hMF-SLIN synapses that I used in this study (Fig. 14). In mature calyx of Held synapses, the presynaptic AP-like Ca^{2+} current does not decrease during a train and exhibits rather facilitation in the beginning of an AP train at 100 Hz (Taschenberger *et al.*, 2002). The same is true for mature hair cells synapses (Li *et al*. 2014). Thus, the mature hMF-SLIN synapses probably do not exhibit presynaptic Ca^{2+} current inactivation during AP train stimulation, suggesting no reduction in p. Therefore, the synaptic depression mainly reflects a decrease of the occupancy probability (δ) in our experiments, especially under high release probability conditions. Under low $[Ca^{2+}]_o$ conditions (Figs. 17 and 21), the decrease in initial δ with $[Ca^{2+}]_o$ reduced the number of released SV and peak EPSC amplitude at the first response in trains, leading to affect the extent of synaptic plasticity at hMF-SLIN synapses. Under 1.2 mM $[Ca^{2+}]_o$ condition, the effect of desensitization emerged later in a train because of less saturation (Fig. 21). It is again likely that N is constant while p is increased/constant during trains in

the conditions (Figs. 17 and 21; see Discussion above). Therefore, decrease in δ and/or Q could contribute to synaptic depression under low $[Ca^{2+}]_o$ conditions at the synapses.

At glutamatergic facilitating synapses between cerebellar PFs and MLIs, the initial low probability of the site occupancy (δ) at rest allows rapid replenishment of SVs to empty docking sites after the first AP, increasing δ during a time period from the first to the second AP. This causes augmentation of the second response, leading to synaptic facilitation (Miki *et al.*, 2016; Malagon *et al.*, 2020). This result indicates a strong influence of the occupancy probability (δ) on synaptic facilitation. In contrast, in hippocampal synapses replenishment is slow while initial δ is high, leading to a decrease in δ and hence to synaptic depression. Therefore, combinations of initial δ and replenishment rate determine δ during trains, and in turn shape short-term synaptic plasticity. Altogether, these results suggest that the occupancy probability may be a crucial determinant of various forms of short-term synaptic plasticity at some glutamatergic synapses under certain conditions.

hMF terminals strongly express synaptotagmin-7, which is known as a calcium sensor for synaptic facilitation at several synapses including hMF-CA3 synapses (Jackman *et al.*, 2016). However, we have not observed clear facilitation in any conditions at the hMF-SLIN synapses that I selected as depressing synapses (Figs. 9, 17, and 21). There are two possible explanations for the contradiction: (i) synaptotagmin-7 proteins are not located at some small en passant or filopodial extensions of the hMF boutons that terminate on SLINs, but are located at hMF synapses on CA3 pyramidal cells. (ii)

synaptotagmin-7 is a sensor for SV recruitment and/or asynchronous release, not for synaptic facilitation (Bacaj *et al.*, 2013; Liu *et al.*, 2014). To clarify the reason, further studies would be needed at the depressing synapses.

3.4.3 Estimate of the pool size

One of the most widespread mechanisms underlying short-term depression is depletion of the RRP (Schneggenburger *et al.*, 2002; von Gersdorff & Borst, 2002; Zucker & Regehr, 2002). The RRP size (= N δ) as well as the magnitude of depression are determined by the balance between vesicle consumption and simultaneous recruitment of new vesicles at presynaptic terminals during trains of APs (Wang & Kaczmarek, 1998; Dittman & Regehr, 1998; Wu & Borst, 1999). Changes in synaptic signaling, via myosin light chain kinase (MLCK) activation and/or cAMP pathways, can alter the short-term dynamics of synapses via changes in RRP size (Srinivasan *et al.*, 2008; González-Forero *et al.*, 2012). Change in the propensity of multivesicular release via RRP size change and not just via Pr change also affected synaptic plasticity (Vaden *et al.*, 2019). However, quantitative description of the change in RRP size during trains has been lacking at the synapses in the forebrain. Here, I obtained estimates for the docking site number (N = 2.7) per AZ and for the initial docking site occupancy (δ ≈ 0.85) at hMF-SLIN synapses under 3 mM $[Ca^{2+}]_o$ condition (Figs. 13 and 14). According to these estimates, the number of vesicles at docking sites per AZ is calculated to be ~2.3 by multiplying N

and δ. At 3 mM calcium and room temperature, the recruitment rate is calculated to be 3.25 s^{-1} per docking site by the simulation results, indicating that at most ~0.17 vesicles per docking site can be recruited during an inter-spike interval (50 ms) if the site is empty. Because of high p value (≈ 0.8), 99% of the initially docked vesicles are released by the first three stimuli in a train. Thereafter, the slowly recruited vesicles determine steady-state release (~0.25 vesicles per AZ per stimulus). The analysis of SV counts and model simulation suggested that N was unchanged during trains under high release probability condition (Figs. 12, 14 and 16). Thus, the RRP depletion known as a mechanism of synaptic depression represents depletion of the number of vesicles occupying docking sites, or in other words a decrease of the occupancy probability (δ) during trains (Taschenberger *et al.*, 2005; Vaden *et al.*, 2019).

By pre- and post-synaptic paired recording at hMF-CA3 pyramidal cells, a RRP size of 2 per AZ was also obtained under 2 mM $[Ca^{2+}]_o$ condition (Vyleta & Jonas, 2014). I estimated a RRP size of ~1.8 for 2 mM $[Ca^{2+}]_o$ at a single hMF-SLIN synapse. These results suggest non-target specific RRP size per AZ at hMF terminals. Measurement of membrane capacitance increases in response to depolarization pulses at hMF terminals demonstrated larger RRP size (~30 vesicles per AZ; Hallermann et al., 2003; Miyano et al., 2019). This is probably because the recruited vesicles during the depolarization participated in the vesicle release (Delvendahl & Hallermann, 2016). The pool size

obtained by the capacitance measurement may correspond to the total pool size including the replacement pool and the recycling pool in the two-step model.

3.4.4 SV recruitment at docking sites

The extent of short-term synaptic depression depends on the RRP size (= N δ) and the recruitment rate to the RRP (Zucker & Regehr, 2002). The δ values at the time of each stimulus are determined by the remaining δ value after previous stimulus and amount of SV recruitment at a docking site during a time of an interspike interval. Therefore, the probability of SV recruitment during an inter-AP time interval (r) and release probability of a docked SV (p) are crucial factors of determining δ. If r is fast, δ would hover at almost maximum value during trains, leading to large contribution of p to synaptic plasticity (Fig. 15). The simulation results showed r = 0.15, 0.3, and 0.4 for 3 mM, 2 mM, and 1.2 mM $[Ca^{2+}]_o$ conditions, respectively (Figs. 14, 17, 19, 21 and 23), indicating an apparent increase in r with a decrease in $[Ca^{2+}]_o$. That is probably because I have not assumed that p increases with stimulus number in the simulation. Under high p condition, p is probably near maximal at the stimulation onset (> 0.8 under 3 mM $[Ca^{2+}]_o$ condition), and can be assumed to be stable or slightly increased (Fig. 14). However, it is not the case for lower $[Ca^{2+}]_o$ condition, because p is << 1. When assuming that p increases by 0.2 with each stimulus during a train for 2 mM and 1.2 mM $[Ca^{2+}]_o$, r values for both conditions become ~0.2, similar to that for 3 mM $[Ca^{2+}]_o$. Therefore, it is likely that

the recruitment rates at the hMF-SLIN synapses are similar among different $[Ca^{2+}]_o$ conditions. The result is consistent with Ca^{2+}–independent recruitment to the RRP at hMF terminals (Miyano *et al.*, 2019). Vesicle mobilization or recruitment can be greatly influenced by temperature under conditions of fixed external Ca^{2+} (Kushmerick *et al.*, 2006). Overall levels of short-term depression are thus generally reduced at more physiological temperatures.

3.4.5 Desensitization of AMPA receptors

Desensitization decreases Q, supposed to cause synaptic depression (Jones & Westbrook, 1996). At PF-MLI synapses, amplitude occlusion primarily reflects receptor activation, because the small difference between the time constant of recovery of amplitude occlusion (1.1 ms) and that of mEPSC decay (0.67 ms), suggests that receptor availability follows a direct recovery path via occupied closed state toward the resting state (Malagon *et al.*, 2016). In hMF-SLIN synapses, the recovery time constant of amplitude occlusion was one-order of magnitude larger (11.1 ms) with a mEPSC decay time constant of 4.7 ms (Figs. 7 and 9D). AMPA receptors recover from desensitized states to resting state within a time period of ~10 ms, while they recover from activated states with short durations of ~1ms (Robert & Howe, 2003). Therefore, the amplitude occlusion at hMF-SLIN synapses may reflect receptor desensitization, rather than activation.

The percentage of the amplitude occlusion (ω) of 0.18 at the hMF-SLIN synapse is smaller than

the ω values of 0.5-0.7 at the PF-MLI synapse, the calyx of Held synapse, and the cerebellar mossy fiber-granule cell synapse (Fig.9D; Ishikawa et al., 2002; DiGregorio et al., 2007; Malagon et al., 2016). In addition, the degree of reduction of EPSC amplitudes by cumulative desensitization at hMF-SLIN synapses is around 20% which is slightly larger than the value of 10% obtained at PF-MLI synapses (Fig. 11; Malagon et al., 2016). These differences probably result from a variety of synapse specific features, such as the sizes of AZ and postsynaptic density, glial coverage of synapses, the distribution and density of AMPA receptors, the subtypes of AMPA receptors, and/or the presence of the auxiliary proteins TARPs (Tóth & McBain, 1998; Koike *et al.*, 2000; Robert & Howe, 2003; Greger *et al.*, 2007; Rollenhagen *et al.*, 2007; Wilke *et al.*, 2013).

3.4.6 Molecular determinants of docking site occupancy

Molecular determinants of the site occupancy (δ) remain unknown in detail. However recent studies about docking sites and SV movements in AZs have provided a clue to understand the docking site occupancy (δ) from physical and molecular points of view. Recent studies demonstrated that docking site numbers (N) matched with the numbers of supramolecular assemblies, such as Ca^{2+} channel, Munc13, and RIM nanoclusters (Tang *et al.*, 2016; Miki *et al.*, 2017; Pulido & Marty, 2017; Sakamoto *et al.*, 2018), suggesting that the molecular nano-assemblies defined the regions for the docking sites. Nanometer-resolution vesicle observations revealed that repetitive vesicle fusions occurred at limited

regions in an AZ during neuronal activity (Maschi & Klyachko, 2017). Super-resolution imaging and electron microscopy revealed that SV movement was dynamic within <100 nm AZ, supporting the idea of incomplete occupancy ($\delta < 1$; Midorikawa & Sakaba, 2015, 2017; Chang et al., 2018; Kusick et al., 2020; Miki et al., 202). These results suggest that molecular nano-assemblies with SVs may represent docking sites occupied by SVs (= N δ) which are ready to release in response to an AP. In this study, I found an increase of δ with $[Ca^{2+}]_o$ at hMF-SLIN synapses. Similar finding has been recently reported at cerebellar PF-MLI synapses (Malagon *et al.*, 2020), suggesting that the Ca^{2+}-dependent change of δ is a common feature of the site occupancy among synapses. The Ca^{2+} dependency of δ may be mediated by several AZ molecules associated with the nano-assemblies including synaptotagmin-1 and Munc13 that are commonly expressed among synapses (Junge *et al.*, 2004; Shin *et al.*, 2010; Chang *et al.*, 2018).

In summary, the present study suggests that the probability of docking site occupancy (δ) is crucial for short-term synaptic plasticity (Fig.2). Other factors, such as N, p and Q are relatively constant during stimulus train and /or contribute little to short-term plasticity. The importance of δ on synaptic plasticity has been demonstrated at cerebellar synapses showing facilitation, but this study is the first demonstration at forebrain synapses as well as depressing synapses. Future studies integrating nanometer-scale observations and in-depth electrophysiological examinations would provide physical insight into a molecular determinant of the docking site occupancy (δ), leading to understand

the molecular mechanisms of synaptic plasticity and short-term memory.

Chapter 4. General Discussion

hMFs innervate pyramidal cells and the interneurons, and the interneurons in turn innervate the pyramidal cells to form a feed-forward circuit. hMF synapses undergo both structural and functional plasticity (from short-term facilitation/depression to LTP/LTD), which control the network activity (Shigemoto *et al.*, 1997; Acsády *et al.*, 1998; Pelkey *et al.*, 2005). In this study, I focused on two types of plasticity, modulation by metabotropic glutamate receptors (Chapter 2) and activity-dependent synaptic depression (Chapter 3). In the first part, I recorded directly from the hMF presynaptic terminals and found that activation of group III metabotropic glutamate receptors (mGluR) suppressed synaptic vesicle release by decreasing Ca^{2+} influx (Chapter 2.3). In the second part of the study, the values of δ and p were estimated at hMF-SLIN synapses using new variance-mean analysis (Chapter 3.3). These parameters cannot be obtained by conventional variance-mean analysis, which estimates N, P, and Q. Furthermore, the model simulations suggested that short-term plasticity is mainly controlled by changes in δ (Chapter 3.3.7 and 3.3.8). The values of δ and p were previously estimated by the model-based approach, but in this study the value of δ and p were obtained directly from the data, which are valid when δ and p are large and vesicle recovery is slow (Chapter 3.3.7).

4.1 The effect of group III mGluRs on the docking site occupancy (δ) at hMF-

pyramidal cell synapses

I found reduction of Ca^{2+} influx by activation of Group III mGluRs at hMF presynaptic terminals (Chapter 2.3). I suggest that reducing Ca^{2+} influx is an effect of mGluR4 and 8 activations because mGluR7 is expressed only slightly at the hMF terminal (Chapter 2.4.2 and Shigemoto et al., 1997). mGluR4/8-mediated suppression of glutamate release from the hMF boutons results in delayed action potential initiation at 20 and 40 Hz stimuli (Cosgrove *et al.*, 2011*b*). I suggest that activation of group III mGluRs may also prevent epileptic-like firings during high-frequency inputs at hMF-pyramidal synapses by auto-receptor activation (see Chapter 2.4.2). I should note that because recording from hMF terminals mainly reflects presynaptic physiology of large hMF terminals which have dozens of active zones and innervate the pyramidal cell (Chicurel & Harris, 1992; Henze *et al.*, 2000), contribution of filopodial extensions to interneuron, which usually form a small synapse with one or two active zones (Acsády *et al.*, 1998), is supposed to be minor. Therefore, the results may be mainly relevant to mGluRs expression at large terminals rather than filopodial extensions.

In the present study, activation of group III mGluR decreased transmitter release for 10 ms depolarization at presynaptic terminals (Chapter 2.3) in addition to the reduction in Ca^{2+} influx in the time frame of minutes (see Chapter 2.4.1). It is likely that group III mGluR activation decreases the initial release probability (P), which in turn causes the decrease of transmitter release during the short depolarization. It is suggested that the downstream of mGluR4/8 may be cAMP/PKA-signaling

pathways, which may phosphorylate/dephosphorylate proteins in the active zone release machinery, such as RIM1α and synapsin I in the longer time course (Greengard *et al.*, 1993; Evans *et al.*, 2001; Castillo *et al.*, 2002; Leenders & Sheng, 2005). Rab3/RIM/Munc13 interaction is important for priming of synaptic vesicles for rapid transmitter release (Dulubova *et al.*, 2005), suggesting that RIM1α may be involved in the release probability of a docked synaptic vesicle (p). Activation of PKA induces LTP at cerebellar synapse by phosphorylation of RIM1α(Lonart *et al.*, 2003), and dephosphorylation may be relevant to LTD (Atwood *et al.*, 2014). Synapsin I is an important regulator of the synaptic vesicle cycle (Greengard *et al.*, 1993), indicating that Synapsin I may be involved in vesicle recruitment (r). The release probability of a docked synaptic vesicle (p) and probability of synaptic vesicle recruitment (r) are crucial factors of determining the docking site occupancy (δ). These suggest that mGluR4/8 may be crucial for δ in the long-term depression which is mediated by decreasing p or r.

4.2 The effect of group III mGluRs on the docking site occupancy (δ) at hMF-SLIN synapses

At hMF-SLIN synapses, mGluR7 is highly expressed at the presynaptic terminal (Shigemoto *et al.*, 1997) and long-term depression occurs by activation of group III mGluRs under condition of high-frequency presynaptic stimulation, likely through auto-receptor activation (Pelkey *et al.*, 2005). When

this synapse type continues to receive intense stimulation after induction of long-term depression, the synapses internalize surface-expressed mGluR7, resulting in rebound long-term potentiation (Pelkey *et al.*, 2005). SLINs innervate pyramidal cells and form a strong feed-forward inhibitory circuit (Mori *et al.*, 2004; Evstratova & Tóth, 2014). If high-frequency stimuli occur in series, pyramidal cells would easily undergo epileptiform activity when feedforward inhibition remains depressed. mGluR7 may have the role in preventing epileptiform activity in the hippocampus during high-frequency stimulation through such bi-directional plasticity (Pelkey *et al.*, 2005).

At hMF-SLIN synapses, mGluR7, expressed on the surface of presynaptic terminals or internalized from the membrane, may contribute to the induction of LTD or LTP, respectively (Pelkey *et al.*, 2005). In the condition of mGluR7 expressed on surface, the terminals are completely insensitive to elevation of cAMP. In the condition of mGluR7 internalized, the terminals are sensitive to changing in cAMP, allowing to induce AC/cAMP/PKA-mediated LTP, because mGluR7 expressed on surface may sequester RIM1α (Pelkey *et al.*, 2008). In the condition of mGluR7 internalized, AC/cAMP/PKA-mediated LTP may be induced by phosphorylation of RIM1α. Because LTP is abolished in mice lacking RIM1α at hMF-pyramidal cell synapses (Castillo *et al.*, 2002), LTP induced at hMF-SLIN and hMF-pyramidal cell may have the same mechanism. In addition, the docking site occupancy (δ) may contribute to the mGluR7-internalized LTP because the increasing in cAMP activates PKA which phosphorylates proteins such as RIM1α and synapsin I (Greengard et al., 1993; Evans et al., 2001;

Castillo et al., 2002; Leenders & Sheng, 2005; Chapter 4.1). In the present study, it was found that the parameters of synaptic strength, such as docking site occupancy (δ), can be determined quantitatively at hMF-SLIN synapses. It may be interesting to investigate the effect of δ on LTP by obtaining the parameters in the condition of LTP.

4.3 δ may contribute the plasticity at hMF synapses in the future

At hMF-pyramidal cell synapses, the decreased transmitter release may be mediated by the activation of mGluR4/8, and downregulation of PKA by mGluR4/8 may decrease the docking site occupancy (δ; Chapter 4.1) because RIM1 is phosphorylated by PKA and is important for the organization of docking site (Tang *et al.*, 2016). At hMF-SLIN synapses, short-term plasticity was mainly mediated by the change in δ (Chapter 3), and δ may also contribute to mGluR7-internalized long-term potentiation by the activation of PKA (Chapter 4.2). Furthermore, because mGluR7-internalized LTP at hMF-SLIN synapses may have the same mechanisms of AC/cAMP/PKA-mediated LTP at hMF-pyramidal cell presynaptic terminals (Castillo *et al.*, 2002; Pelkey *et al.*, 2008) and model simulation suggested that short-term plasticity is controlled by changes in δ at hMF-SLIN (Chapter 3), δ may be a key of understanding the various forms of plasticity of hMF synapses in addition to short-term plasticity. In the future, if it will be found that δ will contribute to mGluR7-internalized LTP at hMF-SLIN synapses, the method used here may be useful for studying the mechanisms of long-term

plasticity at both hMF-pyramidal and SLIN synapses.

5 Reference

Abbott LF & Regehr WG (2004). Synaptic computation. *Nature* **431,** 796–803.

Acsády L, Kamondi A, Sík A, Freund T & Buzsáki G (1998). GABAergic Cells Are the Major Postsynaptic Targets of Mossy Fibers in the Rat Hippocampus. *The Journal of Neuroscience* **18,** 3386–3403.

Alabi ARA & Tsien RW (2012). Synaptic Vesicle Pools and Dynamics. *Cold Spring Harbor Perspectives in Biology* **4,** a013680.

Amaral DG & Dent JA (1981). Development of the mossy fibers of the dentate gyrus: I. A light and electron microscopic study of the mossy fibers and their expansions. *Journal of Comparative Neurology* **195,** 51–86.

Anwyl R (1999). Metabotropic glutamate receptors: electrophysiological properties and role in plasticity. *Brain Research Reviews* **29,** 83–120.

Atwood BK, Lovinger DM & Mathur BN (2014). Presynaptic long-term depression mediated by Gi/o-coupled receptors. *Trends in Neurosciences* **37,** 663–673.

Auger C, Kondo S & Marty A (1998). Multivesicular Release at Single Functional Synaptic Sites in Cerebellar Stellate and Basket Cells. *Journal of Neuroscience* **18,** 4532–4547.

Auger C & Marty A (2000). Quantal currents at single-site central synapses. *The Journal of Physiology* **526,** 3–11.

Bacaj T, Wu D, Yang X, Morishita W, Zhou P, Xu W, Malenka RC & Südhof TC (2013). Synaptotagmin-1 and Synaptotagmin-7 Trigger Synchronous and Asynchronous Phases of Neurotransmitter Release. *Neuron* **80,** 947–959.

Bartos M, Vida I & Jonas P (2007). Synaptic mechanisms of synchronized gamma oscillations in inhibitory interneuron networks. *Nature Reviews Neuroscience* **8,** 45–56.

Blanchard K, de San Martín JZ, Marty A, Llano I & Trigo FF (2020). Differentially poised vesicles underlie fast and slow components of release at single synapses. *Journal of General Physiology* **152,** e201912523.

Bornschein G, Brachtendorf S & Schmidt H (2020). Developmental Increase of Neocortical Presynaptic Efficacy via Maturation of Vesicle Replenishment. *Frontiers in Synaptic Neuroscience* **11,** Article 36.

Borst JGG, Helmchen F & Sakmann B (1995). Pre- and postsynaptic whole-cell recordings in the medial nucleus of the trapezoid body of the rat. *The Journal of Physiology* **489,** 825–840.

Borst JGG (2010). The low synaptic release probability in vivo. *Trends in Neurosciences* **33,** 259–266.

Brenowitz S & Trussell LO (2001). Minimizing Synaptic Depression by Control of Release Probability. *Journal of Neuroscience* **21,** 1857–1867.

Cartmell J & Schoepp DD (2000). Regulation of Neurotransmitter Release by Metabotropic Glutamate Receptors. *Journal of Neurochemistry* **75,** 889–907.

Castillo PE, Schoch S, Schmitz F, Südhof TC & Malenka RC (2002). RIM1α is required for presynaptic long-term potentiation. *Nature* **415,** 327–330.

Chang S, Trimbuch T & Rosenmund C (2018). Synaptotagmin-1 drives synchronous Ca 2+ -triggered fusion by C 2 B-domain-mediated synaptic-vesicle-membrane attachment. *Nature Neuroscience* **21,** 33–42.

Charlton MP, Smith SJ, Zucker RS (1982). Role of presynaptic calcium ions and channels in synaptic facilitation and depression at the squid giant synapse. *The Journal of Physiology* **323,** 173–193.

Chen C, Blitz DM & Regehr WG (2002). Contributions of Receptor Desensitization and Saturation to Plasticity at the Retinogeniculate Synapse. *Neuron* **33,** 779–788.

Chicurel ME & Harris KM (1992). Three-dimensional analysis of the structure and composition of CA3 branched dendritic spines and their synaptic relationships with mossy fiber boutons in the rat hippocampus. *Journal of Comparative Neurology* **325,** 169–182.

Citri A & Malenka RC (2008). Synaptic plasticity: Multiple forms, functions, and mechanisms. *Neuropsychopharmacology* **33,** 18–41.

Clements JD & Silver RA (2000). Unveiling synaptic plasticity: a new graphical and analytical approach. *Trends in Neurosciences* **23,** 105–113.

Conn PJ & Pin JP (1997). Pharmacology and functions of metabotropic glutamate receptors. *Annual Review of Pharmacology and Toxicology* **37,** 205–237.

Corti C, Aldegheri L, Somogyi P & Ferraguti F (2002). Distribution and synaptic localisation of the metabotropic glutamate receptor 4 (mGluR4) in the rodent CNS. *Neuroscience* **110,** 403–420.

Cosgrove KE, Galván EJ, Barrionuevo G & Meriney SD (2011*a*). mGluRs Modulate Strength and Timing of Excitatory Transmission in Hippocampal Area CA3. *Molecular Neurobiology* **44,** 93–101.

Cosgrove KE, Meriney SD & Barrionuevo G (2011*b*). High affinity group III mGluRs regulate mossy fiber input to CA3 interneurons. *Hippocampus* **21,** 1302–1317.

Crowley JJ, Carter AG & Regehr WG (2007). Fast Vesicle Replenishment and Rapid Recovery from Desensitization at a Single Synaptic Release Site. *Journal of Neuroscience* **27,** 5448–5460.

del Castillo J & Katz B (1954). Quantal components of the end-plate potential. *The Journal of Physiology* **124,** 560–573.

Delvendahl I & Hallermann S (2016). The Cerebellar Mossy Fiber Synapse as a Model for High-Frequency Transmission in the Mammalian CNS. *Trends in Neurosciences* **39,** 722–737.

DiGregorio DA, Rothman JS, Nielsen TA & Silver RA (2007). Desensitization Properties of AMPA Receptors at the Cerebellar Mossy Fiber-Granule Cell Synapse. *Journal of Neuroscience* **27,** 8344–8357.

Dittman JS & Regehr WG (1998). Calcium Dependence and Recovery Kinetics of Presynaptic Depression at the Climbing Fiber to Purkinje Cell Synapse. *Journal of Neuroscience* **18,** 6147–6162.

Doussau F, Humeau Y, Benfenati F & Poulain B (2010). A Novel Form of Presynaptic Plasticity Based on the Fast Reactivation of Release Sites Switched Off during Low-Frequency Depression. *Journal of Neuroscience* **30,** 16679–16691.

Doussau F, Schmidt H, Dorgans K, Valera AM, Poulain B & Isope P (2017). Frequency-dependent mobilization of heterogeneous pools of synaptic vesicles shapes presynaptic plasticity. *eLife* **6,** e28935

Dulubova I, Lou X, Lu J, Huryeva I, Alam A, Schneggenburger R, Südhof TC & Rizo J (2005). A Munc13/RIM/Rab3 tripartite complex: from priming to plasticity? *The EMBO Journal* **24,** 2839–2850.

Evans GJO, Wilkinson MC, Graham ME, Turner KM, Chamberlain LH, Burgoyne RD & Morgan A (2001). Phosphorylation of Cysteine String Protein by Protein Kinase A: IMPLICATIONS FOR THE MODULATION OF EXOCYTOSIS. *Journal of Biological Chemistry* **276,** 47877–47885.

Evstratova A & Tóth K (2014). Information processing and synaptic plasticity at hippocampal mossy fiber terminals. *Frontiers in Cellular Neuroscience* **8,** Article 28.

Ferraguti F & Shigemoto R (2006). Metabotropic glutamate receptors. *Cell and Tissue Research* **326,** 483–504.

Fisher SA, Fischer TM & Carew TJ (1997). Multiple overlapping processes underlying short-term synaptic enhancement. *Trends in Neurosciences* **20,** 170–177.

Forsythe ID, Tsujimoto T, Barnes-Davies M, Cuttle MF & Takahashi T (1998). Inactivation of Presynaptic Calcium Current Contributes to Synaptic Depression at a Fast Central Synapse. *Neuron* **20,** 797–807.

Foster KA & Regehr WG (2004). Variance-Mean Analysis in the Presence of a Rapid Antagonist Indicates Vesicle Depletion Underlies Depression at the Climbing Fiber Synapse. *Neuron* **43,** 119–131.

Geiger JRP & Jonas P (2000). Dynamic Control of Presynaptic Ca^{2+} Inflow by Fast-Inactivating K^{+} Channels in Hippocampal Mossy Fiber Boutons. *Neuron* **28,** 927–939.

González-Forero D, Montero F, García-Morales V, Domínguez G, Gómez-Pérez L, García-Verdugo JM & Moreno-López B (2012). Endogenous Rho-Kinase Signaling Maintains Synaptic Strength by

Stabilizing the Size of the Readily Releasable Pool of Synaptic Vesicles. *Journal of Neuroscience* **32,** 68–84.

Greengard P, Valtorta F, Czernik AJ & Benfenati F (1993). Synaptic Vesicle Phosphoproteins and Regulation of Synaptic Function. *Science* **259,** 780–785.

Greger IH, Ziff EB & Penn AC (2007). Molecular determinants of AMPA receptor subunit assembly. *Trends in Neurosciences* **30,** 407–416.

Hainmueller T & Bartos M (2020). Dentate gyrus circuits for encoding, retrieval and discrimination of episodic memories. *Nature Reviews Neuroscience* **21,** 153–168.

Hallermann S, Pawlu C, Jonas P & Heckmann M (2003). A large pool of releasable vesicles in a cortical glutamatergic synapse. *Proceedings of the National Academy of Sciences of the United States of America* **100,** 8975–8980.

Harris EW & Cotman CW (1986). Long-term potentiation of guinea pig mossy fiber responses is not blocked by N-methyl $_{D}$-aspartate antagonists. *Neuroscience Letters* **70,** 132–137.

Henze DA, Urban NN & Barrionuevo G (2000). The multifarious hippocampal mossy fiber pathway: a review. *Neuroscience* **98,** 407–427.

Hua Y, Woehler A, Kahms M, Haucke V, Neher E & Klingauf J (2013). Blocking Endocytosis Enhances Short-Term Synaptic Depression under Conditions of Normal Availability of Vesicles. *Neuron* **80,** 343–349.

Ishikawa T, Sahara Y & Takahashi T (2002). A Single Packet of Transmitter Does Not Saturate Postsynaptic Glutamate Receptors. *Neuron* **34,** 613–621.

Jackman SL, Turecek J, Belinsky JE & Regehr WG (2016). The calcium sensor synaptotagmin 7 is required for synaptic facilitation. *Nature* **529,** 88-91.

Jonas P, Major G & Sakmann B (1993). Quantal components of unitary EPSCs at the mossy fibre synapse on CA3 pyramidal cells of rat hippocampus. *The Journal of Physiology* **472,** 615–663.

Jones MV & Westbrook GL (1996). The impact of receptor desensitization on fast synaptic transmission. *Trends in Neurosciences* **19,** 96–101.

Junge HJ, Rhee JS, Jahn O, Varoqueaux F, Spiess J, Waxham MN, Rosenmund C & Brose N (2004). Calmodulin and Munc13 Form a Ca^{2+} Sensor/Effector Complex that Controls Short-Term Synaptic Plasticity. *Cell* **118,** 389–401.

Kamiya H & Ozawa S (1999). Dual mechanism for presynaptic modulation by axonal metabotropic glutamate receptor at the mouse mossy fibre-CA3 synapse. *The Journal of physiology* **518,** 497–506.

Kamiya H, Shinozaki H & Yamamoto C (1996). Activation of metabotropic glutamate receptor type 2/3 suppresses transmission at rat hippocampal mossy fibre synapses. *The Journal of Physiology* **493,** 447–455.

Kandel ER, Mack S, Jessell TM, Schwartz JH, Siegelbaum SA & Hudspeth AJ (2013). *Principles of Neural Science (5th Ed.),* McGraw-Hill Professional.

Katz B (1969). The release of neural transmitter substances (Sherrington Lecture). *Liverpool University Press,* Liverpool.

Kawaguchi S & Sakaba T (2017). Fast Ca^{2+} Buffer-Dependent Reliable but Plastic Transmission at Small CNS Synapses Revealed by Direct Bouton Recording. *Cell Reports* **21,** 3338−3345.

Kobayashi K, Manabe T & Takahashi T (1996). Presynaptic Long-Term Depression at the Hippocampal Mossy Fiber-CA3 Synapse. *Science* **273,** 648–650.

Koike M, Tsukada S, Tsuzuki K, Kijima H & Ozawa S (2000). Regulation of Kinetic Properties of GluR2 AMPA Receptor Channels by Alternative Splicing. *Journal of Neuroscience* **20,** 2166–2174.

Korn H, Triller A, Mallet A & Faber DS (1981). Fluctuating Responses at a Central Synapse: n of Binomial Fit Predicts Number of Stained Presynaptic Boutons. *Science* **213,** 898–901.

Kushmerick C, Renden R & von Gersdorff H (2006). Physiological Temperatures Reduce the Rate of Vesicle Pool Depletion and Short-Term Depression via an Acceleration of Vesicle Recruitment. *Journal of Neuroscience* **26,** 1366–1377.

Kusick GF, Chin M, Raychaudhuri S, Lippmann K, Adula KP, Hujber EJ, Vu T, Davis MW, Jorgensen EM & Watanabe S (2020). Synaptic vesicles transiently dock to refill release sites. *Nature Neuroscience* **23,** 1329–1338.

Kwon HB & Castillo PE (2008). Long-Term Potentiation Selectively Expressed by NMDA Receptors at Hippocampal Mossy Fiber Synapses. *Neuron* **57,** 108–120.

Lang U & Frotscher M (1990). Postnatal development of nonpyramidal neurons in the rat hippocampus (areas CA1 and CA3): a combined Golgi/electron microscope study. *Anatomy and Embryology* **181,** 533–545.

Lanthorn TH, Ganong AH & Cotman CW (1984). 2-Amino-4-phosphonobutyrate selectively blocks mossy fiber-CA3 responses in guinea pig but not rat hippocampus. *Brain Research* **290,** 174–178.

Lawrence JJ, Grinspan ZM & McBain CJ (2004). Quantal transmission at mossy fibre targets in the CA3 region of the rat hippocampus. *The Journal of Physiology* **554,** 175–193.

Leenders AGM & Sheng ZH (2005). Modulation of neurotransmitter release by the second messenger-activated protein kinases: Implications for presynaptic plasticity. *Pharmacology and Therapeutics* **105,** 69–84.

Lei S & McBain CJ (2002). Distinct NMDA Receptors Provide Differential Modes of Transmission at Mossy Fiber-Interneuron Synapses. *Neuron* **33,** 921–933.

Li GL, Cho S & von Gersdorff H (2014). Phase-Locking Precision Is Enhanced by Multiquantal Release at an Auditory Hair Cell Ribbon Synapse. *Neuron* **83,** 1404–1417.

Lindau M & Neher E (1988). Patch-clamp techniques for time-resolved capacitance measurements in single cells. *Pflügers Archiv* **411,** 137–146.

Liu H, Bai H, Hui E, Yang L, Evans CS, Wang Z, Kwon SE & Chapman ER (2014). Synaptotagmin 7 functions as a Ca^{2+}-sensor for synaptic vesicle replenishment. *eLife* **3,** e01524.

Lonart G, Schoch S, Kaeser PS, Larkin CJ, Südhof TC & Linden DJ (2003). Phosphorylation of RIM1α by PKA Triggers Presynaptic Long-Term Potentiation at Cerebellar Parallel Fiber Synapses. *Cell* **115,** 49–60.

Lou X, Scheuss V & Schneggenburger R (2005). Allosteric modulation of the presynaptic Ca^{2+} sensor for vesicle fusion. *Nature* **435,** 497–501.

Maccaferri G, Tóth K & McBain CJ (1998). Target-Specific Expression of Presynaptic Mossy Fiber Plasticity. *Science* **279,** 1368–1371.

Malagon G, Miki T, Llano I, Neher E & Marty A (2016). Counting Vesicular Release Events Reveals Binomial Release Statistics at Single Glutamatergic Synapses. *Journal of Neuroscience* **36,** 4010–4025.

Malagon G, Miki T, Tran V, Gomez LC & Marty A (2020). Incomplete vesicular docking limits synaptic strength under high release probability conditions. *eLife* **9,** e52137

Maschi D & Klyachko VA (2017). Spatiotemporal Regulation of Synaptic Vesicle Fusion Sites in Central Synapses. *Neuron* **94,** 65-73.e3.

Midorikawa M & Sakaba T (2015). Imaging Exocytosis of Single Synaptic Vesicles at a Fast CNS Presynaptic Terminal. *Neuron* **88,** 492–498.

Midorikawa M & Sakaba T (2017). Kinetics of Releasable Synaptic Vesicles and Their Plastic Changes at Hippocampal Mossy Fiber Synapses. *Neuron* **96,** 1033-1040.e3.

Miki T (2019). What We Can Learn From Cumulative Numbers of Vesicular Release Events. *Frontiers in Cellular Neuroscience* **13,** Article 257.

Miki T, Kaufmann WA, Malagon G, Gomez L, Tabuchi K, Watanabe M, Shigemoto R & Marty A (2017). Numbers of presynaptic Ca^{2+} channel clusters match those of functionally defined vesicular docking

sites in single central synapses. *Proceedings of the National Academy of Sciences of the United States of America* **114,** E5246-E5255; DOI: 10.1073/pnas.1704470114.

Miki T, Malagon G, Pulido C, Llano I, Neher E & Marty A (2016). Actin- and Myosin-Dependent Vesicle Loading of Presynaptic Docking Sites Prior to Exocytosis. *Neuron* **91,** 808–823.

Miki T, Midorikawa M & Sakaba T (2020). Direct imaging of rapid tethering of synaptic vesicles accompanying exocytosis at a fast central synapse. *Proceedings of the National Academy of Sciences of the United States of America* **117,** 14493–14502.

Miki T, Nakamura Y, Malagon G, Neher E & Marty A (2018). Two-component latency distributions indicate two-step vesicular release at simple glutamatergic synapses. *Nature Communications* **9,** 3943.

Miyano R, Miki T & Sakaba T (2019). Ca-dependence of synaptic vesicle exocytosis and endocytosis at the hippocampal mossy fibre terminal. *The Journal of Physiology* **597,** 4373–4386.

Mori M, Abegg MH, Gähwiler BH & Gerber U (2004). A frequency-dependent switch from inhibition to excitation in a hippocampal unitary circuit. *Nature* **431,** 453–456.

Nakanishi S (1994). Metabotropic glutamate receptors: Synaptic transmission, modulation, and plasticity. *Neuron* **13,** 1031–1037.

Neher E (2015). Merits and Limitations of Vesicle Pool Models in View of Heterogeneous Populations of Synaptic Vesicles. *Neuron* **87,** 1131–1142.

Neher E & Sakaba T (2008). Multiple Roles of Calcium Ions in the Regulation of Neurotransmitter Release. *Neuron* **59,** 861–872.

Nicoll RA & Schmitz D (2005). Synaptic plasticity at hippocampal mossy fibre synapses. *Nature Reviews Neuroscience* **6,** 863–876.

Otis T, Zhang S & Trussell LO (1996). Direct Measurement of AMPA Receptor Desensitization Induced by Glutamatergic Synaptic Transmission. *Journal of Neuroscience* **16,** 7496–7504.

Pan B & Zucker RS (2009). A General Model of Synaptic Transmission and Short-Term Plasticity. *Neuron* **62,** 539–554.

Pelkey KA, Lavezzari G, Racca C, Roche KW & McBain CJ (2005). mGluR7 is a Metaplastic Switch Controlling Bidirectional Plasticity of Feedforward Inhibition. *Neuron* **46,** 89–102.

Pelkey KA, Topolnik L, Lacaille JC & McBain CJ (2006). Compartmentalized Ca^{2+} Channel Regulation at Divergent Mossy-Fiber Release Sites Underlies Target Cell-Dependent Plasticity. *Neuron* **52,** 497–510.

Pelkey KA, Topolnik L, Yuan XQ, Lacaille JC & McBain CJ (2008). State-Dependent cAMP Sensitivity of Presynaptic Function Underlies Metaplasticity in a Hippocampal Feedforward Inhibitory Circuit. *Neuron* **60,** 980–987.

Pulido C & Marty A (2017). Quantal Fluctuations in Central Mammalian Synapses: Functional Role of Vesicular Docking Sites. *Physiological Reviews* **97,** 1403–1430.

Pulido C & Marty A (2018). A two-step docking site model predicting different short-term synaptic plasticity patterns. *Journal of General Physiology* **150,** 1107–1124.

Pulido C, Trigo FF, Llano I & Marty A (2015). Vesicular Release Statistics and Unitary Postsynaptic Current at Single GABAergic Synapses. *Neuron* **85,** 159–172.

Quastel DMJ (1997). The Binomial Model in Fluctuation Analysis of Quantal Neurotransmitter Release. *Biophysical Journal* **72,** 728–753.

Ramon y Cajal S (1894). The Croonian lecture.—La fine structure des centres nerveux. *Proceedings of the Royal Society of London* **55,** 444–468.

Redman S (1990). Quantal analysis of synaptic potentials in neurons of the central nervous system. *Physiological Reviews* **70,** 165–198.

Regehr WG, Delaney KR & Tank DW (1994). The role of presynaptic calcium in short-term enhancement at the hippocampal mossy fiber synapse. *Journal of Neuroscience* **14,** 523–537.

Ritzau-Jost A, Tsintsadze T, Krueger M, Ader J, Bechmann I, Eilers J, Barbour B, Smith SM & Hallermann S (2021). Large, Stable Spikes Exhibit Differential Broadening in Excitatory and Inhibitory Neocortical Boutons. *Cell Reports* **34,** 108612.

Robert A & Howe JR (2003). How AMPA Receptor Desensitization Depends on Receptor Occupancy. *Journal of Neuroscience* **23,** 847–858.

Rollenhagen A, Sätzler K, Rodríguez EP, Jonas P, Frotscher M & Lübke JHR (2007). Structural Determinants of Transmission at Large Hippocampal Mossy Hiber Synapses. *Journal of Neuroscience* **27,** 10434–10444.

Rozov A, Jerecic J, Sakmann B & Burnashev N (2001). AMPA Receptor Channels with Long-Lasting Desensitization in Bipolar Interneurons Contribute to Synaptic Depression in a Novel Feedback Circuit in Layer 2/3 of Rat Neocortex. *Journal of Neuroscience* **21,** 8062–8071.

Sakamoto H, Ariyoshi T, Kimpara N, Sugao K, Taiko I, Takikawa K, Asanuma D, Namiki S & Hirose K (2018). Synaptic weight set by Munc13-1 supramolecular assemblies. *Nature Neuroscience* **21,** 41–49.

Saviane C & Silver RA (2006). Fast vesicle reloading and a large pool sustain high bandwidth transmission at a central synapse. *Nature 2006 439:7079* **439,** 983–987.

Scheuss V & Neher E (2001). Estimating Synaptic Parameters from Mean, Variance, and Covariance in Trains of Synaptic Responses. *Biophysical Journal* **81,** 1970–1989.

Schneggenburger R, Meyer AC & Neher E (1999). Released Fraction and Total Size of a Pool of Immediately Available Transmitter Quanta at a Calyx Synapse. *Neuron* **23,** 399–409.

Schneggenburger R, Sakaba T & Neher E (2002). Vesicle pools and short-term synaptic depression: lessons from a large synapse. *Trends in Neurosciences* **25,** 206–212.

Schoepp DD (2001). Unveiling the Functions of Presynaptic Metabotropic Glutamate Receptors in the Central Nervous System. *The Journal of Pharmacology and Experimental Therapeutics* **299,** 12–20.

Schoepp DD & Conn PJ (1993). Metabotropic glutamate receptors in brain function and pathology. *Trends in Pharmacological Sciences* **14,** 13–20.

Scott R, Lalic T, Kullmann DM, Capogna M & Rusakov DA (2008). Target-Cell Specificity of Kainate Autoreceptor and Ca^{2+}-Store-Dependent Short-Term Plasticity at Hippocampal Mossy Fiber Synapses. *Journal of Neuroscience* **28,** 13139–13149.

Shigemoto R, Kinoshita A, Wada E, Nomura S, Ohishi H, Takada M, Flor PJ, Neki A, Abe T, Nakanishi S & Mizuno N (1997). Differential Presynaptic Localization of Metabotropic Glutamate Receptor Subtypes in the Rat Hippocampus. *Journal of Neuroscience* 17**,** 7503–7522.

Shin O-H, Lu J, Rhee J-S, Tomchick DR, Pang ZP, Wojcik SM, Camacho-Perez M, Brose N, Machius M, Rizo J, Rosenmund C & Südhof TC (2010). Munc13 C_2B domain is an activity-dependent Ca^{2+} regulator of synaptic exocytosis. *Nature Structural & Molecular Biology* **17,** 280–288.

Silver RA, Momiyama A & Cull-Candy SG (1998). Locus of frequency-dependent depression identified with multiple-probability fluctuation analysis at rat climbing fibre-Purkinje cell synapses. *The Journal of Physiology* **510,** 881–902.

Sivaramakrishnan S & Laurent G (1995). Pharmacological characterization of presynaptic calcium currents underlying glutamatergic transmission in the avian auditory brainstem. *Journal of Neuroscience* **15,** 6576–6585.

Spiess AN & Neumeyer N (2010). An evaluation of R^2 as an inadequate measure for nonlinear models in pharmacological and biochemical research: A Monte Carlo approach. *BMC Pharmacology* **10,** Article number: 6.

Srinivasan G, Kim JH & von Gersdorff H (2008). The Pool of Fast Releasing Vesicles Is Augmented by Myosin Light Chain Kinase Inhibition at the Calyx of Held Synapse. *Journal of Neurophysiology* **99,** 1810–1824.

Südhof TC (2004). The synaptic vesicle cycle. *Annual Review of Neuroscience* **27,** 509–547.

Takahashi T, Forsythe ID, Tsujimoto T, Barnes-Davies M & Onodera K (1996). Presynaptic Calcium Current Modulation by a Metabotropic Glutamate Receptor. *Science* **274,** 594–597.

Takahashi T, Kajikawa Y & Tsujimoto T (1998). G-Protein-Coupled Modulation of Presynaptic Calcium Currents and Transmitter Release by a $GABA_B$ Receptor. *Journal of Neuroscience* **18,** 3138–3146.

Takahashi T & Momiyama A (1993). Different types of calcium channels mediate central synaptic transmission. *Nature* **366,** 156–158.

Tang AH, Chen H, Li TP, Metzbower SR, MacGillavry HD & Blanpied TA (2016). A trans-synaptic nanocolumn aligns neurotransmitter release to receptors. *Nature* **536,** 210–214.

Tang F (2005). Agonists and Antagonists of Metabotropic Glutamate Receptors: Anticonvulsants and Antiepileptogenic Agents? *Current Neuropharmacology* **3,** 299–307.

Taschenberger H & von Gersdorff H (2000). Fine-Tuning an Auditory Synapse for Speed and Fidelity: Developmental Changes in Presynaptic Waveform, EPSC Kinetics, and Synaptic Plasticity. *Journal of Neuroscience* **20,** 9162–9173.

Taschenberger H, Leão RM, Rowland KC, Spirou GA & von Gersdorff H (2002). Optimizing Synaptic Architecture and Efficiency for High-Frequency Transmission. *Neuron* **36,** 1127–1143.

Taschenberger H, Scheuss V & Neher E (2005). Release kinetics, quantal parameters and their modulation during short-term depression at a developing synapse in the rat CNS. *The Journal of Physiology* **568,** 513–537.

Tong G & Jahr CE (1994). Multivesicular release from excitatory synapses of cultured hippocampal neurons. *Neuron* **12,** 51–59.

Tóth K & McBain CJ (1998). Afferent-specific innervation of two distinct AMPA receptor subtypes on single hippocampal interneurons. *Nature Neuroscience* **1,** 572–578.

Tóth K, Suares G, Lawrence JJ, Philips-Tansey E & McBain CJ (2000). Differential mechanisms of transmission at three types of mossy fiber synapse. *Journal of Neuroscience* **20,** 8279–8289.

Trigo FF, Sakaba T, Ogden D & Marty A (2012). Readily releasable pool of synaptic vesicles measured at single synaptic contacts. *Proceedings of the National Academy of Sciences of the United States of America* **109,** 18138–18143.

Trussell LO, Zhang S & Ramant IM (1993). Desensitization of AMPA receptors upon multiquantal neurotransmitter release. *Neuron* **10,** 1185–1196.

Tzounopoulos T, Janz R, Südhof TC, Nicoll RA & Malenka RC (1998). A Role for cAMP in Long-Term Depression at Hippocampal Mossy Fiber Synapses. *Neuron* **21,** 837–845.

Vaden JH, Banumurthy G, Gusarevich ES, Overstreet-Wadiche L & Wadiche JI (2019). The readily-releasable pool dynamically regulates multivesicular release. *eLife* **8,** e47434.

Vandael D, Borges-Merjane C, Zhang X & Jonas P (2020). Short-Term Plasticity at Hippocampal Mossy Fiber Synapses Is Induced by Natural Activity Patterns and Associated with Vesicle Pool Engram Formation. *Neuron* **107,** 509-521.e7.

Vere-Jones D (1966). SIMPLE STOCHASTIC MODELS FOR THE RELEASE OF QUANTA OF TRANSMITTER FROM A NERVE TERMINAL. *Australian Journal of Statistics* **8,** 53–63.

Vida I & Frotscher M (2000). A hippocampal interneuron associated with the mossy fiber system. *Proceedings of the National Academy of Sciences of the United States of America* **97,** 1275–1280.

von Gersdorff H & Borst JGG (2002). Short-term plasticity at the calyx of held. *Nature Reviews Neuroscience* **3,** 53–64.

Vyleta NP & Jonas P (2014). Loose Coupling Between Ca^{2+} Channels and Release Sensors at a Plastic Hippocampal Synapse. *Science* **343,** 665−670.

Wang LY & Kaczmarek LK (1998). High-frequency firing helps replenish the readily releasable pool of synaptic vesicles. *Nature* **394,** 384–388.

Wheeler DB, Randall A & Tsien RW (1994). Roles of N-Type and Q-Type Ca^{2+} Channels in Supporting Hippocampal Synaptic Transmission. *Science* **264,** 107–111.

Wilke SA, Antonios JK, Bushong EA, Badkoobehi A, Malek E, Hwang M, Terada M, Ellisman MH & Ghosh A (2013). Deconstructing Complexity: Serial Block-Face Electron Microscopic Analysis of the Hippocampal Mossy Fiber Synapse. *Journal of Neuroscience* **33,** 507–522.

Wu LG & Borst JGG (1999). The Reduced Release Probability of Releasable Vesicles during Recovery from Short-Term Synaptic Depression. *Neuron* **23,** 821–832.

Xu J & Wu LG (2005). The Decrease in the Presynaptic Calcium Current Is a Major Cause of Short-Term Depression at a Calyx-Type Synapse. *Neuron* **46,** 633–645.

Zucker RS (1973). Changes in the statistics of transmitter release during facilitation. *The journal of physiology* **229,** 787–810.

Zucker RS & Regehr WG (2002). Short-Term Synaptic Plasticity. *Annual Review of Physiology* **64,** 355–405.